Journal of Polymer Science

Part A-2: Polymer Physics

Contents

Electron Spin Resonance of γ-Irradiated Poly(ethylene 2,6-naphthalene Dicarboxylate)

R. S. ROGOWSKI and G. F. PEZDIRTZ, *Chemistry and Physics Branch; NASA Langley Research Center, Hampton, Virginia 23365*

Synopsis

The two types of radicals trapped in γ-irradiated poly(ethylene 2,6-naphthalene dicarboxylate) (PEN 2,6) have been identified by ESR as —O—ĊH—CH$_2$—O— (radical I) and a radical located on the naphthalene ring (radical II). The relative concentrations of radicals in the gross polymer are 10–20% radical I and 80–90% radical II. Similar trapped radicals have been identified in γ-irradiated poly(ethylene terephthalate) (PET), a structurally related polymer which differs only in the aromatic moiety, but the relative radical concentrations are quite different. These results are discussed in relation to the radiation resistance of the two polymers.

Introduction

Poly(ethylene 2,6-naphthalene dicarboxylate) (PEN-2,6)
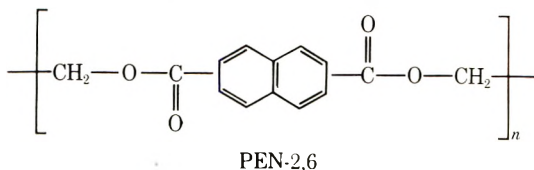
PEN-2,6

has been the subject of several studies at this laboratory.[1–3] Specifically it has been shown that PEN-2.6 has greater resistance to ionizing radiation than poly(ethylene terephthalate) (PET)

PET
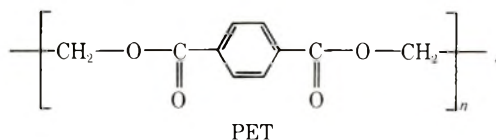
Radiation effects in PEN-2,6 are characterized by a high ratio of chain crosslinks to chain scissions, in contrast to the behavior of PET which degrades mostly by chain rupture with negligible chain crosslinking.[4] The ESR spectra of γ-irradiated PET have been published,[5–13] and at least two radical species identified.[5,6,10]

The ESR spectra of γ-irradiated PEN-2,6 have now been studied to elucidate the effect of replacing the phenylene ring with the naphthalene
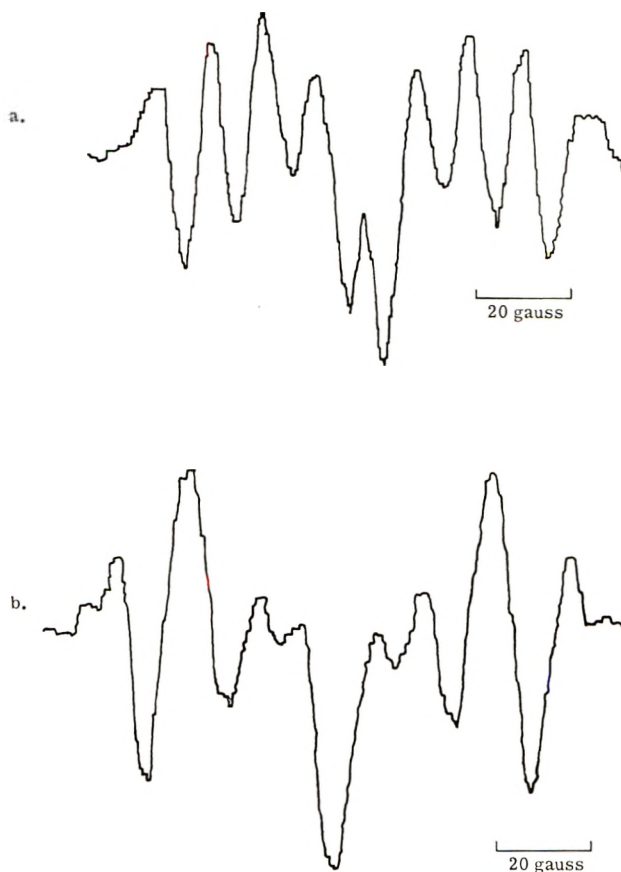
Fig. 1. Second derivative ESR spectra of PEN film with face of film (a) perpendicular to and (b) parallel to H_0 ($T = 298°K$).

rings in the polymer on the formation of radicals and to identify the radical species. The results are compared with those of PET.

Experimental

ESR spectra were measured on γ-irradiated PEN-2,6 powder and uniaxially and biaxially oriented films. The PEN-2,6 powder was synthesized in this laboratory and was melt-pressed to produce film samples. The film was then uniaxially oriented by stretching at temperatures between 50 and 80°C. The uniaxially oriented films were cut into rectangular strips which were stacked with the orientation in the same direction and placed in quartz tubes. The biaxially oriented film was obtained from the Minnesota Mining and Manufacturing Company and was treated like the uniaxially oriented film.

The samples of powder and film were sealed in quartz tubes after evacuation for over 4 hr at 10^{-6} torr and were exposed to γ-rays from a ^{60}Co source at 308°K. The total dose was 5–50 Mrad at a dose rate of 2 Mrad/hr.
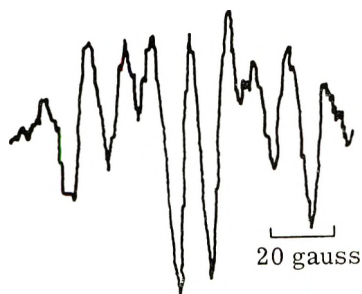
Fig. 2.   Second derivative ESR spectrum of PEN powder (T = 298°K).
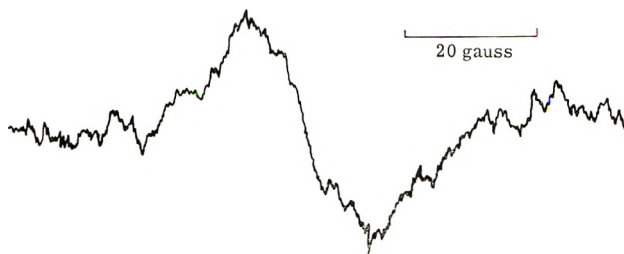
Fig. 3. ESR spectrum of PEN film showing signal from radical species stable at 423°K.

The ESR spectra of the samples sealed in quartz tubes were obtained with a Varian V-4502 ESR spectrometer.   Magnetic field calibration was accomplished with a proton resonance signal from a Varian F-8 fluxmeter. DPPH was used as a standard for measuring g values (spectroscopic splitting factor) and spin concentrations.

Results

The ESR spectra of uniaxially oriented film (Fig. 1) illustrate the dependence of the spectra on the orientation of film in the magnetic field. The eight-line spectrum (Fig. 1a) in the orientation with the magnetic field perpendicular to the film surface changes to a five-line spectrum in the orientation with the field parallel to the film surface.   Both spectra contain a broad overlapping signal which is shown below to be due to another radical.   The extreme splitting changes from 75 gauss for the perpendicular orientation to 82 gauss for the parallel orientation of the film in the magnetic field.   The g value for the radical producing the eight hyperfine lines is 2.0025 ± 0.0002, which is very close to the free-electron value.

For comparison, the spectrum of PEN-2,6 powder which was used to make the film is shown in Figure 2.   The spectrum from this randomly oriented sample is not significantly different from the eight line spectrum of the film.   The hyperfine pattern is present in the powder, and therefore the anisotropic part of the coupling value is not large enough to broaden the lines beyond resolution.
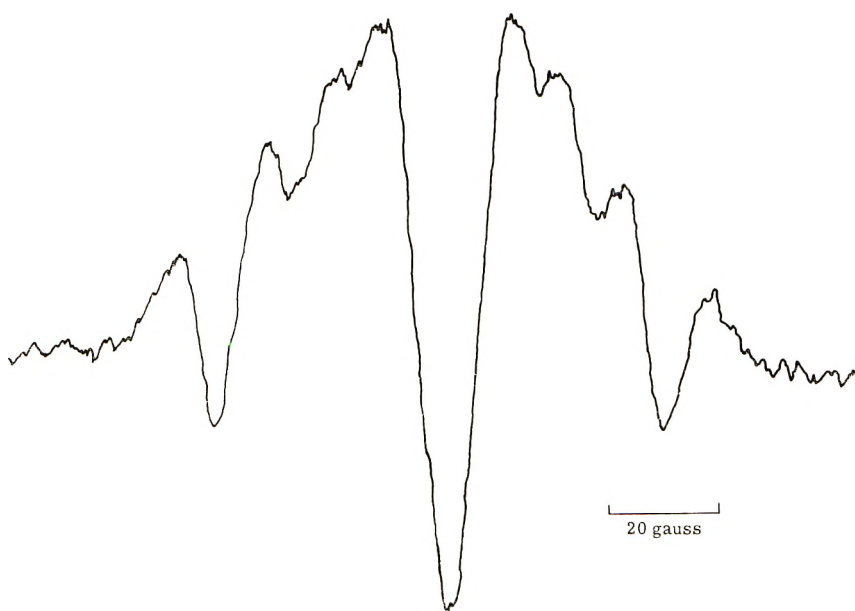
Fig. 4. ESR spectrum of biaxially oriented PEN film with surface of film parallel to H_0 ($T = 298°K$).
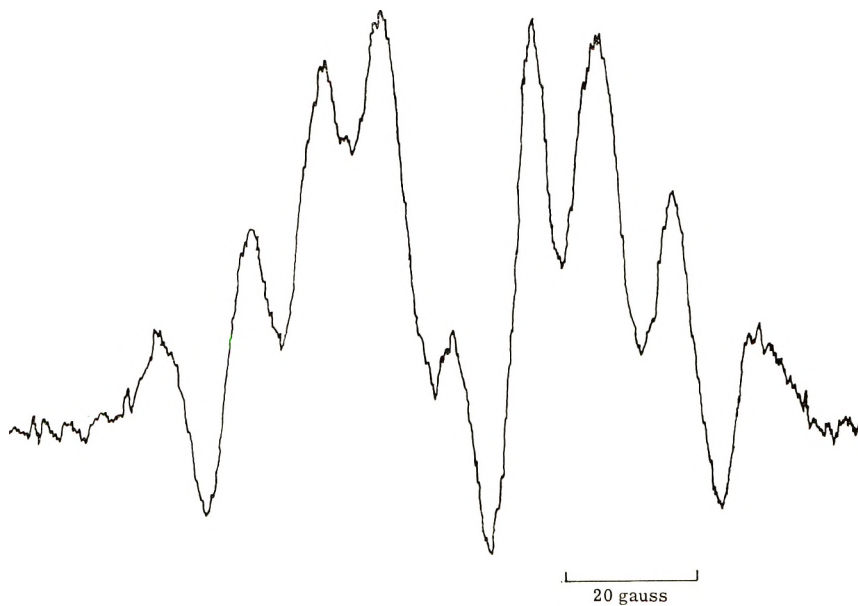
Fig. 5. EST spectrum of biaxially oriented film with face of film perpendicular to H_0 ($T = 298°K$).

Upon heating the irradiated film at 423°K for one hour the eight-line spectrum was observed to decay and a broad, poorly resolved spectrum shown in Figure 3 was observed. Only a broad line with a halfwidth of 18 gauss remains when the spectrum is measured at room temperature.

The spectra of biaxially oriented film (Figs. 4 and 5) observed at room temperature consisted of the characteristic eight line pattern with the film perpendicular to the magnetic field. The spectra changed only slightly with changes in orientation indicating that there is a lower degree of ordering in the biaxial film than in the uniaxial film.

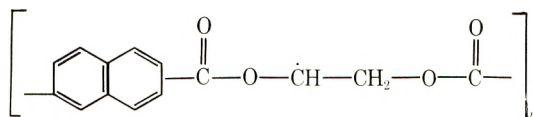By comparison with DPPH the G value (spins/100 eV of absorbed dose) was found to be 0.02 ± 0.003 for powder and film samples. This approximates the G value for the total radicals in PET.

Discussion

The spectrum of Figure 1 is assigned to radical I

Radical I

which is produced by abstraction of a hydrogen atom from a methylene group along the polymer chain. This radical would account for the eight-line spectrum with three different coupling constants resulting from coupling of the unpaired electron with the three adjacent protons. In the perpendicular orientation the coupling values are 10, 22, 43 gauss with the value of 10 gauss assigned to the interaction with the α proton, which is expected to have the largest anisotropic coupling. The α coupling value increases to 17 gauss in the parallel orientation and produces the five-line spectrum of Figure 1 with an extreme splitting of 82 gauss.

Ideally, the eight-line spectrum produced by the hyperfine interaction with three protons would have lines of equal intensity. The unequal intensities observed may be explained in terms of a broad component overlapping with this signal. The spectrum of Figure 1 was synthesized with a computer program by superimposing the broad line signal of Figure 3 on an ideal eight-line spectrum. The result is shown in Figure 6, where the computed spectrum is compared with the experimental spectrum. The computer program was obtained from the Quantum Chemistry Program Exchange[13] and was revised to superimpose spectra of different intensities and g values.

Considering the high temperature stability and the linewidth of the radical producing the spectrum of Figure 4 (radical II) it is probably due to an aromatic radical located on the naphthalene ring. By double integration of the signals from radical I and radical II, the relative concentration of the two species was found to be 10–20% radical I and 80–90% radical II trapped in PEN-2,6 at room temperature.
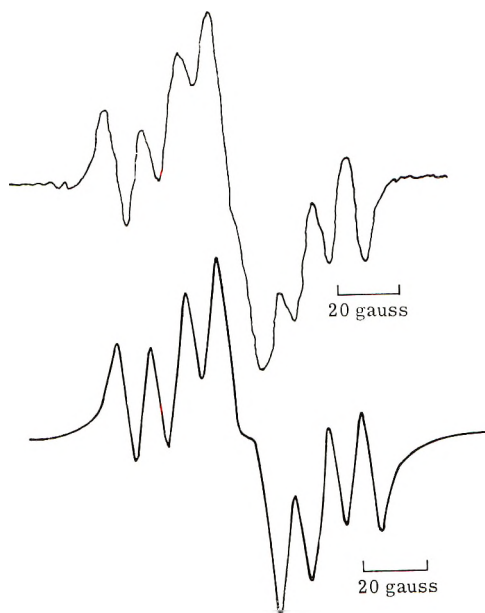
Fig. 6. Comparison of observed and calculated spectra for PEN (first derivative).

Results for PET indicate that the radical III, which is similar to radical
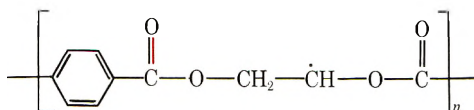
Radical III

I, accounts for only about 1–2% of the radical concentration trapped in PET,[14] with an aromatic radical on the benzene ring making up the remainder of the signal from the unpaired electrons.   The G value for all radicals trapped in PET is also about 0.02.

The higher concentration of the aliphatic radical I in PEN-2,6 compared to the concentration of a similar aliphatic radical in PET indicates that the naphthalene ring may be stabilizing this radical and preventing chain rupture.   If PEN-2,6 crosslinks through the aromatic part of the polymer chain, the concentration of the aromatic radical II would be further decreased relative to radical I and would also account for the lower concentration of aromatic radical in PEN-2,6.

The α-coupling constant for radical I in PEN-2,6 has an isotropic value of approximately 13 gauss and is anomalously low for a typical aliphatic radical, but this may be due in part to an electron withdrawal effect of the fused rings in naphthalene.   The isotropic value for coupling to the α proton of the analogous radical in PET is close to the 23 gauss value normally observed for aliphatic types of radicals.   The extreme splittings for the aliphatic radical in PET are 81 and 92 gauss, determined for the per-

pendicular and parallel orientations respectively,[14,15] whereas for PEN-2,6 the comparable splittings were observed to be 75 and 82 gauss. The differences in the splittings might be accounted for by the difference in the α coupling constant for the two polymers.

Fessenden and Schuler have observed low values of α-coupling constants and have attributed the effect to a departure from the normal π radical structure.[16] The structure that is assumed to give a coupling of 23 gauss, is one in which the unpaired electron is located in a p-orbital perpendicular to the plane containing the three sp^2 carbon bonds. If the unpaired electron is not in a pure p-orbital but possesses some s character then the coupling value for the α proton will change.

On the other hand Fischer, in a study of proton coupling in a series of substituted alkyl radicals,[17] concluded that the coupling values depended on the electron withdrawing characteristic of the substituents. Molecular orbital calculations are being carried out on this radical to determine if there is a significant difference in spin density on the α carbon to account for the difference in coupling constant for the radical in PEN-2,6 and further to determine if the greater electronegativity of the naphthalene ring makes a contribution to the spin density.

References

1. *Chem. Eng. News*, **43**, 38 (May 17, 1965).

2. D. H. Phillips and J. C. Schug, *J. Chem. Phys.*, **50**, 3297 (1969).

3. H. D. Hendricks, *J. Mol. Phys.*, **20**, 189 (1970).

4. D. T. Turner, G. F. Pezdirtz, and G. D. Sands, *J. Polym. Sci. A-1*, **4**, 252 (1966).

5. D. Campbell, K. Araki, and D. T. Turner, *J. Polym. Sci. A-1*, **4**, 2597 (1966).

6. K. Araki, D. Campbell, and D. T. Turner, *J. Polym. Sci. B*, **3**, 993 (1965).

7. S. Ohnishi, Y. Ikeda, M. Kashiwagi, and I. Natta, *Polymer*, **2**, 119 (1961).

8. Z. Kuri and H. Ueda, *J. Polym. Sci.*, **50**, 349 (1961).

9. Y. Hama, S. Okamoto and N. Tamura, *Repts. Progr. Polym. Phys. Japan*, **7**, 351 (1964).

10. D. Campbell and D. T. Turner, *J. Polym. Sci. A-1*, **5**, 2199 (1967).

11. J. Sobue, Y. Tabata, and M. Hiroaka, *Kogyo Kagaku Zasshi*, **64**, 372 (1961).

12. J. R. Chapman, Ph.D. Thesis, Vanderbilt Univ., 1967.

13. C. S. Johnson, Jr., and M. K. Ahn, Program 83, Quantum Chemistry Program Exchange, Indiana University, 1968.

14. R. S. Rogowski, to be published.

15. D. Campbell, *J. Polym. Sci. D*, **4**, 91 (1970).

16. R. W. Fessenden and R. H. Schuler, *J. Chem. Phys.*, **39**, 2147 (1963).

17. H. Fischer, *Z. Naturforsch.*, **20A**, 428 (1965).

Statistical Thermodynamics of Networks
at Large Deformations

K. J. SMITH, JR., *Polymer Research Center, State University College of Forestry at Syracuse University, Syracuse, New York 13210*

Synopsis

A general theory of non-Gaussian elasticity is presented for real polymeric chains having fixed bond angles and restricted internal rotations. The theory contains the displacement-vector distribution given by Nagai, and the Flory-Wall-Hermans procedure is used for the calculation of network properties. Whereas the treatment is valid for all types of polymer chains, it is not totally satisfactory from a practical standpoint because of a slow series convergence if the chains are stiff. It is best utilized for flexible polymers under conditions of light crosslinking. Detailed network behavior is investigated only for polyethylene type chains having uncorrelated internal rotations. In this instance the fractional contribution f_e/f of the internal energy to the total force f is found to be a function of elongation at high degrees of stretching. It may decrease, or increase, depending upon the sign of f_e/f at low elongations. Furthermore, the variation of f_e/f with elongation is independent of the fixed bond angle of the chain backbone. Stress–strain behavior and energy–strain behavior are in opposition, i.e., when the non-Gaussian contribution to the stress is greatest, it is the least for the ratio f_e/f, and vice versa. The presence of correlated internal rotations would not be expected to greatly alter these general conclusions.

Introduction

The network theory of elasticity[1-5] was originally developed for flexibly jointed polymer chains, i.e., chains for which the orientation of a chain link is completely independent of the positions of all others. In the Gaussian approximation such an idealization makes little difference for it may be argued that the same distribution must hold for real chains having fixed bond angles and restricted internal rotations. Deviations from Gaussian behavior as a consequence of finite chain extensibility, however, present certain difficulties which can not be overcome by the use of "equivalent" flexibly jointed chains.[6-8] The existing theories[9,10] of non-Gaussian chains are inadequate on this account. The basic difficulty stems from the fact that the moments of a flexibly jointed chain are functions of only two quantities; the number of links N in the chain and the length of each link b. The moments of real chains, however, cannot be reduced to only two parameters. The Gaussian distribution involves only a single moment, the second one $\langle r^2 \rangle_0$ (mean square end-to-end displacement of the chain vector $\mathbf{r}$), and can easily be described in terms of the two parameters. But the exact distribution for all degrees of stretch involves not only $\langle r^2 \rangle_0$

but $\langle r^4 \rangle_0$, $\langle r^6 \rangle_0$ and higher moments. Hence, an equivalent chain concept is unsatisfactory for non-Gaussian chains.

Volkenstein and Ptitsyn[11] calculated the conformational integral of a real chain under a constant load, but their solution is not satisfactory for a network treatment because it yields an average displacement for the load f. What is required is the function of average load for displacement $\mathbf{r}$. Nagai,[12] adopting a procedure given earlier by Chandrasekhar,[13] derived the desired function, but to date there has been no attempt to incorporate this result into a general network theory. It is the intent of this paper to do so and to discuss some of the pertinent features thereof.

Theory

The probability density for a polymer chain of N links having an end-to-end distance $\mathbf{r}$ is

$$W(\mathbf{r}) = \int \delta(\mathbf{r}' - \mathbf{r})W(\mathbf{r}')d\mathbf{r}'$$

where $\delta(\mathbf{r}' - \mathbf{r})$ is the Dirac delta function:

$$\delta(\mathbf{r}' - \mathbf{r}) = \frac{1}{8\pi^3} \int e^{i\mathbf{p}\cdot(\mathbf{r}'-\mathbf{r})}d\mathbf{p}$$

Integration over $\mathbf{r}'$ and the angular coordinates of $\mathbf{p}$ leads immediately to the equation of Nagai[12]

$$W(\mathbf{r}) = \frac{1}{2\pi^2} \int_0^\infty \frac{\sin (pr)}{r} \left\langle \frac{\sin (pr)}{r} \right\rangle_0 dp \tag{1}$$

where the term in angular brackets with subscript zero represents an unperturbed average. Equation (1) is the exact density function for any kind of polymer chain, but further integration cannot be performed in closed form. Nagai expands $\langle \sin (pr)/r \rangle_0$ in terms of its argument and integrates term by term. The result is

$$W(\mathbf{r}) = \left(\frac{3}{2\pi\langle r^2 \rangle_*}\right)^{3/2} e^{-3r^2/2\langle r^2 \rangle_*} \left\{ 1 - \delta_1 \left[1 - \frac{r^2}{\langle r^2 \rangle_*} \right] \right.$$

$$+ \delta_2 \left[5 - \frac{10r^2}{\langle r^2 \rangle_*} + \frac{3r^4}{\langle r^2 \rangle_*^2} \right] - \delta_3 \left[35 - \frac{105r^2}{\langle r^2 \rangle_*} + \frac{63r^4}{\langle r^2 \rangle_*^2} - \frac{9r^6}{\langle r^2 \rangle_*^3} \right] + \cdots \left. \right\}$$

$$\tag{2}$$

where

$$\delta_1 = 3[\langle r^2 \rangle_0 - \langle r^2 \rangle_*]/2\langle r^2 \rangle_*$$

$$\delta_2 = 9 \left[\langle r^4 \rangle_0 - \frac{10}{3} \langle r^2 \rangle_0 \langle r^2 \rangle_* + \frac{5}{3} \langle r^2 \rangle_*^2 \right] \Big/ 40\langle r^2 \rangle_*^2$$

$$\delta_3 = 9 \left[\langle r^6 \rangle_0 - 7\langle r^4 \rangle_0 \langle r^2 \rangle_* + \frac{35}{3} \langle r^2 \rangle_0 \langle r^2 \rangle_*^2 - \frac{35}{9} \langle r^2 \rangle_*^3 \right] \Big/ 560\langle r^2 \rangle_*^3$$

and $\langle r^2 \rangle_*$ is that portion of $\langle r^2 \rangle_0$ which is directly proportional to the number of links N. The point of expressing $W(\mathbf{r})$ in this manner is that

δ_1 and δ_2 are both proportional to N^{-1}, and $\delta_3 \propto N^{-2}$. Thus, the density is written as a series in powers of N^{-1}. When N is very large, only a few terms in the series need be retained, and in the limit $N \to \infty$ the familiar Gaussian result is obtained.

In order to incorporate this result into a network theory of elasticity, a method similar to that used by Smith, Ciferri, and Hermans[10] for flexibly jointed chains is adopted; however, we include herein the effect of different chain contour lengths.

Consider a network composed of G chains formed by the introduction of approximately $G/2$ crosslinks. As crosslinking can be presumed to be more or less random in nature, a distribution of chain contour lengths will be present. If we let j represent the number of links in a chain, the partition function for the network can be written as

$$Z \propto \prod_j \frac{G_j!}{\prod_i G_{ij}!} \prod_i W_{ij}{}^{G_{ij}}$$

where there are G_j chains of j links, G_{ij} chain of j links having an endpoint displacement $\mathbf{r}_i$, and W_{ij} is the probability density of a j chain having a displacement $\mathbf{r}_i$. The product over j arises because each j must be considered as a different molecular species. By using Sterling's approximation this can be written as

$$\ln Z = \sum_j [G_j \ln G_j - \sum_i G_{ij} \ln (G_{ij}/W_{ij})] + \text{constant} \tag{3}$$

The condition

$$\sum_i G_{ij} = G_j \tag{4}$$

must be met. In addition, a relation between the end-to-end vectors and the bulk deformation must be introduced. One can only make an assumption on this point, and we propose to follow Wall;[1] i.e.,

$$\sum_i x_{ij}{}^2 G_{ij} = G_j \langle x_j{}^2 \rangle_* \lambda_x{}^2 \tag{5}$$

where $\lambda_x{}^2$ is the deformation ratio $\langle x_j{}^2 \rangle / \langle x_j{}^2 \rangle_*$ and is the same for all j. Similar equations hold for y and z.

Using undetermined multipliers to introduce conditions (4 and 5) into eq. (3)

$$G_{ij} = W_{ij} e^{a_j} e^{\Sigma_x C_{xj} x_{ij2}}$$

where a_j and C_{xj} are the constants to be determined and the summation is over the coordinates x,y,z. Thus

$$\ln Z = \sum_j G_j \{ \ln G_j - [a_j + \sum_x \langle x_j{}^2 \rangle_* \lambda_x{}^2] \} + \text{constant}$$

which may be recast into the form

$$\Delta A = 2kT \sum_j G_j \sum_x \langle x_j{}^2 \rangle_* \int C_{xj} \lambda_x d\lambda_x \tag{6}$$

where $A = -kT \ln Z$ is the elastic free energy. The constant C_{zj} is found from the equation

$$\frac{\partial}{\partial C_{zj}} \ln \left\{ \sum_i W_{ij} e^{\Sigma_x C_{zj} x_{ij}^2} \right\} = \langle x_j^2 \rangle_* \lambda_z^2$$

Using eq. (2) for $W_{ij} = W_j(r_i)$, replacing the summation by an integration, we find

$$C_{zj} = \frac{1}{2 \langle x_j^2 \rangle_*} \left\{ 1 - \frac{1}{\lambda_z^2} \left[1 - \frac{20}{3} \delta_2 \lambda_z^2 \left(1 - \frac{1}{5} \sum_x \lambda_x^2 - \frac{2}{5} \lambda_z^2 \right) \right] \right\}$$

$$- \frac{1}{3 \langle x_j^2 \rangle_*} \delta_1 \quad (7)$$

Here the δ_3 term has been omitted. Then, from eqs. (6 and 7), we obtain

$$\Delta A = kT \sum_j G_j \left\{ - \ln \left(\Pi_x \lambda_x \right) + \frac{1}{2} \left[1 - \frac{2}{3} (\delta_1 - 10 \delta_2) \right] \left[\sum_x \lambda_x^2 - 3 \right] \right.$$

$$\left. - \delta_2 \left[\sum_x \lambda_x^4 - 3 \right] - \frac{2}{3} \delta_2 \left[\sum_{x<y} \lambda_x^2 \lambda_y^2 - 3 \right] \right\}$$

The Gaussian approximation ($\delta_1, \delta_2 \to 0$) can be determined without knowledge of G_j, but since $\delta_1, \delta_2 \propto j^{-1}$ we can only write

$$\sum_j G_j \delta = G \langle \delta \rangle$$

where $\langle \delta \rangle$ represents the average over j. Thus, in general, we have

$$\Delta A = GkT \left\{ - \ln \left(\Pi_x \lambda_x \right) + \frac{1}{2} \left[1 - \frac{2}{3} (\langle \delta_1 \rangle - 10 \langle \delta_2 \rangle) \right] \left[\sum_x \lambda_x^2 - 3 \right] \right.$$

$$\left. - \langle \delta_2 \rangle \left[\sum_x \lambda_x^4 - 3 \right] - \frac{2}{3} \langle \delta_2 \rangle \left[\sum_{x<y} \lambda_x^2 \lambda_y^2 - 3 \right] \right\} \quad (8)$$

Furthermore λ_z^2 refers to the reference state $\langle r^2 \rangle_*$. This can be cast in terms of the network deformation $\alpha_z^2 = \langle x^2 \rangle / \langle x^2 \rangle_i$ by

$$\lambda_z^2 = \eta \alpha_z^2$$

where

$$\eta = \langle x^2 \rangle_i / \langle x^2 \rangle_* = \langle r^2 \rangle_i / \langle r^2 \rangle_*$$

where $\langle r^2 \rangle_i$ is the mean-square end-to-end distance of the chains in the undeformed network; hence,

$$\Delta A = GkT \left\{ - \ln \left(\eta^{3/2} \Pi_x \alpha_x \right) + \frac{1}{2} \left[1 - \frac{2}{3} (\langle \delta_1 \rangle - 10 \langle \delta_2 \rangle) \right] \left[\eta \sum_x \alpha_x^2 - 3 \right] \right.$$

$$\left. - \langle \delta_2 \rangle \left[\eta^2 \sum_x \alpha_x^4 - 3 \right] - \frac{2}{3} \langle \delta_2 \rangle \left[\eta^2 \sum_{x<y} \alpha_x^2 \alpha_y^2 - 3 \right] \right\} \quad (9)$$

Consider now a simple elongation at constant volume, such that

$$\alpha_x = \alpha$$

$$\alpha_y = \alpha_z = \alpha^{-1/2}$$

Equation (9) then yields

$$\Delta A = GkT \left\{ -\frac{3}{2} \ln \eta + \frac{1}{2} \left[1 - \frac{2}{3} \left(\langle \delta_1 \rangle - 10 \langle \delta_2 \rangle \right) \right] \left[\eta \left(\alpha^2 + \frac{2}{\alpha} \right) - 3 \right] \right.$$

$$\left. - \langle \delta_2 \rangle \left[\eta^2 \left(\alpha^4 + \frac{2}{\alpha^2} \right) - 3 \right] - \frac{2}{3} \langle \delta_2 \rangle \left[\eta^2 \left(2\alpha + \frac{1}{\alpha^2} \right) - 3 \right] \right\}$$

and the retractive force $f = (\partial \Delta A / \partial \alpha)_{V,T} / L_i$, where L_i is the initial sample length, becomes

$$f = \frac{GkT}{L_i} \eta \left(\alpha - \frac{1}{\alpha^2} \right) \left\{ 1 - \frac{2}{3} \left(\langle \delta_1 \rangle - 10 \langle \delta_2 \rangle \right) - \frac{4}{3} \eta \langle \delta_2 \rangle \left(\frac{3\alpha^3 + 4}{\alpha} \right) \right\} \quad (10)$$

Since the internal-energy component f_e of the force f is given by[14]

$$f_e / f = -T [\partial \ln (f/T) / \partial T]_{V,L}$$

we have from eq. (10)

$$\frac{f_e}{f} = T \frac{d \ln \langle r^2 \rangle_*}{dT} \left\{ 1 + \frac{2}{3} \frac{d(\langle \delta_1 \rangle - 10 \langle \delta_2 \rangle)/dT}{d \ln \langle r^2 \rangle_* / dT} - \frac{4}{3} \eta \left(\frac{3\alpha^3 + 4}{\alpha} \right) \right.$$

$$\left. \times \left[\langle \delta_2 \rangle - \frac{d \langle \delta_2 \rangle / dT}{d \ln \langle r^2 \rangle_* / dT} \right] \right\} \quad (11)$$

Because experimental conditions are usually those of constant pressure and length, rather than constant volume and length, a means of conversion is required. It is easy to show that[14]

$$\frac{f_e}{f} = -T \left[\frac{\partial \ln (f/T)}{\partial T} \right]_{P,L} + \frac{VT}{f} \left(\frac{\partial f}{\partial V} \right)_{L,T} \beta$$

where $\beta = (\partial \ln V / \partial T)_{P,L}$ is the volume coefficient of thermal expansion. Thus from eq. (10), we find

$$\frac{f_e}{f} = -T \left[\frac{\partial \ln (f/T)}{\partial T} \right]_{P,L} - \frac{\beta T}{\alpha^3 - 1} - \frac{16\beta T}{3\alpha} \eta \langle \delta_2 \rangle \quad (12)$$

Discussion

As precise information on the form of the distribution G_j is lacking, two situations can be considered: the monodisperse distribution, and the most probable one. If all contour lengths are the same (monodisperse), $\langle \delta \rangle$ equals δ and is given by eq. (2). For the most probable distribution of contour lengths,[15] we have

$$G_j = (G/N) \lfloor 1 - (1/N) \rfloor^{j-1}$$

where N is the average of j, $N = \langle j \rangle$. Since $\delta \propto j^{-1}$, it follows that

$$\sum_{j=1}^{\infty} G_j(1/j) = G(\ln N/N) \qquad\qquad N \gg 1$$

hence

$$\langle \delta \rangle = \delta \ln N$$

where δ now refers to the average chain of N links. Thus, the most probable distribution augments δ by a factor $\ln N$ in the leading correction terms for non-Gaussian behavior. Real networks might probably fall between these two distribution extremes.

If is of interest to investigate the rate of convergence of the series expansion of ΔA. If the next order term were retained ($\delta_3 \propto j^{-2}$), summations such as

$$G\langle \delta_3 \rangle = \sum_{j=1}^{\infty} G_j \left(\frac{1}{j^2} \right)$$

would be required. Since no evaluation of this can be made for the most probable distribution, a rigorous analysis of convergence is precluded; but if it can be assumed that $\langle \delta_3 \rangle \propto N^{-2}$, it is probably sufficient to look only at the monodisperse case, bearing in mind that the most probable distributions will converge at a slower rate. In this instance, inclusion of δ_3 yields

$$\Delta A = GkT\{ - \ln (\eta^{3/2} \alpha_x \alpha_y \alpha_z) + A\eta[\alpha^2]$$
$$- B\eta^2[\alpha^4] - C\eta^3[\alpha^6] + D\eta^4[\alpha^8]\} + \text{constant} \qquad (13)$$

with

$$A = \frac{1}{2} \left[1 - \frac{2}{3} \delta_1 + \frac{20}{3} \delta_2 - 70\delta_3 - \frac{2}{3} \delta_1^2 + 10\delta_1\delta_2 - \frac{100}{3} \delta_2^2 \right]$$

$$B = \delta_2 - 21\delta_3 - \frac{1}{6} \delta_1^2 + \frac{13}{3} \delta_1\delta_2 - 19 \delta_2^2$$

$$C = \frac{5}{9} [9\delta_3 - 3\delta_1\delta_2 + 30\delta_2^2]$$

$$D = \frac{35}{6} \delta_2^2$$

$$[\alpha^2] = \alpha_x^2 + \alpha_y^2 + \alpha_z^2$$

$$[\alpha^4] = \alpha_x^4 + \alpha_y^4 + \alpha_z^4 + \frac{2}{3} (\alpha_x^2\alpha_y^2 + \alpha_x^2\alpha_z^2 + \alpha_y^2\alpha_z^2)$$

$$[\alpha^6] = \alpha_x^6 + \alpha_y^6 + \alpha_z^6 + \frac{3}{5} (\alpha_x^4\alpha_y^2 + \alpha_x^4\alpha_z^2 + \alpha_x^2\alpha_y^4$$
$$+ \alpha_x^2\alpha_z^4 + \alpha_y^4\alpha_z^2 + \alpha_y^2\alpha_z^4) + \frac{2}{5} \alpha_x^2\alpha_y^2\alpha_z^2$$

$$[\alpha^8] = \alpha_x{}^8 + \alpha_y{}^8 + \alpha_z{}^8 + \frac{4}{7}(\alpha_x{}^6\alpha_y{}^2 + \alpha_x{}^6\alpha_z{}^2 + \alpha_z{}^2\alpha_y{}^6$$

$$+ \alpha_x{}^2\alpha_z{}^6 + \alpha_y{}^6\alpha_z{}^2 + \alpha_y{}^2\alpha_z{}^6) + \frac{18}{35}(\alpha_x{}^4\alpha_y{}^4 + \alpha_z{}^4\alpha_z{}^4$$

$$+ \alpha_y{}^4\alpha_z{}^4) + \frac{12}{35}(\alpha_x{}^4\alpha_y{}^2\alpha_z{}^2 + \alpha_z{}^2\alpha_y{}^4\alpha_z{}^2 + \alpha_x{}^2\alpha_y{}^2\alpha_z{}^4)$$

Consider the flexibly jointed (random) chain. Flory[16] gives

$$\langle r^2 \rangle_0 = \langle r^2 \rangle_* = Nb^2$$

$$\langle r^4 \rangle_0 = [(5/3)N(N-1) + N]b^4$$

$$\langle r^6 \rangle_0 = [(35/9)N(N-1)(N-2) + 7N(N-1) + N]b^6$$

Thus,

$$A = (1/2)[1 - (1/N) - (11/4N^2)]$$

$$B = -(3/20N)[1 + (137/20N)]$$

$$C = 29/56N^2$$

$$D = 21/160N^2$$

Clearly, convergence at large N (Ca. 100) is rapid. When $N \to \infty$ the Gaussian result is obtained. For smaller N only the terms in N^{-1} need be retained to yield the leading correction terms for non-Gaussian behavior. When real chains are considered, the situation is somewhat different. Nagai[17] has calculated the moments of polyethylene (including correlated internal rotations) up to $\langle r^{12} \rangle_0$. Using his results we have approximately

$$A = (1/2)[1 - (16.7/N) + (1403/N^2)]$$

$$B = -(1/N)[3.4 + (408.5/N)]$$

$$C = 228/N^2$$

$$D = 70/N^2$$

Here a few thousand units are required for rapid convergence, but this will amount to only Ca. 100 "statistical" links. It is observed that for 100 real links the N^{-1} and N^{-2} terms in A and B above are of the same magnitude. At first glance it would appear that there is no particular advantage in going beyond the Gaussian approximation. Such a conclusion is, however, erroneous. To show this we calculate the force from eq. (13) in the region of small strain $\epsilon = \alpha - 1$ for a simple elongation. We find

$$f \sim (3GkT/L_i)[1 + (14/N) + (5750/N^2)]\epsilon$$

When $N = 100$, there is a rapid buildup of the higher order terms resulting in a severe challenge to the Gaussian result. Thus, unless convergence is assured the theory including the usual Gaussian result is completely invalid.

Application is justified only for rapid convergence. This requires, in the case of polyethylene, very large N. For more common elastomers such as polyisoprene we expect a considerably smaller value of N to meet these conditions. Once rapid convergence is assured, the Gaussian approximation is applicable at low extensions. Higher elongations necessitate the retention of terms in N^{-1}, and still higher deformations require N^{-2}, etc. If crosslinking is so tight that such a progression does not occur, the entire theory is inapplicable, including the Gaussian result. With these remarks in mind, we present in the following paragraphs a discussion of only the leading correction terms (N^{-1}) with the understanding that N is so large and α so small that all higher order terms can be neglected.

In order to gain better insight into the theory, it is necessary to consider the influence of δ_1, δ_2 in some detail. Miyake and Sakakibara[18] have derived the fourth moment $\langle r^4 \rangle_0$ of chains having fixed bond angles θ and angles of internal rotation φ. For polyethylene type chains having independent rotation, their result is

$$\langle r^4 \rangle_0 = \frac{5N^2 b^4}{3} \left[\frac{(1-\sigma)(1-\gamma)}{(1+\sigma)(1+\gamma)} \right]^2 + \frac{4N b^4}{9(1-\omega)} \left[\frac{(1-\sigma)(1-\gamma)}{(1+\sigma)(1+\gamma)} \right]^2$$

$$+ \frac{2N b^4}{9} \frac{(1-\sigma)(1-\gamma)}{(1+\sigma)^3(1+\gamma)^3} [\sigma^2 + 42\sigma - 11 - 4(\sigma^2 + 6\sigma - 21)\gamma$$

$$- (3\sigma^2 - 42\sigma + 7)\gamma^2] \quad (14a)$$

$$\langle r^2 \rangle_0 = N b^2 \left[\frac{(1-\sigma)(1-\gamma)}{(1+\sigma)(1+\gamma)} \right] + 2b^2 \left[\frac{\sigma + \gamma(2+\gamma\sigma)}{(1+\sigma)^2(1+\gamma)^2} \right] \quad (14b)$$

where $\sigma = \cos\theta$, $\gamma = \langle \cos\varphi \rangle$, $\omega = \langle \cos^2\varphi \rangle$. Therefore,

$$\delta_1 = \frac{3[\sigma + \gamma(2 + \gamma\sigma)]}{N(1 - \sigma^2)(1 - \gamma^2)} \quad (15)$$

$$\delta_2 = \frac{1}{20N} \left\{ \frac{1}{1-\omega} + \frac{1}{(1-\sigma^2)(1-\gamma^2)} [\sigma^2 + 12\sigma - 11 - \right.$$

$$\left. 4(\sigma^2 + 6\sigma - 6)\gamma - (3\sigma^2 - 12\sigma + 7)\gamma^2] \right\}$$

with φ so defined that the *trans* conformation is denoted by $\varphi = \pi$. When the *gauche* conformations occur at $\varphi = \pm \pi/3$ it is well known that

$$\gamma = \frac{-1 + \exp\{-\Delta E/kT\}}{(1 + 2\exp\{-\Delta E/kT\})}$$

$$\omega = \frac{2 + \exp\{-\Delta E/kT\}}{2(1 + 2\exp\{\Delta E/kT\})} \quad (16)$$

where $\Delta E = E_{(gauche)} - E_{(trans)}$, so that for polyethylene type chains $\omega = {}^1\!/_2(1 - \gamma)$.
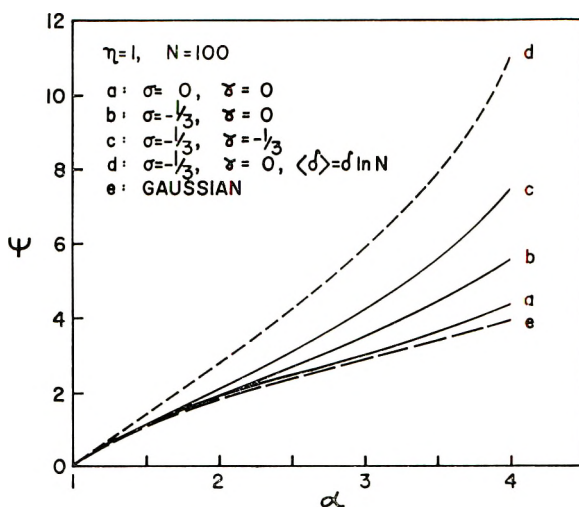
Fig. 1. $\psi = f/(GkT/L_i)$ vs. α for various model chains.

For a random chain, we have $\sigma = 0$, $\gamma = 0$, $\omega = 1/2$ and $\delta_1 = 0$, $\delta_2 = -3/20N$, a result given earlier by Smith, Ciferri, and Hermans.[10] For a fixed bond angle of $\theta = 109°$ and free internal rotation, the relations are $\sigma = -1/3$, $\gamma = 0$, $\omega = 1/2$ and

$$\delta_1 = 3\sigma/[N(1 - \sigma^2)]$$

$$= -9/8N$$

$$\delta_2 = (1/20N)\{[2/(1 - \omega)] + [(\sigma^2 + 12\sigma - 11)/(1 - \sigma^2)]\}$$

$$= -51/80N.$$

and for the special case of $\gamma = -1/3$ (corresponding to $\Delta E \simeq 600$ cal/mole), $\sigma = -1/3$, $\delta_1 = -63/16N$ and $\delta_2 = -111/80N$.

The influence of these restrictions on the stress-strain curve is illustrated in Figure 1. Here $\psi = f/(GkT/L_i)$ is plotted versus α for the three model chains above. In addition, a comparison between the monodisperse distribution and the most probable distribution is shown for the case of fixed bond angles but unrestricted internal rotation (curves a and d). The results are quite sensitive to the model and assumptions employed, particularly with regard to the form of G_j. Deviations from Gaussian behavior can be so great, even at very low extensions, that the Gaussian approximation may be invalidated in all but the most loosely crosslinked systems. It is pointed out also that the sensitivity of the results to the contour distribution can be altered if λ is a function of j. It is, after all, only an assumption that all λ are equal. In fact, a chain of short contour length cannot be stretched by the same amount as a longer one—the maximum deformation ratio is proportional to $j^{1/2}$. This would require that short chains be stretched less and the long ones more, the result being that

the system probably moves towards the direction of the behavior of a network composed of average chains (monodisperse distribution), but probably not exactly so. It may well be that this is at the origin of the well known deviations from Gaussian theory as exemplified by the Mooney-Rivlin phenomenological equation.

To investigate the thermoelastic properties of the network, it is necessary to obtain $d\delta/dT$ and $d\ln\langle r^2\rangle_*/dT$. From eq. (13)

$$\frac{d\ln\langle r^2\rangle_*}{dT} = -\frac{2}{(1-\gamma^2)}\frac{d\gamma}{dT}$$

Thus,

$$\frac{d\delta_1/dT}{d\ln\langle r^2\rangle_*/dT} = -\frac{3(1+2\sigma\gamma+\gamma^2)}{N(1-\sigma^2)(1-\gamma^2)}$$

$$\frac{d\delta_2/dT}{d\ln\langle r^2\rangle_*/dT} = -\frac{1}{20N}\left\{\frac{(1-\gamma^2)}{(1-\omega)^2}\frac{d\omega}{d\gamma} - \frac{1}{(1-\sigma^2)(1-\gamma^2)}[2(\sigma^2+6\sigma\right.$$

$$\left. -6) + (\sigma^2-24\sigma+19)\gamma + 2(\sigma^2+6\sigma-6)\gamma^2]\right\}$$

and for

$$\zeta = \delta_2 - \frac{d\delta_2/dT}{d\ln\langle r^2\rangle_*/dT} = \frac{1}{20N}\left\{\frac{1}{(1-\omega)}\left[\frac{(1-\gamma^2)}{(1-\omega)}\frac{d\omega}{d\gamma} + \frac{1+5\gamma}{1-\gamma}\right]\right\}$$

or since $\omega = (1-\gamma)/2$

$$\zeta = (1/20N)[(1+\gamma)/(1-\gamma)]$$

which is nonzero for $\gamma > -1$. This means that in general f_e/f will be a function of elongation, particularly at large degrees of stretch. As $\gamma \to -1$, $\zeta \to 0$, and as $\gamma \to \frac{1}{2}$, $\zeta \to 9/20N$ (if the most probable distribution is used ζ must be multiplied by $\ln N$). Thus, when δ_2 contributes most to the stress–strain behavior, ζ contributes the least to f_e/f, and vice versa. Put another way, these results indicate that a polymer for which f_e/f is negative will be sensitive to non-Gaussian behavior as far as the stress is concerned, but less so for f_e/f. The reverse is true when f_e/f is positive.

Because ζ is always positive, f_e/f will either decrease or increase with elongation, depending upon whether ΔE is positive or negative. Polyethylene, for example, should show an increase in f_e/f at large deformations provided crystallization is prohibited. If the same model can be applied to rubber, one deduces that f_e/f should decrease with elongation. In this regard it is of interest to examine some published data. Figure 2 shows a plot of the experimental values of f_e/f for rubber, reported by Smith, Greene, and Ciferri,[7] versus $(3\alpha^3+4)/\alpha$. According to eq. (11), such a plot should be linear. The rapid downturn at large α as shown in the figure was detected by x-rays to be due to crystallization. Before this region is reached,
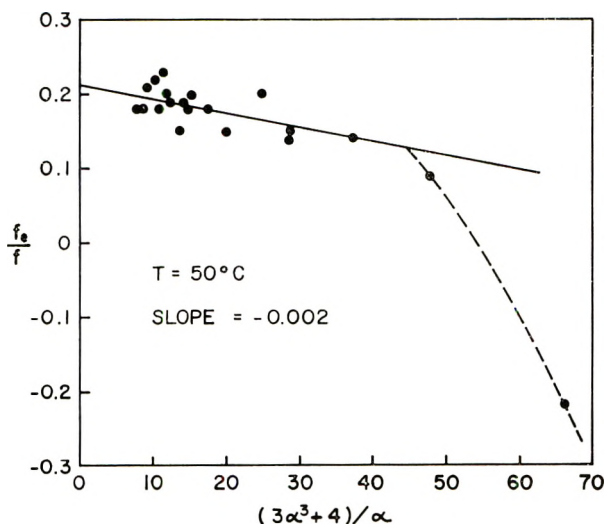
Fig. 2. f_e/f as a function of $(3\alpha^3 + 4)/\alpha$.   Data from Smith, Green and Ciferii.[7]

however, there appears a definite decreasing trend with increasing α.   If we draw a straight line as shown in the figure, the slope [eq. (11)] is

$$\text{slope} = -\ T\ \frac{d\ \ln \langle r^2 \rangle_*}{dT} \frac{4}{3} \eta \zeta = -\left(\frac{f_e}{f}\right)_* \frac{4}{3} \eta \zeta$$

The point at $\alpha \approx 4$ is not considered for the line, since crystallization begins at about this deformation; hence, this point might be a little low.   Whereas the chain geometry considered herein should not be applied to polyisoprene, one should nevertheless expect an order-of-magnitude agreement by doing so.   Using the most probable distribution,

$$\zeta = 3 \ln N/20N)[(1 + \gamma)/(1 - \gamma)]$$

and $\eta \sim 1$, $\gamma \gtrsim 0$, $(f_e/f)_* \simeq 0.2$, $\ln N \sim 5$, we find

$$N \approx -\frac{0.2}{\text{slope}} \approx 100$$

The actual value of N is not known, but Smith, Greene, and Ciferri[7] estimate it to be 100–150.   In view of the uncertainties the agreement is excellent.   Had the monodisperse distribution been used, our estimate would drop to $N \approx 20$.   Thus, considerable support for the most probable distribution is gained.

The effect of swelling can be incorporated into the foregoing equations by replacing η with $\langle r^2 \rangle_i / \langle r^2 \rangle_* v^{-2/3}$, where v is the volume fraction of polymer. It is of interest to note that measurements of f_e/f of two highly swollen systems are in general accord with the theory.   A re-analysis of the published data for rubber swollen in hexadecane[19] reveals that a slight decrease of f_e/f with elongation might be occurring.   On the other hand, f_e/f

for poly(vinyl alcohol) networks swollen in water shows a consistent increase with elongation.[20] Since f_e/f in this case is negative, this is again in qualitative agreement with our theory. However, since the range of deformation is small, too much should not be made of these conclusions.

Finally, it is pointed out that the logarithmic term appearing in eq. (9) is in dispute. Our result is in accord with the theory of Hermans.[5] Flory, on the other hand, believes a coefficient of $1/2$ is required, and James and Guth do not admit to its presence at all. We should perhaps include a factor p in this term which might range $0 \leqslant p \leqslant 1$ in order to include all possibilities.

References

1. F. T. Wall, *J. Chem. Phys.*, **10**, 132, 485 (1942); *ibid.*, **11**, 527 (1943).
2. W. Kuhn and F. Grün, *J. Polym. Sci.*, **1**, 183 (1946).
3. F. T. Wall and P. J. Flory, *J. Chem. Phys.*, **19**, 1435 (1951).
4. H. M. James and E. Guth, *J. Chem. Phys.*, **11**, 455 (1943); *J. Polym. Sci.*, **4**, 153 (1949); *J. Chem. Phys.*, **21**, 1039 (1953).
5. J. J. Hermans, *Trans. Faraday Soc.*, **43**, 591 (1947); *J. Polym. Sci.*, **58**, 191 (1962).
6. K. J. Smith, and Jr. and D. Puett, *J. Appl. Phys.*, **37**, 346 (1966).
7. K. J. Smith, Jr., A. Greene, and A. Ciferri, *Kolloid-Z.*, **194**, 49 (1964).
8. K. Nagai, *J. Chem. Phys.*, **45**, 838 (1966).
9. M. C. Wang and E. Guth, *J. Chem. Phys.*, **20**, 1144 (1952).
10. K. J. Smith, Jr., A. Ciferri, and J. J. Hermans, *J. Polym. Sci. A*, **3**, 1025 (1964).
11. M. V. Volkenstein and D. B. Ptitsyn, *Zh. Tekh. Fiz.*, **25**, 649 (1955).
12. K. Nagai, *J. Chem. Phys.*, **38**, 924 (1963).
13. S. Chandrasekhar, *Rev. Mod. Phys.*, **15**, 1 (1943).
14. C. A. J. Hoeve and P. J. Flory, *J. Polym. Sci.*, **60**, 155 (1962).
15. K. W. Scott and R. S. Stein, *J. Chem. Phys.*, **21**, 1281 (1953).
16. P. J. Flory, *Statistical Mechanics of Chain Molecules*, Wiley, New York, 1969.
17. K. Nagai, *J. Chem. Phys.*, **48**, 5646 (1968).
18. A. Miyake and M. Sakakibara, *J. Phys. Soc. Japan*, **17**, 164 (1962).
19. J. Bashaw and K. J. Smith, Jr., *J. Polym. Sci.*, *A-2*, **6**, 1041 (1968).
20. J. Bashaw and K. J. Smith, Jr., *J. Polym. Sci. A-2*, **6**, 1051 (1968).

Glass Transition in Ionic Polymers: The Acrylates*

A. EISENBERG, H. MATSURA,† and T. YOKOYAMA,‡

McGill University, Montreal, Canada

Synopsis

It is shown that the glass transition temperatures of the ionic acrylates are subject to the same correlation as found for the phosphates, silicates, and ionenes; the equation is $T_g = 730 \ (q/a) - 67$, where q is the cation charge and a the separation between centers of charge for the cation and anion.

Introduction

In two glass transition studies involving inorganic anions,[1,2] it was shown that a plot of the glass transition temperature against the ratio of the cation charge q to the distance between centers of charge of the cation and anion a yielded a linear relation.   The reason for the observed linearity was believed to lie in the relation between the transition temperature and the electrostatic work necessary to remove an anion from the coordination sphere of a cation (or the converse) which, for any one polymer system, reduces to q/a.   In a subsequent study[3] it was shown that, within a rather high experimental error (due to the short range of q/a values accessible experimentally), the aliphatic ionenes also are subject to this correlation. The three systems studied to date, along with the corresponding equations are:

Polyphosphates:

$$T_g = 625 \ (q/a) - 12 \tag{1}$$

Silicates:

$$T_g = 635 \ (q/a) + 132 \tag{2}$$

Aliphatic ionenes:

$$T_g = 695 \ (q/a) - 23 \tag{3}$$

In this work, an attempt was made to see whether such a relation also applies to the acrylates.   We found that it does, the result being

$$T_g = 730 \ (q/a) - 67 \tag{4}$$

หองสมุด กรมวิทยาศาสตร

Experimental

The poly(acrylic acid) used in this study was prepared by free-radical polymerization of the monomer in toluene at ca. 50°C with benzoyl peroxide as a catalyst with conversions up to 80%. Samples of three molecular weights were used, i.e., 20,000, 231,000, and 472,000, the values being calculated from intrinsic viscosities measured in dioxane at 30°C on the basis of published correlations.[4] No significant differences were found in the T_g behavior for these three samples. The polymer was dried under vacuum at 80–100°C to constant weight and stored under dry nitrogen. Distilled water or commercial formamide were used as plasticizers without further purification.

Because of the very high glass transition of the salts and the great difficulty of obtaining them in the dry state, all the glass transitions were determined as a function of plasticizer content (water or formamide) and extrapolation to zero plasticizer content. The extrapolation procedure was based on the equation[5]

$$T_g = w_1 T_{g_1} + w_2 T_{g_2} - K w_1 w_2 \tag{5}$$

where the subscripts 1 and 2 refer to polymer and plasticizer, respectively, and K is treated as an adjustable parameter. A plot of $(T_{g_1} - T_{g_2})/w_1$ versus w_1 or w_2 yields the glass transition of the pure material by simple linear extrapolation. Equation (5) was used because of its convenience rather than for any theoretical reasons. Other equations with one adjustable parameter were also tried and gave the same extrapolated glass transition, within experimental error.

The glass transition temperatures were measured in a Beckmann DSC I instrument with a scanning speed of 10°C/min. Samples were prepared by dissolving known amounts of dry PAA in the appropriate solvent and evaporating to a predetermined weight. Samples of poly(sodium acrylate) and the other completely neutralized salts were prepared by titrating the acid to a phenolphthalein endpoint with NaOH, KOH, CsOH, Ca(OH)$_2$, or mixtures of bases and again evaporating excess plasticizer. Partly, neutralized samples were prepared by adding a precalculated amount of the base to a solution of the acid of known concentration and evaporating to a predetermined weight.

Results

A plot of the glass transition temperature of poly(sodium acrylate) as a function of water content is shown in Figure 1, and a summary of all the extrapolated results is given in Table I. Table I also lists values of q/a for each sample; q is given in units of one electron and a (in Ångstrom) is simply the sum of the ion radii.[1] An approximate method used to obtain a took the following factors into account. While the crystal structures of several sodium phosphates and carboxylate salts are known, no detailed information is available for the structures of the glasses. However, crystal
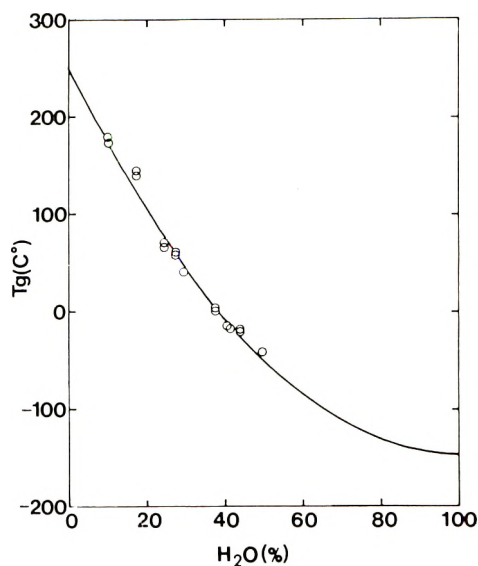
Fig. 1. Glass transition of poly(sodium acrylate) plasticized with water as a function of the water content.

TABLE I
Extrapolated Values of T_g, q/a, and K for Various Polymer–Plasticizer Systems

Polymer	Plasticizer	T_{g1}, °C	q/a	K
Poly(acrylic acid)	Formamide	102	0	−205
"	Water	102	0	−223
20% Na salt	"	108	0.085	−233
40% "	"	132	0.170	−262
60% "	"	162	0.255	−298
80% "	"	198	0.340	−338
Poly(sodium acrylate)	"	251	0.425	−407
"	Formamide	250	0.425	−537
Poly(potassium acrylate)	Water	194	0.366	−556
50% Na⎱ acrylate 50% K ⎰	"	219	0.396	−464
25% Ca⎱ acrylate 75% Na⎰	"	287	0.484	−312
Poly(cesium acrylate)	"	174	0.323	−447

structure information is not helpful here, since we are dealing with charge delocalization in both the phosphate and carboxylate systems. Most probably, the distance between centers of charge is greater than the sum of the radii of the cation and singly charged oxygen anion, but smaller than the internuclear distance between the cation and the carbon (or phosphorus) atom carrying the two oxygens. Thus, in the absence of more quantitative information, a was taken as the sum of the radii of the cation and the doubly charged oxygen anion (i.e., 1.4 Å) for both the phosphate and acrylate

systems.   This naturally introduces some inaccuracy which is reflected in
the precise value of the T_g versus q/a slope; the method is, however, self-
consistent for each system.   The method of calculation of q/a for mixed
salts for partly neutralized samples has been given before.   Figure 2
Shows a plot of T_g versus q/a for all the samples studied to date, indicating
the great similarity of all the systems.
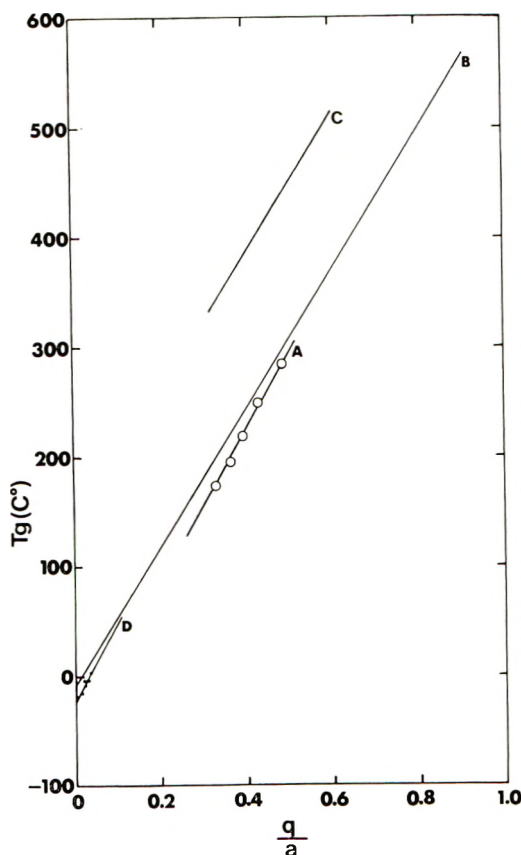
Fig. 2. Glass transition of (A) poly(sodium acrylate) plotted against q/a; also shown are
the results for (B) the polyphosphates[1], (C) silicates,[2] and (D) ionenes.[3]

The value found for poly(sodium acrylate) is very close to that of Otocka
and Kwei,[6] who estimate it to be $230°C$.   These authors obtained their
estimate by extrapolating the glass transitions of copolymers of ethylene-
sodium acrylate to zero ethylene content.
Several points are noteworthy.   While in the poly-phosphate series the
partly neutralized polyacid yielded points which fell on the q/a versus T_g
plot for the completely neutralized salts, this is not the case with the acry-
lates; the extrapolated value for $q/a = 0$ is -67, whereas the glass transi-
tion temperature of PAA is 102–$106°C$.[7]

The most reasonable explanation for this fact lies in the formation of highly structured acid dimers or higher oligomers in the acrylate case. Although hydrogen bonding with sites on the repeat unit not involving the hydroxyl groups is possible in the phosphoric acid, this is not true in the case of acrylic acid. Since two hydrogen bonds are formed per acid dimer in the acrylates, this pair would probably be stable to higher temperatures than a hydrogen-bonded species involving only one hydrogen bond, thus giving PAA its abnormally high T_g.

As can be seen in Figure 2, the phosphates, ionenes, and acrylates all fall close to the same line on the plot; the plot for the silicates has the same slope but a higher intercept, possibly due to the presence of two ions per repeat unit in the silicates. The similarity of the slope for all these polymers suggests that we may be dealing with a universal parameter, the full significance of which is not clear as yet. From a practical point of view, if the slope of 625–730 is observed in other systems also, it would make the estimation of glass transitions for ionic polymers exceedingly easy; the knowledge of only one glass transition for one q/a value would allow the prediction of all the others, especially for completely ionized systems and for those partly ionized systems in which highly structured oligomers are not observed.

References

1. A. Eisenberg, H. Farb, and L. G. Cool, *J. Polym. Sci. A-2*, **4**, 855 (1966).

2. A. Eisenberg and K. Takahashi, *J. Noncryst. Solids*, **3**, 279 (1970).

3. A. Eisenberg, H. Matsuura, and T. Yokoyama, *Polym. J. (Japan)*, **2**, 117 (1971).

4. S. Newman, W. R. Krigbaum, C. Langier, and P. J. Flory, *J. Polym. Sci.*, **14**, 451 (1954).

5. E. Jenckel and R. Hensch, *Kolloid Z.*, **130**, 89 (1953).

6. E. P. Otocka and T. K. Kwei, *Macromolecules*, **1**, 401 (1968).

7. A. Eisenberg, T. Yokoyama, and E. Sambalido, *J. Polym. Sci. A-1*, **7**, 1717 (1969).

Structural Evaluation of Branched Polyethylene by Combined Use of GPC and Gradient-Elution Fractionation*

L. WILD, R. RANGANATH, and T. RYLE, *U.S. Industrial Chemicals Co., Research Division, Cincinnati, Ohio 45237*

Synopsis

A method is described and a computer program outlined whereby gel-permeation chromatographic analysis of fractions from gradient-elution fractionation of branched polyethylenes provides a complete molecular weight evaluation of each fraction and the parent resin. The procedure involves the use of the universal calibration concept of Benoit et al. in a way that eliminates the ambiguities present in attempts to apply it directly to whole polymers. The resultant molecular weight data for fractions, when related to their solution viscosity and low-shear melt viscosity and to their infrared analysis, provides a total structural evaluation of a branched polyethylene resin, including molecular weight, molecular weight distribution and the distribution of both long- and short-chain branching. The potential of this method for providing a comprehensive structural evaluation of branched polyethylene is illustrated by examples of its application in the analysis of some commercial resins.

INTRODUCTION

Some of the most complex and varied branched structures to be found in synthetic polymers are present in polyethylenes manufactured by a high-pressure, free-radical process. This is because the very flexible polyethylene chain radical may undergo intermolecular or intramolecular chain transfer leading to both long- and short-chain branching. The wide variety of manufacturing conditions used in the production of commercial polyethylene insures a broad spectrum of branched structures of varying degree and distribution of the two types of branches.

Over the years it has become increasingly apparent that if one hopes to derive substantial practical benefit from a study of branched polyethylene structure it will be necessary to define a total structure including molecular weight, molecular weight distribution, the degree of long- and short-chain branching and the distribution of both types of branching among the molecular species present in a particular resin. In this paper, an approach to a total structure evaluation is described through the combined use of gradient-elution fractionation and gel-permeation chromatography (GPC).

* Paper presented at 161st National Meeting, American Chemical Society, Los Angeles, Calif., March 1971.

2137

The objective is to achieve a relatively large-scale separation of molecular species according to their molecular weight by a preparative gradient-elution fractionation and then subject the resultant fractions to analysis by GPC, solution viscosity, and infrared absorption. From the measurement of solution viscosity and GPC analysis, one may derive molecular weight, molecular weight distribution, and degree of long-chain branching by application of Benoit's universal calibration concept.[1] The melt viscosity measurements will provide an additional estimation of the degree of long-chain branching and some further insight as to its influence on melt-flow characteristics. The methyl content of the various fractions from infrared measurements will allow a direct evaluation of the short-chain branching distributions.

The ability to derive molecular weights of branched polyethylene fractions (and whole polymers) from GPC data and intrinsic viscosity $[\eta]$ through the universal calibration provides the foundation of the present approach to resin structure. A detailed description is thus given of the procedure used to determine molecular weights unambiguously from such information. The success of the method is demonstrated by comparing computed and measured molecular weights for selected samples. An outline of the data obtained for a wide range of commercial resins is included in order to illustrate the scope and effectiveness of this relatively rapid evaluation of the branched structure of high-pressure polyethylenes.

EXPERIMENTAL

Gradient-Elution Fractionation

Preparative fractionation of polyethylene resins was carried out by using a gradient-elution column technique.[2] Polymer (15 g) was loaded on the Chromosorb-P column packing by cooling from hot xylene solution. A continuous, exponential solvent gradient was employed at 115°C with 70:30 and 20:80 mixtures of xylene and ethylene glycol monoethyl ether (Ethyl Cellosolve) as solvent and nonsolvent. The samples precipitated in acetone were suitably combined to give approximately twenty 0.5–1.0 g fractions.

Gel-Permeation Chromatography

Gel-permeation chromatography (GPC) data were obtained using a Waters Model 200 GPC instrument equipped with an automatic injection system. Measurements were made in 1,2,4-trichlorobenzene at 140°C with a four-column system (10^6, 10^5, 10^4, 10^4 Å) having a plate count of 700 plates/ft. Samples (0.1% and 0.25%, w/v) were injected for 1 and 2 min for fractions and whole polymers, respectively. The linear polyethylene calibration curve (counts C versus molecular weight M) was established by using NBS linear polyethylene standard reference material No. 1475 (see Appendix). No correction for skewing or instrument spreading effects was made. In the calculation of the number-average ($\bar{M}_n$) and weight-average

$(\bar{M}_w)$ molecular weights from GPC data, peak heights were read at each quarter (1.25 ml) or fifth (1 ml) of a count. Standard methods were then used to calculate the different molecular weight averages of the samples.

The universal calibration (C_w versus $[\eta]\bar{M}_w$) was established with linear polyethylene fractions obtained by gradient-elution fractionation of the NBS #1475. Weight-average molecular weights $\bar{M}_w$ were determined by application of the above linear PE calibration to the GPC analysis of individual fractions. The resulting curve proved virtually indistinguishable from that of C_w versus $[\eta]\bar{M}_w$ derived from polystyrene GPC standards.

Osmometry

The number-average molecular weights were measured by osmometry in toluene at 86°C by using a Hallikainen automatic membrane osmometer with gel cellophane 600 membrane.

Light Scattering

Determination of the weight-average molecular weight by light scattering was carried out by using the Sofica photogoniodiffusometer. The measurements reported here were made on solutions of polyethylene fractions in α-chloronaphthalene at 135°C by using unpolarized 5460 Å radiation. The rate of change of refractive index with concentration was taken to be -0.191 at 135°C. Clarification of the solutions was achieved by filtering the solution through a combined mat of Millipore Solvinert membranes of two different pore sizes, viz. 0.25 μ and 0.45 μ. The zero-angle, zero-concentration intercept of the Zimm plot is directly related to the molecular weight of the polymer.

Solution Viscosity

Solution viscosity of branched polymers was determined as inherent viscosity $\{\eta\}$ for 0.1% solutions in trichlorobenzene at 140°C. For linear polyethylene fractions used in establishing the universal calibration, those with solution viscosities >2.0 were determined as intrinsic viscosities $[\eta]$. Below this viscosity level inherent and intrinsic viscosity values are indistinguishable.

Low-Shear Melt Viscosity

Melt viscosity η_0 was determined at 190°C on small samples (ca. 0.3 g) by the capillary method of McGlammery and Harban.[3] This measurement is carried out under conditions leading to average shear rate in a range of 10^{-1} to 10^{-2} sec^{-1}, and η_0 is considered to approximate a zero-shear melt viscosity.

Melt viscosities in the range of 10^7–10^9 poise were determined by blending the fraction with a low viscosity polyethylene diluent and extrapolating the log η_0 versus per cent composition line to zero diluent composition.

Molecular Weight Evaluation from GPC Data

It is clear that GPC provides what is essentially size distribution data. The conversion to molecular weight distribution data is therefore complicated by the fact that the GPC elution volume reflects both molecular weight and degree of long-chain branching. Benoit et al. concluded[1] that the parameter $[\eta]M$ provides a measure of the hydrodynamic volume of polymer molecules. If $[\eta]$ is the intrinsic viscosity of any polymer species in the same solvent and at the same temperature as is used in the operation of the GPC, the parameter, $[\eta]M$, will be directly related to the appearance volume of any and all molecular species. A calibration of the GPC instrument in terms of $[\eta]M$ will thus be universal, with the $[\eta]$ component taking into account the influence of chain structure and polymer–solvent interactions on the hydrodynamic volume of the polymer. Work in this laboratory[4] confirmed that this universal calibration concept of Benoit et al. describes the influence of long-chain branching on the GPC separation of branched polyethylenes.

Although very satisfying from a theoretical standpoint, in practice it is found that the application of the universal calibration for branched polymers is not simple. The difficulty arises from the fact that in order to convert the calibration curve based on $[\eta]M$ to the required molecular weight calibration it is necessary to know the solution viscosity of each molecular weight species in each whole-polymer sample. The approach that has been taken to overcome this problem is to subject the parent resin to gradient-elution fractionation and then to determine the solution viscosity of a number of the resulting fractions. In principle, this allows a simple extraction of molecular weight from the $[\eta]M$ versus elution volume (count number C) relation.

Even this very direct approach to the use of the universal calibration concept for branched polyethylenes is complicated by the fact that the fractionated samples derived from the elution fractionation method are far from monodisperse, especially in the region of high molecular weight. This raises two uncertainties. The first arises from the necessity of using some average molecular weight for the fraction, as it is not possible to talk of *the* molecular weight. Secondly, assuming that it is known what particular average is applicable in this type of analysis, one still needs to derive the actual elution volume, from the GPC trace, which corresponds to this average molecular weight value.

From practical considerations it becomes clear that the weight-average molecular weight is the most suitable to use in deriving the universal calibration curve, viz., count number C_w vs. $[\eta]\bar{M}_w$. To determine the C_w which truly denotes the point of elution of a species which has a volume parameter of $[\eta]\bar{M}_w$, the following method has been devised. It is first assumed that the branched resin under study is in fact linear in nature and each of the fractions is analyzed by using the calibration derived by analyzing on the GPC the NBS Standard Reference Material #1475.

Schematic Outline of Computer Program
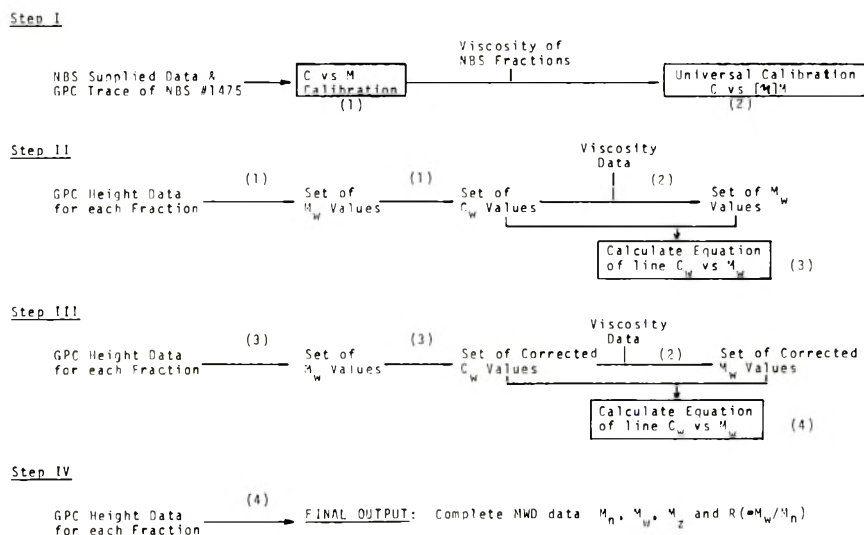
Fig. 1. Schematic outline of computer program. Numbers in parenthesis denote the calibration equation used at each stage.

From this calibration curve of C versus M, one obtains the corresponding C_w for each fraction. However, using this initial C_w value in conjunction with the universal calibration curve (C_w versus $[\eta]\bar{M}_w$) and the measured solution viscosity, one may obtain a value for $\bar{M}_w$. This value for $\bar{M}_w$, which will be somewhat lower than the true $\bar{M}_w$ value for the branched fractions, is then used to achieve a workable molecular weight calibration curve, C_w versus $\bar{M}_w$. This relationship partially takes into account the influence of long-chain branching on the elution volume. This first-generation calibration curve is now used to recompute an apparent MWD for each of the fractions and provides values for $\bar{M}_w$ which approach even more closely the true $\bar{M}_w$.

The improved $\bar{M}_w$ values are used to read off the corresponding C_w values from the applicable C_w versus $\bar{M}_w$ relationship and the improved C_w value used to derive once again a value of $\bar{M}_w$ from the universal calibration. The above process is repeated by using the resulting new C_w versus $\bar{M}_w$ calibration curve. This iterative process may be continued until the values for $\bar{M}_w$ computed from the original GPC traces do not change appreciably.

The procedure described above, which is used to take account of polydispersity of the component fractions, has been programmed for the computer. A schematic presentation of the procedure is outlined in Figure 1. The resulting, unique calibration curve for each resin will provide molecular weight distribution (and all the molecular weight averages) for each of the fractions analyzed and also for the whole polymer.

Determination of Degree of Branching

Long-Chain Branching.   The degree of long-chain branching is defined by the branching index λ:

$$\lambda = m/M,$$

where m is the number of branch units per chain and M is the molecular weight.   For polymers with trifunctional branch points, the number of branches may be derived by the equations of Zimm and Stockmayer,[5]

$$g = [1 + (m/7)]^{1/2} + (4m/9)^{-1/2}$$

for monodisperse systems, and

$$\langle g \rangle_w = \frac{6}{n_w} \left\{ 1/_2 \frac{(2 + n_w)^{1/2}}{(n_w)^{1/2}} \ln \left[\frac{(2 + n_w)^{1/2} + (n_w)^{1/2}}{(2 + n_w)^{1/2} - (n_w)^{1/2}} \right] - 1 \right\}$$

for polydisperse systems, where n_w is the weight-average number of branches and g is the ratio of the mean square radii of the gyration of branched and linear molecules of the same molecular weight,

$$\langle s \rangle_b{}^2 / \langle s \rangle_l{}^2$$

In practice the value of g is derived from the ratio of the solution viscosity of branched and linear molecules of the same molecular weight; and the relation suggested by Zimm and Kilb[6] has been used in the present studies:

$$g^{1/2} = [\eta]_b / [\eta]_l$$

The values of λ for fractions and whole polymers have been derived by using the above relations for monodisperse and polydisperse polymers, respectively.

Short-Chain Branching.   The method employed in determining the methyl group content of a polyethylene sample is essentially similar to that given in ASTM D2238-64T, Method B.   Films of the fractionated samples of polyethylene, 0.01 in. thick, were scanned in an infrared spectrometer between 7.00 and 7.60 μ.   From the ratio of the absorption bands at 7.25 μ (due to methyl groups) and 7.30 μ (due to methylene groups) the number of methyls per 1000 carbon atoms was calculated by using a previously established calibration curve.

Materials Included in Study

Each of the parent polymers included in this study is a commercial low-density resin manufactured by a high-pressure process.   The end-uses of the resins vary but their melt index and density values fall within a fairly narrow range.   A list of these resins is given in Table I along with an approximate ranking of the level of long-chain branching expected on the basis of their synthesis conditions.

TABLE I
Whole-Polymer Data

Polymer sample	Melt index, g/10 min	Annealed density, g/ml	Degree of LCB[a]
I	2.82	0.9199[b]	High
II	1.88	0.9217[b]	Moderate
III	1.38	0.9257[b]	Low
A	1.29	0.9252	Very low
B	2.7	0.9224	High
C	1.78	0.9213	Moderate
D	1.20	0.9193	Very high
E	1.85	0.9233	Low
F	2.0	0.9209	Low

[a] Inferred from synthesis conditions.
[b] Measured on quenched samples.

RESULTS AND DISCUSSION

As indicated above, the derivation of realistic molecular weight values from GPC analysis of fractions from a parent resin forms the basis of a comprehensive structure analysis of branched polyethylene. Efforts have therefore been made to demonstrate the effectiveness of the application of the universal calibration in conjunction with the iterative analysis as outlined in the Experimental Section, in evaluating molecular weights. To this end, three resins, I, II, and III which exhibit differing branching characteristics, have been subjected to a fairly complete structural evaluation consisting of molecular weight determination on fractions and whole polymer through GPC, measurement of low-shear melt viscosity, and methyl content, and estimation of the degree of long-chain branching. Molecular weights, both number-average and weight-average, have been measured for an appreciable number of fractions from the three resins. The resulting data are given in Table II.

Agreement between the measured and computed molecular weights is very good over the whole molecular weight range. One may conclude from these data both that the universal-calibration concept of Benoit effectively takes into account the influence of long-chain branching and that the iterative analysis, described above, adequately handles the problems associated with the application of the universal calibration to fractions exhibiting appreciable polydispersity. The ability to measure molecular weights of branched polyethylene fractions in this manner is of tremendous practical importance because of the increased reliability, speed and simplicity of the GPC technique as compared to the classical molecular weight measuring techniques of osmometry and light scattering.

The value of rapid and effective molecular weight measurement is particularly appreciated in the case of branched polyethylene because it is only through a knowledge of molecular weight that the degree of long-chain branching may be readily estimated. Normally, a comparison of the

TABLE II. Computed and Measured Molecular Weights of Branched Polyethylene Fractions

Resin and fraction	Weight %	Solution viscosity $[\eta]$ (140°C), TCB	Melt viscosity η^0 (190°C), poise	Methyl content CH₃/1000C	$\bar{M}_n \times 10^{-4}$ Computed	$\bar{M}_n \times 10^{-4}$ Measured	$\bar{M}_w \times 10^{-4}$ Computed	$\bar{M}_w \times 10^{-4}$ Measured	$R = \bar{M}_w/\bar{M}_n$ (computed)	$\lambda \times 10^4$
Resin 1										
4	7.4	0.35	—	30.0	1.26	1.20	1.47	1.37ª	1.17	1.0
5	7.1	0.39	8.82 × 10	28.2	1.85	1.72	2.13	1.94ª	1.15	3.3
8	6.1	0.61	1.97 × 10³	26.9	3.69	3.87	4.41	4.41ª	1.20	2.8
10	7.0	0.70	1.97 × 10⁴	25.3	7.49	7.06	9.58	7.35ª	1.28	9.8
12	4.2	0.89	2.37 × 10⁵	26.2	10.6	11.2	14.8	12.2	1.40	9.0
14	4.2	1.15	2.05 × 10⁶	24.7	16.8	16.5	28.9	33.3	1.72	12.1
15	9.3	1.56	1.02 × 10⁷	25.2	23.7	39.8	83.2	86.9	3.51	27.6
16	8.6	1.56	7.1 × 10⁷	25.7	40.8	66.4	123.0	137.0	3.08	60.2
Whole polymer		0.86	3.78 × 10⁴	—	2.44	2.81	38.2	54.7	15.7	6.54
Resin II										
4	7.3	0.36	5.5 × 10	31.2	1.06	1.07	1.34	1.21ª	1.26	—
5	7.8	0.37		30.1	2.01	1.51	2.33	1.71ª	1.16	6.4
8	6.0	0.61	2.38 × 10³	27.5	3.85	4.02	4.99	4.58ª	1.30	4.9
10	7.2	0.85	7.01 × 10⁴	24.0	6.92	7.54	9.80	8.83	1.42	4.9
12	7.3	1.16	1.84 × 10⁶	22.9	14.5	14.1	23.1	19.2	1.59	7.3
14	4.1	1.66	4.81 × 10⁷	21.5	26.7	25.0	58.5	64.7	2.19	11.3
Whole polymer		0.86	6.35 × 10⁴	—	1.99	2.34	25.9	23.3	13.0	4.63
Resin III										
2	9.6	0.31	—	29.5	1.50	1.30	1.69	1.48ª	1.13	5.6
3	11.5	0.38	7.5 × 10	27.8	1.90	1.63	2.16	1.86ª	1.14	3.8
4	8.7	0.56	1.1 × 10³	23.3	3.11	3.29	3.65	3.82ª	1.17	2.3
5	17.7	0.78	6.0 × 10⁴	19.8	5.95	6.25	7.58	7.50ª	1.27	4.2
6	10.7	1.01	1.6 × 10⁶	17.8	8.58	9.31	11.4	11.4ª	1.33	3.1
7	9.5	1.15	7.4 × 10⁶	16.5	10.6	10.5	14.3	12.9ª	1.35	2.9
8	8.4	1.33	8.2 × 10⁷	16.0	13.5	15.4	19.3	19.3ª	1.43	2.8
9	8.4	1.48	4.6 × 10⁸	15.5	16.6	18.1	27.7	24.7ª	1.67	3.8
11	3.5	1.92	—	14.3	29.6	25.7	44.3	31.1ª	1.50	3.3
Whole polymer		0.79	7.88 × 10⁴	—	2.66	2.46	8.93	7.75	3.4	1.48

ª $\bar{M}_w = R_{GPC}\bar{M}_n$ (osm), where $R_{GPC} = A_w/A_n$.
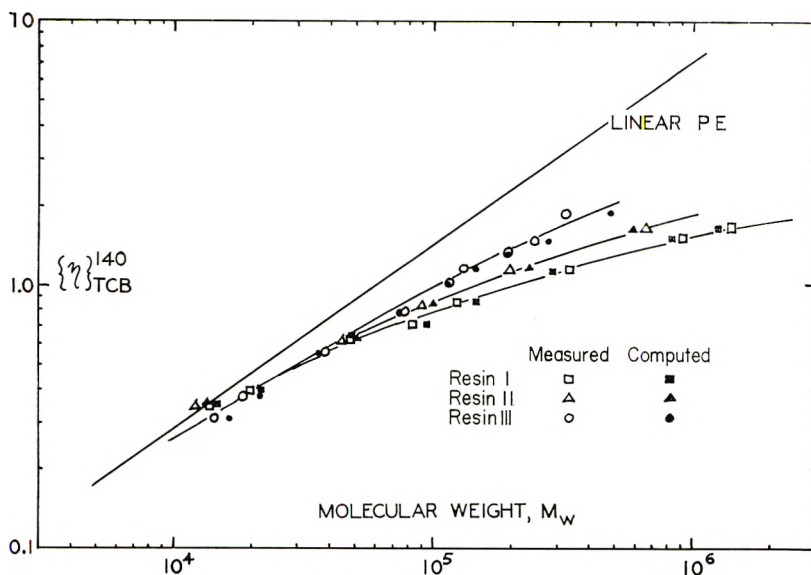
Fig. 2. Comparison of solution viscosity vs. molecular weight relations derived using computed and measured molecular weight data.

solution viscosity of a branched polymer with that of a hypothetical linear polymer of the same molecular weight formed the basis for a long-chain branching (LCB) index. A graphical representation of the molecular weight dependence of solution viscosity for the branched resins as compared to the relation for linear polymer effectively illustrates the relative degree of LCB in a particular resin. Figure 2 shows the data for the resins, I, II, and III obtained by using both computed and measured molecular weight values and indicates that the degree of LCB among these resins follows the order: I > II > III.

The agreement between measured and computed data is observed to be sufficient to allow one to distinguish clearly between the differing LCB levels in the three resins. The molecular weight distributions are seen to differ appreciably for these resins, clearly reflecting the presence of differing degrees of LCB (see Table II). An increase in the overall level of LCB is accompanied by an increase in the weight-average molecular weight and a broadening of the molecular weight distribution (MWD).

The evaluation of the degree of LCB of fractions through the long-chain branching index λ provides a more detailed description and some indication of the distribution of LCB within each resin. It is interesting to note, for example, that the least branched resin III exhibits a very narrow distribution of LCB in which all molecular species appear to exhibit the same level of LCB. In contrast, the more highly branched resin I shows a relatively broad LCB distribution with the higher molecular weight species exhibiting a much higher degree of LCB than those of low molecular weight. Clearly, the relation between degree of LCB and molecular weight is not simple,

though it is believed to be a reasonable reflection of the complex poly-
merization conditions.   In passing it is noted that this molecular weight
dependence of λ is the cause of some uncertainty in the application of the
method of Drott and Mendelson[7] for deriving MWD data from the GPC
analysis of branched polyethylene whole polymers.   They assume con-
stancy of λ for all molecular species within a given resin in deriving a com-
puted solution viscosity-molecular weight relation.

In the calculation of λ, all fractions were assumed to be monodisperse,
and the suitable Zimm branching function was used.   The polydisperse
relation was used for whole polymers.   From the data in Table II, one
notes that the values of λ for fractions and whole polymers are not com-
pletely consistent.   The parent resin in each case gives a lower λ than would
be expected from the summation of the λ values for their fractions.   It was
considered possible that the polydisperse Zimm function might also be
applicable to fractions in view of the fact that they are by no means com-
pletely monodisperse.   However, the considerably lower values that result,
even for very sharp fractions, appear to be in even poorer agreement with
the λ values of the parent resin.   It is probably true that the extremely high
values obtained for the high molecular weight fractions from resin I are
overestimates due to the use of the monodisperse function despite the quite
broad MWD.   At present it is not clear which is the proper approach to the
calculation of realistic branching indices.   However, it is believed that the
essential character of the molecular weight dependence of LCB for each
resin will remain.

From a practical standpoint, one of the main reasons for putting emphasis
on LCB in high-pressure polyethylenes is the very strong dependence of the
melt-flow properties on this structural feature.   This dependence of melt
viscosity of branched polyethylenes on the degree of LCB has been noted
previously[8] and is illustrated by the molecular weight dependences of low-
shear melt viscosity for resins I, II, and III shown in Figure 3, where they
are compared with the relation for linear polyethylene.   It is particularly
interesting to note that the melt viscosity of a branched fraction may be
higher or lower than that observed in the absence of LCB.   This possibility
of LCB causing enhancement of melt viscosity is indicative of the presence
of strong intermolecular interactions and has been observed in other
systems.[9,10]   It is significant to note that this enhancement of melt vis-
cosity, which is not predicted by the theories of Bueche,[11] carries through
the whole polymer.   There is only slight diminution of the effect of the
higher molecular weight species on dilution by smaller molecules in the
whole polymer, although it has been suggested that enhancement is unlikely
except when a high concentration of molecules possessing long-chain
branches of very similar (and high) molecular weights is present.[12]

Studies aimed at elucidating the structure of branched polyethylenes
have rightly been concerned with the nature and influence of LCB.   How-
ever, it is believed that this preoccupation has led to a neglect of the
influence of short-chain branching (SCB).   Certainly, there have been
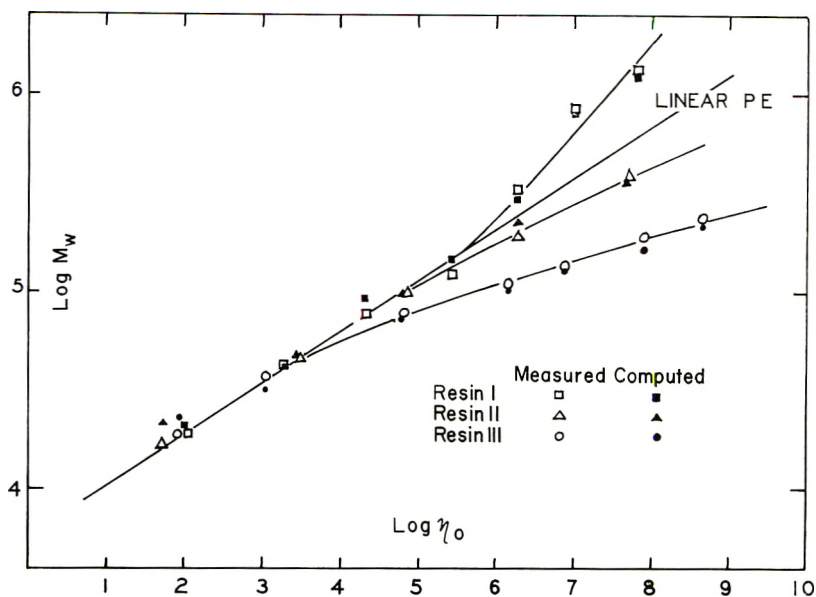
Fig. 3. Comparison of melt viscosity vs. molecular weight relations derived using computed and measured molecular weight data.

studies aimed at determining the type of SCB present in the molecules,[13,14] but in reality it must be the distribution of SCB among the molecular species which exerts the major influence on resin properties. The crystallization, melting and cold-drawing characteristics of a resin are all likely to be influenced by the distribution of SCB.

The present scheme for structural analysis allows one to evaluate the distribution of SCB through analysis of gradient-elution fractions of differing molecular weights. From the limited data presented in Table II it can be seen that the distribution of SCB does differ among commercial resins. For example, resin I exhibits a very narrow SCB distribution, in contrast with the broad distribution observed for resin III. It is interesting to note that distributions of long-chain and short-chain branching present in these three resins appear to be independent to a great extent. This is indicative of the wide variety of branched structures that are possible in polyethylenes.

Finally, as a further illustration of the kind of information one may obtain by using the above approach to polyethylene structure, there is presented in Figures 4 and 5 the molecular weight dependence of both solution viscosity and melt viscosity derived for a series of commercial resin types (see Table I). As these data indicate, there is a wide range in the degree of LCB to be found in commercial resins. It appears from Figure 5 that the melt viscosity is very sensitive to the level (and possibly type) of LCB present in the higher molecular weight species and that enhancement of low-shear melt viscosity is the norm, rather than the exception, in commercial branched polyethylenes.
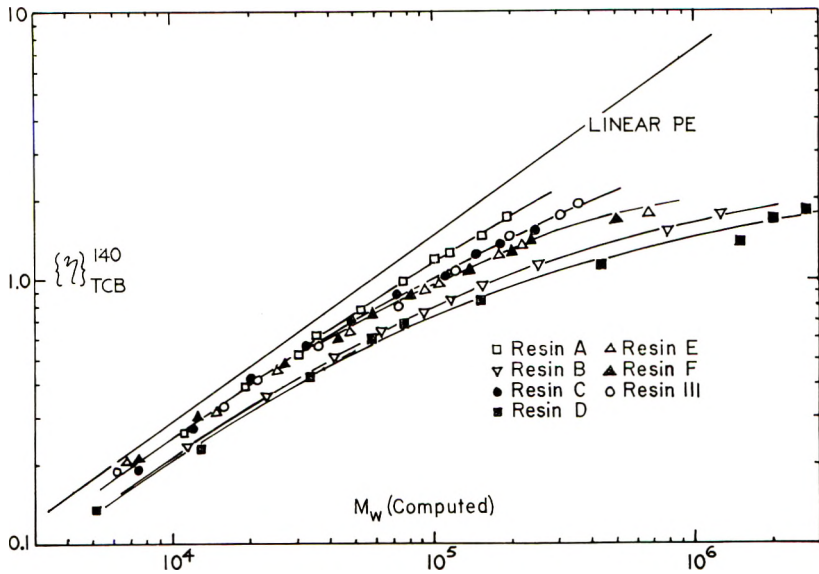
Fig. 4. Solution viscosity vs. molecular weight for a series of commercial branched poly-ethylenes.
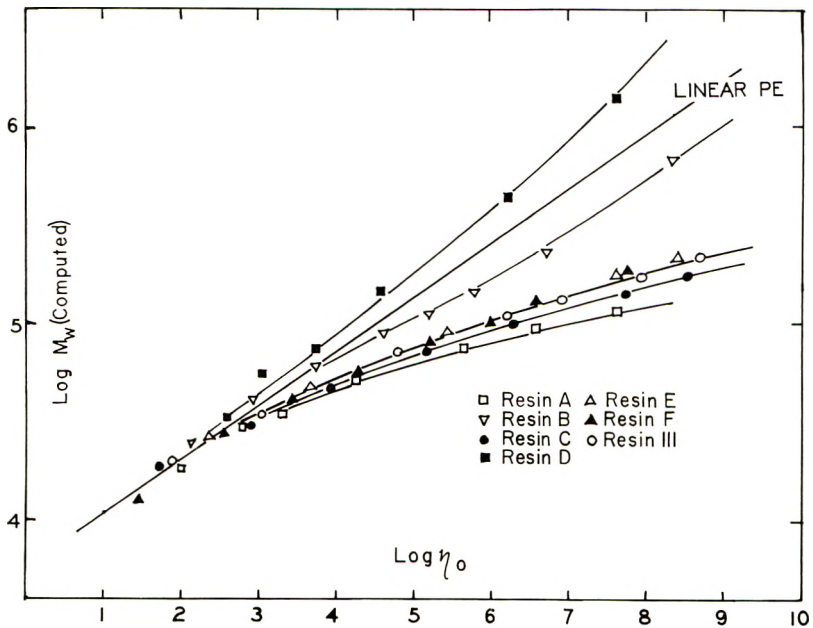
Fig. 5. Melt viscosity vs. molecular weight for a series of commercial branched poly-ethylenes.

The complexity of the branching structure (both long-chain and short-chain) in low-density polyethylenes and the considerable influence it must exert on polymer properties are quite clear from the foregoing data. It would seem that a fairly complete knowledge of the total structure for an appreciable number of resin types is necessary if one hopes to establish a working relation between synthesis conditions, resin structure and resin properties. It is believed that the combined use of a preparative gradient-elution fractionation technique in conjunction with molecular weight evaluation through GPC as described above represents a significant step toward this goal.

APPENDIX

The NBS Standard #1475 shows considerable promise as a GPC calibration standard and has been used in the present studies according to the following procedure.

The molecular weight distribution data provided with the NBS standard is in the form: molecular weight versus cumulative weight per cent (I_x). To derive a GPC calibration, the NBS #1475 was first run on the GPC and the GPC trace divided into one-fifth count peak heights. By using the Schulz method of integration, the cumulative peak height per cent (I_x') was calculated as a function of elution volume (count number C). If the separation is an effective molecular weight separation, I_x is equal to I_x'. Thus by directly matching the I_x versus M data supplied by NBS with the I_x' versus C data (obtained from the experimental GPC trace for the NBS standard linear polyethylene) one derives a set of values of elution volume versus molecular weight values. These C and M values were subjected to a polynomial regression analysis on the computer until a satisfactory relation between the two quantities was obtained giving a 99.8% confidence limit. For the GPC column system used in the present study, a quadratic relation, $\log M = B_0 + B_1 C + B_2 C^2$, was found to be appropriate. The three constants of this algebraic equation adequately define the calibration curve over the range of molecular weights presented in this paper. By this particular procedure, four calibration curves were obtained from four GPC traces and gave very good agreement. The final calibration used was the average from the four sets of data.

Two aspects of the use of NBS Standard #1475 deserve comment. First, the standard has a somewhat narrow molecular weight distribution, and it proves necessary to extrapolate the derived calibration curve to cover the very high molecular weight region. For this reason an approximately linear calibration curve is to be preferred to remove some ambiguity in the extrapolation process. Secondly, the derivation of the calibration curve through the cumulative height per cent may lead to appreciable errors where any uncertainty exists in defining the beginning and end of the GPC trace. A stable baseline is thus an important requirement.

The appropriate choice of GPC column system, with precautions made to minimize baseline fluctuations, through temperature control of the photocell block, allows one to derive a very effective GPC calibration by using the NBS #1475. Thus the GPC analysis of a series of linear polyethylene fractions covering a wide range of molecular weights (10^3 to 10^6) yields a well defined Mark-Houwink relation for TCB at 140°C.

$$[\eta] = 3.23 \times 10^{-4}\bar{M}_w^{0.735}$$

References

1. Z. Grubisic, P. Rempp, and H. Benoit, *J. Polym. Sci. B*, **5**, 733 (1967).

2. P. M. Kamath and L. Wild, paper presented at 22nd Annual Technical Conference of the Society of Plastics Engineers, Montreal, Canada, March 7-10, 1966; *SPE Tech. Papers*, **12**, XVII-6 (1966).

3. R. M. McGlammery and A. A. Harban, *Materials Res. Standards (ASTM)*, **3**, 1033 (1963).

4. L. Wild and R. Guliana, *J. Polym. Sci. A-2*, **5**, 1087 (1967).

5. B. H. Zimm and W. H. Stockmayer, *J. Chem. Phys.*, **17**, 1301 (1949).

6. B. H. Zimm and R. W. Kilb, *J. Polym. Sci.*, **37**, 19 (1959).

7. E. E. Drott and R. A. Mendelson, *J. Polym. Sci. A-2*, **8**, 1361 (1970).

8. R. A. Mendelson et al., *J. Polym. Sci. A-2*, **8**, 105 (1970).

9. V. C. Long, G. C. Berry, and L. M. Hobbs, *Polymer*, **5**, 517 (1964).

10. G. Kraus and J. T. Gruver, *J. Polym. Sci. A*, **3**, 105 (1965).

11. F. J. Bueche, *J. Chem. Phys.*, **40**, 484 (1964).

12. W. Graessley and J. S. Prentice, *J. Polym. Sci. A-2*, **6**, 1887 (1968).

13. A. H. Wilbourn, *J. Polym. Sci.*, **34**, 569 (1959).

14. A. Barlow and P. M. Kamath, *J. Polym. Sci. A-1*, **5**, 2023 (1967).

Apparatus for Instantaneously Measuring Ultraviolet, Visible, or Infrared Dichroism from Thin Polymer During High-Speed Stretching

GARTH L. WILKES,* Y. UEMURA,† and RICHARD S. STEIN,‡ *Polymer Research Institute and Department of Chemistry, University of Massachusetts, Amherst, Massachusetts 01002*

Synopsis

An apparatus has been constructed for following changes in the dichroism of a polymer film undergoing rapid elongation. By means of a rapidly rotating mirror with evenly spaced open sectors, a beam of radiation is passed through the sample and then alternately polarized in the horizontal and vertical direction so that the horizontal and vertical absorbances may be rapidly compared in time as compared with the time of sample elongation (a few milliseconds). The apparatus utilizes reflection optics and a grating monochromator so that measurements may be made by using ultraviolet, visible, or infrared radiation. The transmitted intensity is detected by a photomultiplier or semiconductor infrared device, the output of which is amplified and displayed on an oscilloscope. A temperature-controlled sample chamber is provided. The operation of the apparatus is illustrated by following the change in dichroism of a sample of dehydrohalogenated poly(vinyl chloride) with visible radiation during rapid extension.

Introduction

Information regarding the time dependence and magnitude of molecular response in a rapidly deformed polymer film is important with respect to such properties as impact strength or brittleness. Also, such information leads to a better understanding of how a polymeric solid responds on a molecular scale to an imposed stress. Since polymeric solids are in general complex systems with respect to structure on a submicroscopic scale, information on molecular response is of critical value when correlating bulk behavior with molecular structure.

Interest in measuring molecular orientation and its time dependence is certainly not new, since many dynamic techniques involving low-amplitude vibrational strain are already well established to determine orientation or some bulk property, such as stress, which depends on molecular response and its relaxation. Examples of such dynamic techniques are the use of the

---

* Present address: Department of Chemical Engineering, Princeton University, Princeton, N. J. 08540.

† On leave from Sumitomo Chemical Co., Japan.

‡ To whom correspondence should be sent.

torsion pendulum, and the methods of dynamic birefringence, light scattering, and x-ray diffraction.

A second category of experiment exists for measuring similar response during a single extension and can be called the "one-shot" experiment. This type of experiment is generally irreversible. The irreversibility generally arises from the fact that large sample deformations are involved and thus the range of linear viscoelasticity is exceeded. This molecular response in nonlinear regions is of interest. The method need not rely on the assumption on which dynamic techniques are based, i.e., that past cyclic deformations have not changed the internal structure of the sample.

It would be desirable to measure the instantaneous orientation of a particular phase or component in the system of interest (e.g., crystalline vs. amorphous orientation or one component of a copolymer system during rapid deformation). The dichroism method permits such investigations. This technique has been used extensively in measuring "component" orientation after a sample has been deformed or over long periods (minutes) of relaxation.[1-5] Most reported dichroic studies, however, suffer in that the short-time dependence of orientation cannot be determined. Behavior in this region can lead to information about the rate of energy dissipation, which relates to such bulk properties as impact strength. We have now developed an apparatus which can measure dichroism during the rapid deformation of a sample at a controlled temperature. Our instrument is suitable for making measurements in the ultraviolet, visible, and infrared regions of the spectrum. Strain rates of the order of 2000/in./in./min can be applied.

Dichroism and Orientation

To describe the orientation of a polymer molecule in a solid, the Hermans orientation function f, is generally used:[6,7]

$$f \equiv 3 \langle \cos^2 \theta \rangle - 1)/2 \tag{1}$$

where θ is the angle which the principal axis of the chain makes with the stretching axis or any other specified reference axis. It is clear that this function can vary from $-1/2$ to 1 as θ varies from 90° to 0°. The dichroism D, the experimental parameter, is defined as A_1/A_2, where A_1 and A_2 are the absorbances for radiation polarized parallel and perpendicular to the stretching direction, respectively. It is related to the orientation function, the desired parameter, by the expression[8,9]

$$f = C(D - 1)/(D + 2) \tag{2}$$

where

$$C = \frac{a_1 + 2a_2}{a_1 - a_2} \left(\frac{2}{3 \langle \cos^2 \alpha \rangle - 1} \right) \tag{3}$$

Here, a_1 and a_2 are the absorption coefficients associated with the principal and minor axis of the absorption ellipsoid, respectively. The angle α is that

between the principle axis of the absorption ellipsoid and the chain axis. As an example, in a chain which contains conjugated double bonds, α is $0°$ for the absorption associated with the diene structure. It is apparent that C may be different for different absorption bands.

Design Considerations

The instrument was so designed that a thin polymer film sample could be stretched simultaneously from each end by the firing of synchronized retractable hydraulic pistons clamped to the sample.* During this rapid deformation in a temperature controlled chamber, the dichroism is instantaneously measured by passing radiation through the sample and rapidly alternating the polarization direction from parallel to perpendicular to the sample stretching axis. The radiation is then passed through a monochromater and to a detector system, the output of which is recorded on a oscilloscope. The ratio of two consecutive absorbances is then determined from an oscilloscope trace and gives the dichroism at any time during the deformation or during relaxation.

Figure 1 shows a line drawing of the instrument. The numbers denoting the various components of the apparatus will be used in the following description of its operation. The mechanical (stretching) system is independent of the optical (spectrophotometer) system so as to minimize any transfer of vibrations to the optical system caused by the firing of the hydraulic pistons which stretch the sample. This has been accomplished by mounting each system on a separate base (lathe bed). The mechanical portion of the system has been described elsewhere;[11] hence its operation will not be described in detail here.
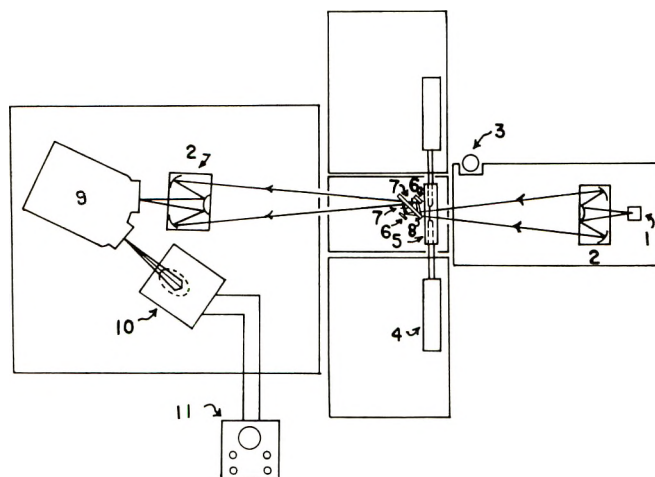
Fig. 1. High-speed dichroism instrument.

* A preliminary presentation of the design of this apparatus has been given.[10]

The optical part of the system is mounted on a lathe bed, oriented perpendicular to that for the mechanical system. As shown in Figure 1, the source (of ultraviolet, visible, or infrared radiation) is located at (1). The ultraviolet source is a Hanovia 901-131 type 200 W xenon mercury arc lamp with an Orion C-60-50 universal lamp housing. An Orion Model C-72-20 Universal lamp power supply was used as the DC lamp power source. The infrared source is a Warner and Swasey Model 10 Glowbar. The radiation from either source is collected by a Cassegrainian optical transfer system (Warner and Swasey Model 30) (2). This system then focuses the radiation through the window of the temperature-controlled sample chamber (5), where the sample is clamped between the ends of the two hydraulic pistons (4). Since the samples are stretched at the same rate from both ends, the central portion on which optical measurements are made remains fixed in position. The radiation transmitted by the sample passes from the chamber and enters the "chopper" region, explained in detail later, where the beam is rapidly switched from one path to another for the purpose of alternately passing the beam through one of two polarizers (7). For ultraviolet these are dichroic filters (Polacoat Model 105), while for infrared, wire grid polarizers (Perkin-Elmer) are used. The polarized radiation then passes to a second Cassegrainian optical transfer system (2), identical to the first one, where it is collected and focused on the slit of a grating monochromator (9) (McPherson Model 218) which has a numerical aperture $f/5.3$, comparable to the $f/5.5$ numerical aperture of the transfer system. During measurements the monochromator is set at a fixed wavelength. Upon exit from the monochromater, the beam impinges either upon a photomultiplier (RCA Type 7200) if measurements are being made in the ultraviolet region, or, in the case of infrared measurements, upon a 90° off-axis ellipsoid mirror (Perkin-Elmer) with focal lengths of 252 mm and 42 mm. The exit slit is located at the longer focal point, while the other focal point is located on a cryogenically cooled copper-doped germaniun semiconductor detector. (Santa Barbara Research Center, Model 9145-2) for infrared measurements. This detector is useful in the wavelength range 3–8.7 μ when operated at liquid helium temperature (4°K), A more easily operated gold-doped germanium detector (Barnes Engineering Co. Model A200) useful in the range 1.2–7 μ is an alternative which may be operated at liquid nitrogen temperature with somewhat lower sensitivity. The output of either detector can then be displayed, after suitable amplification, on a storage oscilloscope from which a photograph can be taken and the dichroic values determined.

The alternation of polarization is accomplished in the following manner. In the chopper region (refer to Fig. 1 and its detail in Fig. 2) are a chopper-rotating mirror (8), two small fixed-plane mirrors (6), and two fixed ultraviolet (or infrared) polarizers (7). It was necessary to alternate the polarization direction in times which are short compared to the time for stretching (a few milliseconds) so as to obtain the change in dichroism during rapid elongation. This was accomplished by using a rotating disk, where both
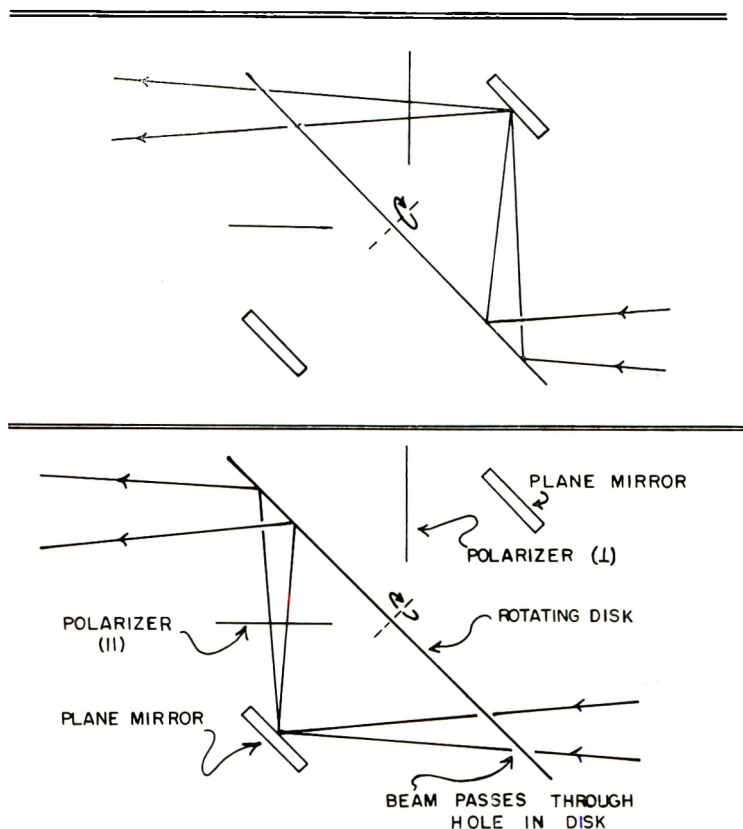
Fig. 2. Operation of chopper blade for switching polarization directions from parallel to perpendicular.

sides act as mirrors, and which has twelve evenly spaced, sector-shaped holes. The alternative scheme of rotating the polarizer was considered but it did not appear practical to rotate it at the required rate. The chopper mirror drive is made from a Princeton Applied Research Mechanical Model BZ-1 chopper furnished with a disk of our design. The chopping disk was made of 0.125 in. aluminum sheet having both surfaces polished to a flatness of 0.0001 in. The disk surfaces were then electroplated with Kanigan (NiP$_3$) by the Cambridge Plating Co. (Cambridge, Mass.). Kanigan coating is used on such optical surfaces before the final deposition of aluminum because of its excellent surface uniformity when polished. After the Kanigan coating and final polishing, aluminum was deposited on both sides, and then a final protective coating of magnesium fluoride was applied. A photograph of the chopper is shown in Figure 3. The operation of the chopping disk is illustrated in Figure 2, in which it is seen that the beam, making its exit from the sample chamber, can take one of two paths before being collected by the second transfer system. One such path is shown in the lower part of the figure. Here the rotating disk (1500 rpm) is at such a

point that the beam falls on an open sector of the disk and thus passes through and impinges on one of the small plane mirrors.   It is then reflected through a polarizer and strikes one surface of the chopper disk which reflects the beam to the second transfer system.   The alternate path of the beam is used when the disk rotates through 51° of arc (see upper part of Fig. 2).   Now the beam from the sample chamber strikes the surface of the disk which reflects it to the second plane mirror, which in turn reflects it
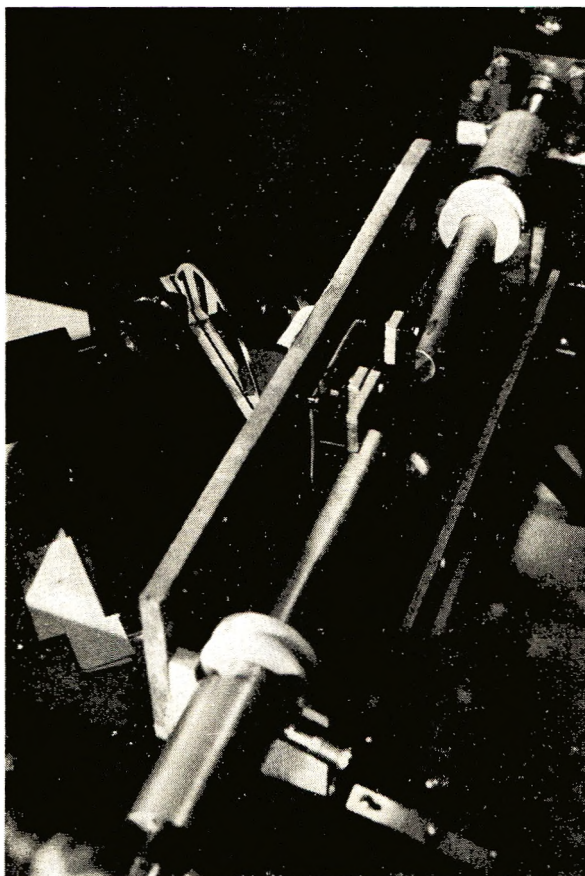
Fig. 3. Photograph of the chopper region of the high-speed instrument.

through the other polarizer.   The polarization direction of the radiation passed by this polarizer is oriented at 90° to that of the former.   The beam then falls on an open-sector region of the disk and thus passes through, taking a path to the second transfer system identical with the first path. Thus the detector will respond to signals which alternate repeatedly between radiation which is polarized parallel and perpendicularly to the stretching axis.   Since there are 600 signals/sec, the response time of the detector must be quite short.   Both the photomultiplier and cryogenically

cooled semiconductor have a response time on the order of a nanosecond which is sufficient.

Calibration

Calibration of the instrument was necessary in order to obtain accurate quantitative results and reproducibility. The factors necessary for consideration when making measurements in the visible region are: (a) reflectivity variation of the chopper wheel, (b) frequency dependence of photomultiplier, (c) oscilloscope calibration, (d) polarization dependence of photomultiplier, (e) machine polarization, (f) linearity of photomultiplier response, and (g) beam convergence. We briefly consider some of these factors.

Since the surface of the rotating disk is not perfectly uniform in reflectivity, as can be noted by Figure 4, one must first measure a "baseline" trace so that the absorption of a sample can be calculated relative to the baseline corresponding to the particular sector on the disk which is in position when the measurement is made. Thus a reference point on the disk is necessary. This point is established by blocking one sector of a small rotating wheel provided as part of the chopper drive which synchronously chops a beam of light. This light is detected by a small photocell within the chopper motor housing which provides the reference signal which can be noted in Figure 4.

Frequency dependence of the photomultiplier was not a limiting factor, as mentioned earlier, since the response was of the order of 10^{-9} sec as discussed by Sommer[12] and signal generation was of the orfer of 600 cps.

Photomultipliers are known to show a small dependence on polarization of the incident signal which strikes the cathode. Generally, this difference in signal output with polarization is of the order of 2 or 3%. To eliminate this effect we placed a thin piece of ground glass in front of the cathode window which acts as a depolarizer and eliminates the polarization dependency.

Machine polarization however cannot be easily eliminated in our instrument in the usual fashion by placing the sample axis and electric vector of the polarizers at 45° to the slits because of the optical and spatial restrictions in our system.

It is necessary to determine a correction factor for this effect. If intensities of the parallel and perpendicularly polarized beams are appreciably different, it is necessary to balance them by using neutral filters or slits to keep both signals on scale.

To maintain linearity in the photomultiplier output, commercial spectrophotometers generally make use of variable slit widths which adjust automatically to maintain this linearity. In our instrument this was not practical owing to the short time of the experiment. As a result, a calibration curve was obtained at each wavelength used for our instrument by calibrating against absorbance values measured with a Cary model 14 spectrophotometer. Polymer films were measured on both instruments and the absorbance found for each for a particular polarizer orientation by

NO SAMPLE

(a)

DH– PVC
IO MIN.
20 msec/div

(b)
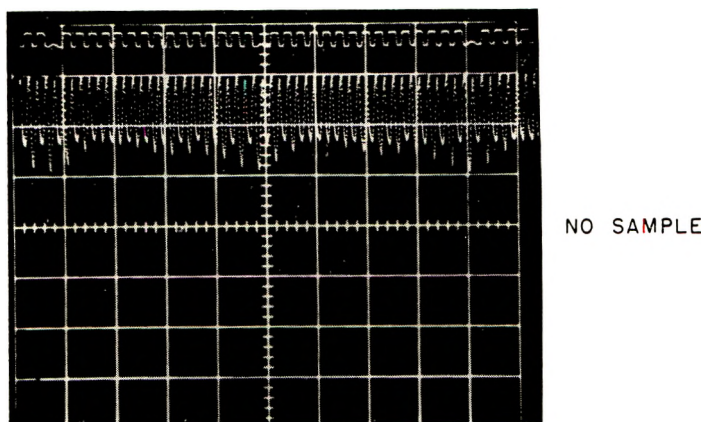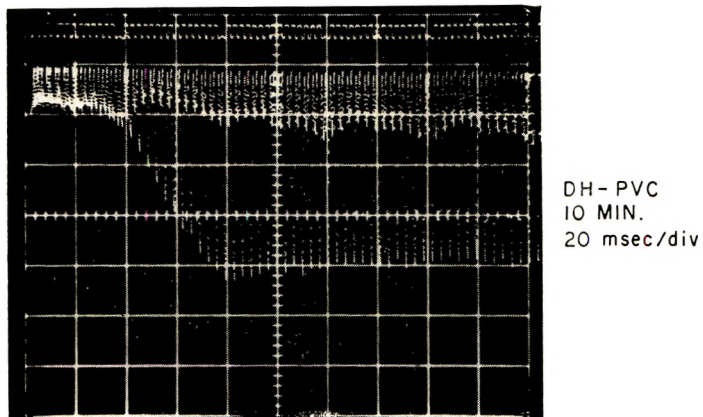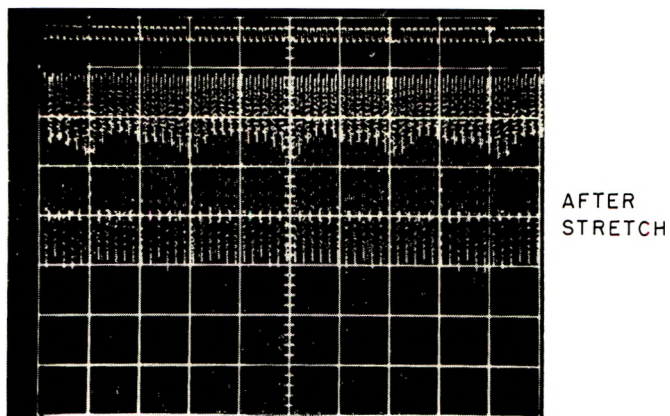
AFTER
STRETCH

(c)

Fig. 4. Oscilloscope traces of photomultiplier signals for (a) baseline, (b) stretching of sample (DHPVC), and (c) after stretch with sample still mounted.
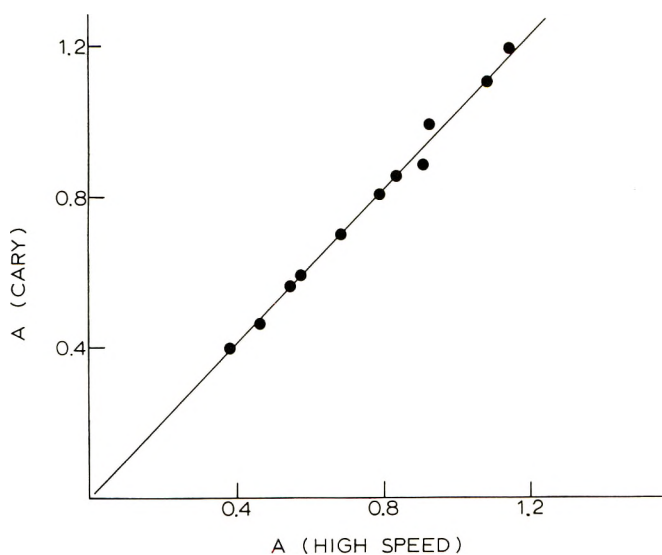
Fig. 5. Comparison of absorbence measured by Cary spectrometer with that measured on high-speed instrument.

the Cary instrument was plotted against that found by our instrument. This graph is shown in Figure 5. This shows the highly linear response of our instrument with absorbance. As was expected, no dependence was noted for polarization direction, since the polarization consideration had been carried out before this calibration. One notes that at high absorbance a small deviation is observed. We therefore tried to keep the absorbances of the film to be stretched in an appropriate range and applied a correction factor when this was not possible.

Errors in dichroism measurements resulting from beam convergence were found to be negligible according to the equation of Fraser[8] for uniaxial orientation. This shows that no correction is necessary for the perpendicular polarization but the parallel orientation is dependent upon convergence. The transmittance T_1 for parallel orientation of the polarizer is is given by

$$T_1 = e^{-\epsilon_\delta \tau} + \frac{2}{3}\left[e^{-\epsilon_p \tau} - e^{-\epsilon_\delta \tau}\left(\frac{\cos^2\theta_1 + \cos^2\theta_2 + \cos\theta_1\cos\theta_2}{\cos\theta_1 + \cos\theta_2}\right)\right] \quad (4)$$

where ϵ_p is the extinction coefficient of the sample with light polarized parallel to sample axis; ϵ_δ is the extinction coefficient of the sample with light polarized perpendicular to sample axis; τ is the thickness of the sample; θ_1 is the smaller semiangle of the cone of the converging beam; and θ_2 is the larger semiangle.
Fraser simplified this by making the substitution

$$m = 2(\cos^2\theta_1 + \cos^2\theta_2 + \cos\theta_1\cos\theta_2)/3(\cos\theta_1 + \cos\theta_2) \quad (5)$$
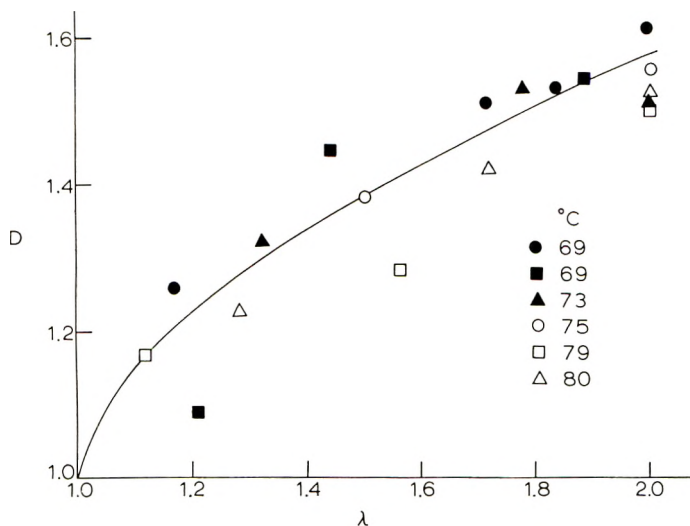
Fig. 6. Variation of dichroism with extension ratio for samples of DHPVC at several temperatures.

thus allowing one to write

$$T_1 = e^{-\epsilon\delta\tau} + m[e^{-\epsilon p\tau} - e^{-\epsilon\delta\tau}] \tag{6}$$

Since the transmittance, T_2, for perpendicular electric vector orientation can be written as

$$T_2 = e^{-\epsilon\delta\tau} \tag{7}$$

the dichroism, D, can be written as

$$D = \ln \{T_1 + [(1/m) - 1] (T_1 - T_2)\}/\ln T_2 \tag{8}$$

In our case θ_1 was ca. 2.0° and θ_2 ca. 5.5°. With eq. (5), this leads to a calculated value of m of about 1.0 so the effect of the converging beam on the final dichroism is negligible in our instrument.

To illustrate the actual use of the instrument some data are given from preliminary investigations of thin films of partly dehydrohalogenated poly(vinyl chloride) (DH-PVC). The dichroism and birefringence of this system has recently been extensively investigated by Shindo et al.[4] DH-PVC is prepared by reacting PVC with potassium hydroxide (KOH) in solution at low temperatures, resulting in the introduction of conjugated double bonds into the chain backbone. The average sequence length of these double bonds is dependent upon the reaction time. Since the conjugated sequences are strongly absorbing in the ultraviolet and visible regions of the spectrum, these systems are convenient for investigation by this new technique. Figures 4b–c illustrate the observed signals from the ultraviolet photomultiplier detector during stretching and after stretching of a 10-min reaction sample of DH-PVC. One can see there is a definite dichroic response by the sample as a result of deformation.
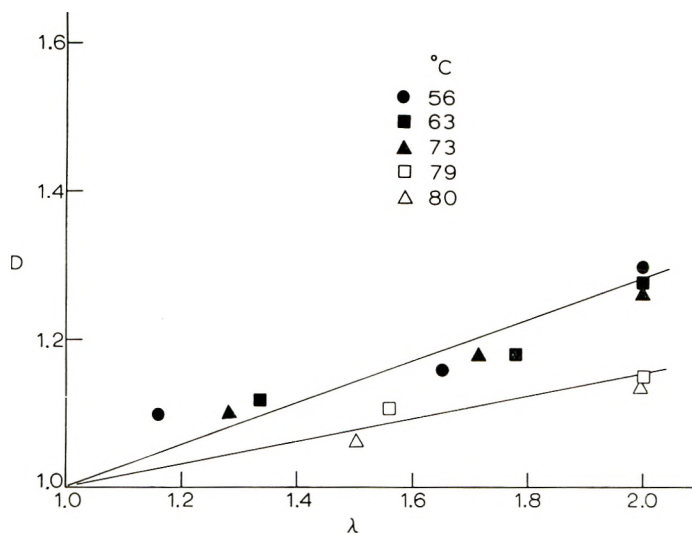
Fig. 7. Variation of dichroism with extension ratio for a sample of DHPVC plasticized with 35% diethyl phthalate (DEP) at several temperatures.
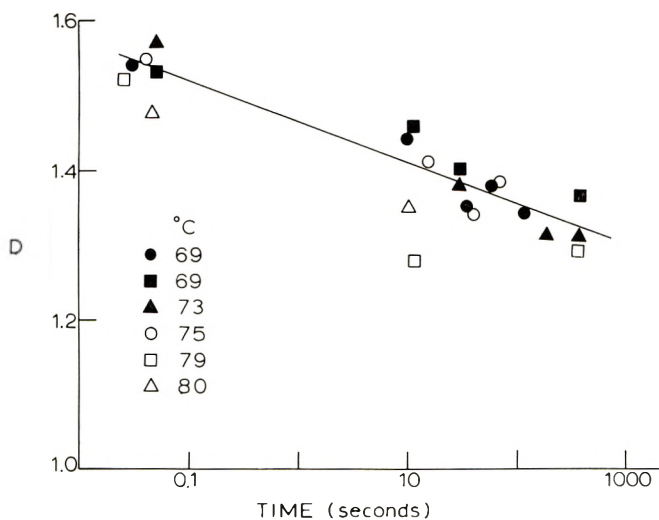
Fig. 8. Variation of dichroism with time during the relaxation of unplasticized DH-PVC at several temperatures.

Films of DH-PVC were prepared by a 10-minute KOH reaction time at 0°C. Figure 6 shows the dichroism of such films as a function of extension ratio at different temperatures. Such data are nonlinear with extension ratio, yet relatively independent of temperature over the range of about 65–80°C. Figure 7 shows similar data measured on the same DH-PVC material which had been plasticized with 35 wt-% diethyl phthalate (DEP) One sees in this more "rubberlike" film, that the dichroism behaves in a near linear manner over the same extension and temperature ranges.
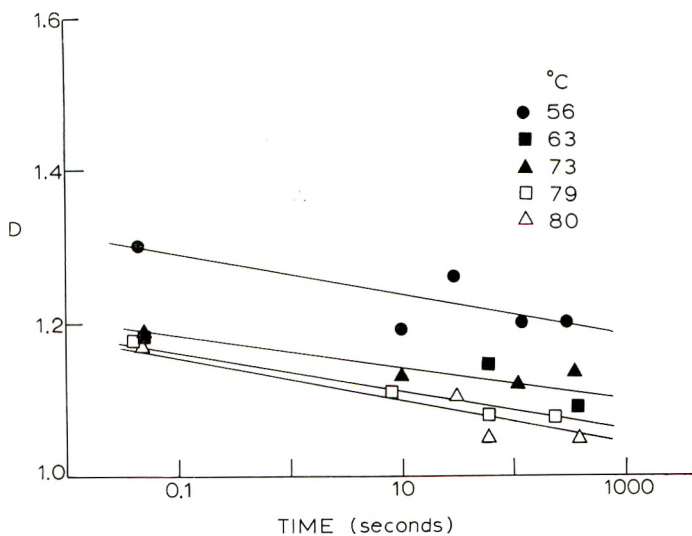
Fig. 9. Variation of dichroism with time during the relaxation of DH-PVC plasticized with 35% DEP at several temperatures.
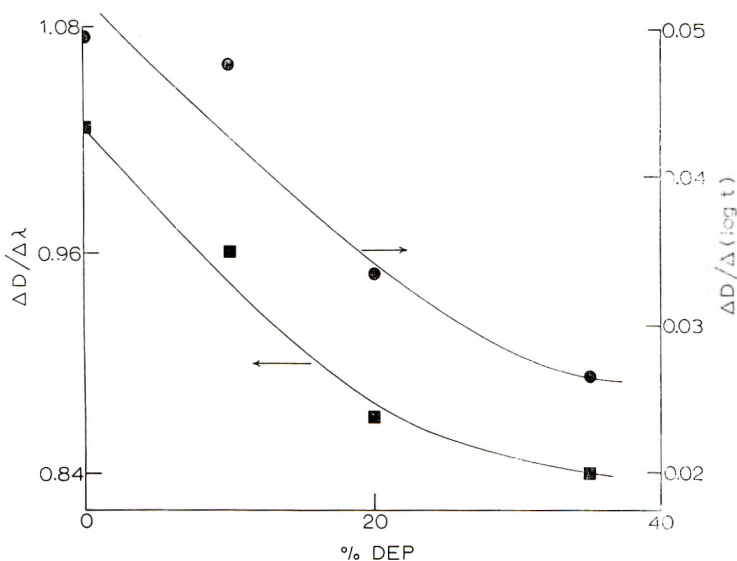
Fig 10. Variation of initial rate of change of dichroism with elongation ratio and with time as a function of DEP content.

There is a greater temperature dependence than for the unplasticized film. Also, the dichroism is less for the plasticized material than for the unplasticized films because of the greater loss of molecular orientation by relaxation. Figures 8 and 9 show the relaxation of the dichroism measured as a function of the logarithm of time following extension for these two types of films described above. Here both the unplasticized and plasticized

materials give linear behavior but with different time dependences (different slopes). Plots of the "average" slopes of dichroism-extension plots and dichroism-log time plots as a function of DEP content are shown in Figure 10.* Again, the plasticizer action can be interpreted in terms of its effect on the relaxation spectrum of the material. Longer times during the relaxation experiment were not used, since the DH-PVC material is chemically unstable over long times when exposed to temperatures over 50°C and to ultraviolet radiation. To minimize the effect of ultraviolet radiation during the relaxation experiments, the light source was blocked off between data point acquisition at longer times.

Infrared Studies

The application of this instrument to infrared relaxation studies is currently being carried out and will be reported in a future publication.[13]

References

1. R. Gotoh, T. Kakenska, and N. Hagama, *Kolloid-Z.*, **205**, 18 (1965).
2. S. Onogi, T. Asada, and T. Takegi, *J. Soc. Mat. Sci. Japan*, **16**, 746 (1967).
3. B. E. Read and R. S. Stein, *Macromolecules*, **1**, 116 (1968).
4. Y. Shindo, B. E. Read, and R. S. Stein, *Makromol. Chem.*, **118**, 272 (1968).
5. S. Onogi, T. Sato, T. Asada, and Y. Fukui, *J. Polym. Sci. A-2*, **8**, 1211 (1970).
6. P. H. Hermans and P. Platzek, *Kolloid-Z.*, **88**, 68 (1939).
7. L. E. Alexander, S. Oldberg, and G. R. Taylor, *J. Appl. Phys.*, **26**, 1068 (1955).
8. R. D. B. Fraser, *J. Chem. Phys.*, **21**, 1511 (1953).
9. R. Yamada and R. S. Stein, *J. Polym. Sci. B*, **2**, 1131 (1964).
10. G. L. Wilkes and R. S. Stein, paper presented at American Chemical Society Meeting, New York, September 1969; *Polym. Preprints*, **10**, 965 (1969).
11. P. F. Erhardt and R. S. Stein, *J. Polym. Sci. B*, **3**, 553 (1965).
12. A. Sommer, *Photoelectric Tubes*, Methuen, London, 1951.
13. Y. Uemura and R. S. Stein, in preparation.

* The "average" slope of the extension ratio plots was determined from the straight line drawn from D equal to unity to the average value of D at $\lambda = 2$. The "average" slope for the log time plots was determined from the average straight line placed through the data at a particular DEP content. Due to scatter in the data and, the small number of samples measured, such treatment gives rise to error but qualitative trends or comparisons could in this way, be obtained from these initial data. Slopes were insensitive to temperature so that these "average" slopes are averaged over the temperature range studied.

Small-Angle Light Scattering from Optically Anisotropic Spheres and Disks.   Theory and Experimental Verification*

ROBERT J. SAMUELS, *Hercules Incorporated, Research Center, Wilmington, Delaware 19899*

Synopsis

The small-angle light scattering (SALS) theory for optically anisotropic spheres and disks is examined in depth.   An error is found in the existing sphere equations.   The correct form of the equations is identified and then experimentally verified for dilute starch suspensions.   Increased concentrations and solid films of starch granules are used to identify the effect of concentration on the scattering envelope.   Spherulitic films of isotactic polypropylene, isotactic polystyrene, nylon 610, PET, and nylon 66 are then used to examine different aspects of the SALS theory.   Experimental observations are found to agree with the predictions of the correct SALS equations.   Disk theory is interrogated and correlated with predictions for spheres.   It is found that the predicted patterns from spheres and disks are very similar under identical optical conditions, in contradiction to earlier predictions.   A method is developed for identifying the optical sign of spherulites too small to be seen in the optical microscope.   This study constitutes a comprehensive examination of SALS theory and includes many other aspects of the phenomena.   A catalogue of theroetical V_V SALS patterns from spheres and disks is also included.

INTRODUCTION

A theory describing the observed small-angle light scattering (SALS) from optically anisotropic spheres was first derived in 1960.[1]   This theory described the scattering behavior under two experimental optical conditions, denoted H_V SALS and V_V SALS.   The first, H_V SALS, occurs when an analyzer and polarizer are crossed.   Here scattering is dependent only on the size and shape of the scattering particle.   The second V_V SALS, requires that the polarizer and analyzer be parallel.   Scattering is much more complicated under V_V SALS conditions, as it depends not only on the size and shape of the scattering particle but also on both the optical anisotropy of the scattering particle and the polarizability of the surroundings.

During the past decade studies have concentrated on the application, verification, and extension of the H_V SALS portion of the theory while

*Portions of this paper were presented at the Amherst Forum on Light Scattering by Solid Polymers at the University of Massachusetts, Amherst, Mass., July 1969.

2165

little interest has been paid to V_V SALS behavior. This is surprising, since it is the V_V SALS behavior which is sensitive to just those anisotropic optical parameters on which the foundation of SALS theory rests. Thus, the present situation is one in which a theory that has never been adequately verified is in general use. Of more disturbing character, a later rederivation of the theory exists[2] which claims identity with the original theory and yet, as is shown in this study, does not predict the identical SALS equations. Thus two theoretical equations are in general use that are assumed identical but are not.

The purpose of the present study is (a) to point out that a theoretical and practical problem exists, (b) to clear up the identity problem by experimentally verifying the correct form of the theoretical equations, (c) to extend the application of the present SALS theory, which was derived for a system of independent scatterers, to the prediction of scattering from condensed systems, (d) to develop new insights into the subtleties of both three-dimensional and two-dimensional SALS theory and (e) to apply these new insights toward the development of new applications for the light scattering method. In order to accomplish these goals, SALS patterns from a wide range of polymers including isotactic polypropylene, nylon 610, starch, poly(ethylene terephthalate), nylon 66, and isotactic polystyrene are examined; extensive use is made of a digital computer, which in this case acts as a mathematical diffractometer.

EXPERIMENTAL

Sample Preparation

Two types of samples are used in this study, suspensions of rice starch granules and solid films. The suspensions of rice starch were prepared by adding a weighed amount of the starch to a known weight of silicone immersion oil. Concentrations varying from 8 to 51% by weight of rice starch were prepared for the different experiments described in the text. The silicone immersion oil was a mixture of Dow Corning 710 fluid (η_s = 1.5347) and Dow Corning 550 fluid (η_s = 1.5012). Combinations of these immersion oils were prepared to provide different refractive index backgrounds for the rice starch granules.

Films were prepared of rice starch (Stein Hall, Lot No. 43885), isotactic polypropylene (Hercules Pro-fax 6623), and nylon 610 (Du Pont Zytel 31). The rice starch films were prepared by compression of 300 mg of starch at a pressure of 85 ton/in.[2] for 3–5 min. The resulting films averaged 3 mil in thickness and contained undamaged spherulites. Isotactic polypropylene films containing spherulites of 7 μ diameter were prepared by room temperature quenching from the melt. Portions of this film were then annealed for ten minutes in an oven at different temperatures. Nylon 610 films containing either negatively or positively birefringent spherulites were also prepared. One film, containing small negatively birefringent spherulites, was prepared by cooling from the melt to 190°C under pressure,

and another film, containing small positively birefringent spherulites, was prepared by quenching from the melt.

Optical Measurements

The refractive index of the immersion liquids was measured in a Bausch and Lomb dipping refractometer. The refractive index of the films was measured in an Abbé refractometer. Starch granules were measured by three different optical methods: (1) the birefringence of the spherulite granule was measured in a Zeiss polarizing microscope with an Ehringhaus compensator; (2) the individual refractive indices parallel and perpendicular to the spherulite radius were measured in the Zeiss polarizing microscope using Zeiss interference attachments; and (3) the average refractive index of the spherulite was measured by the Becke method. The rice starch spherulites had a birefringence of $+0.01$ and an average refractive index of 1.530.

Small-Angle Light Scattering (SALS)

Flat-plate SALS patterns were obtained with the photographic arrangement shown in Figure 1. A Spectra Physics Model-132 continuous wave He-Ne gas laser was used as the source of polarized, monochromatic $(\lambda = 6328$ A$)$ light. The vertically polarized incident light, (E_0) from the laser impinges on the sample and is scattered, (E) by the spherulites. For deformed samples, the stretching direction (S.D.) is aligned parallel to the plane (Z) of the incident light. The scattered ray (E) passes through the analyzer and impinges on the flat-plate photographic film. The position of the scattered reflection is defined by two angles θ and μ. The radial angle θ is defined as the angle between the unit vectors $\mathbf{S_0}$ and $\mathbf{S}$ which specify the direction of the incident and scattered beams, respectively. The azimuthal (tilt) angle μ is defined as the angle between the Z axis (stretch direction) and the projection of the difference $\mathbf{S} - \mathbf{S_0}$ between the unit vectors on the y,z plane.
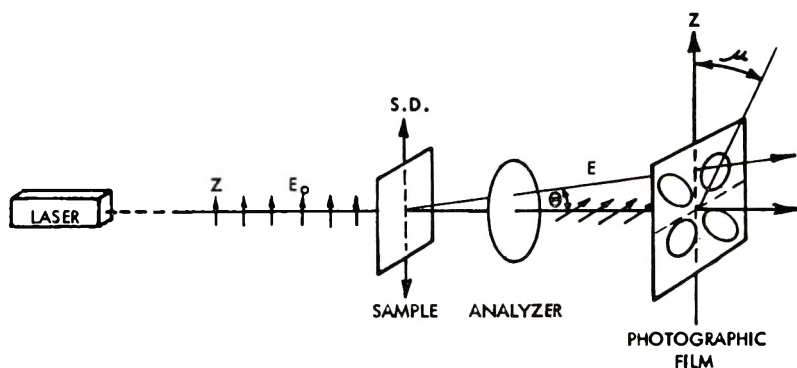
Fig. 1. Schematic diagram of the SALS system.
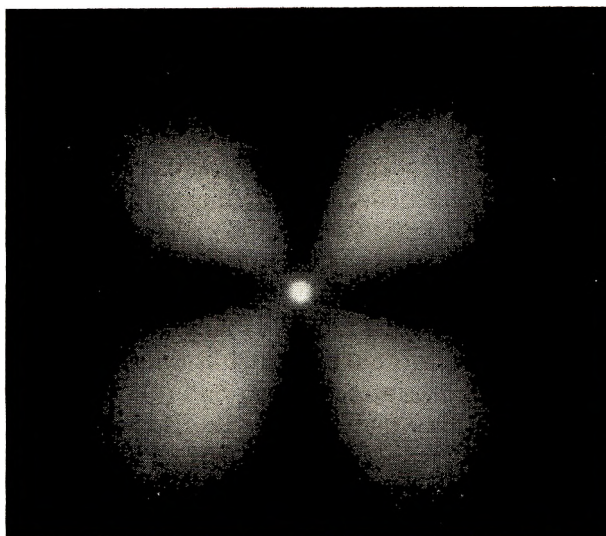
(a)
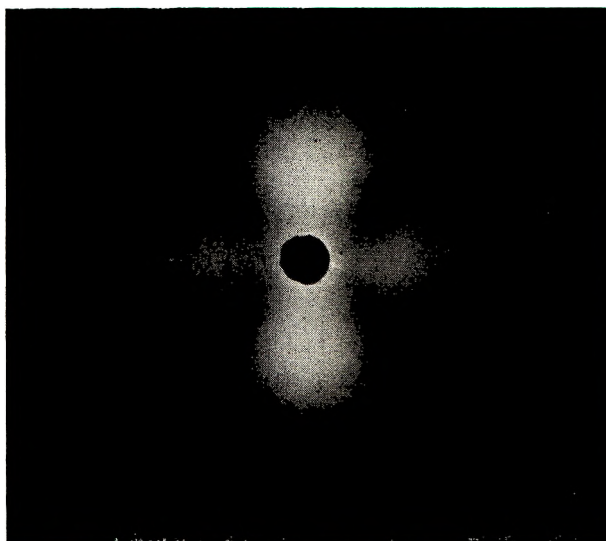
(b)

Fig. 2. Typical experimental SALS patterns from undeformed isotactic polypropylene film. The polarization direction is vertical: (a) H_v; (b) V_v.

An analyzer has been placed between the sample and the photographic film in Figure 1. When the plane of polarization of the analyzer is horizontal (i.e., the plane of polarization of the analyzer and of the incident light are perpendicular) an H_v SALS pattern is obtained (Fig. 2a). By convention, the subscript in the term H_v defines the plane of the incident polarized light which, here, is vertical. If the plane of polarization of the analyzer is vertical (i. e., the plane of polarization of the incident light

and of the analyzer are parallel) a V_V SALS pattern is obtained (Fig. 2b). To obtain results quickly, all photographs were taken with a Polaroid 4 × 5 Land Film Packet Type 55-P-N. A special vertical mounted sample oven was used for high temperature measurements.

RESULTS AND DISCUSSION

Spherulite Optics

This paper considers the consequences of the anisotropic optical character of spherulites on SALS the observed small-angle light scattering. Before examining the SALS theory, it is pertinent first to describe the structural elements of the spherulite and the appropriate optical parameters that are used throughout this study.

A polycrystalline polymer is composed of crystallites and noncrystalline regions which, under appropriate processing conditions, will arrange themselves into an ordered superstructure called a spherulite. Synthetic polymers, such as polyethylene, isotactic polypropylene, Penton,* nylon 66, nylon 610, isotactic polystyrene, and polyethylene terephthalate), and natural polymers, such as starch and silk fibroin, are examples of some of the many polymers that form one or more types of spherulites.

Structurally a spherulite may be described as a spherically symmetrical aggregate of crystalline and noncrystalline polymer. The crystallites are arranged in large part along radial fibrils which have a common center at the site of primary nucleation. Figure 3 is a phase-contrast micrograph of an isotactic polypropylene spherulite. Notice the radial fibrils all emanating from the central site of primary nucleation. The crystallites are aligned mainly along these radial fibrils, although secondary crystallization can occur in the interradial region. The noncrystalline polymer can also be both interradial and intraradial.

The intraradial crystallites generally have a preferred orientation with respect to the radial fibril direction in the spherulite. This orientation has been determined by micro x-ray diffraction[3−7] and electron diffraction studies[8−10] of selected regions of spherulites. These studies have usually shown that the direction of the molecular chain axis in the crystallite is oriented perpendicular (or at some angle toward the perpendicular) to the radial fibril direction in the spherulite. This observation suggests that the crystallites are arranged along the spherulite radii in the form of folded-chain lamellae, with their fast-growth face parallel to the radial fibril direction. A typical example of such crystallization is the preferred orientation that occurs in Type II isotactic polypropylene spherulites.[5] This is illustrated in Figure 4. (The helical chain axis of the isotactic polypropylene molecule is parallel to the c axis of the crystal.) It should not be assumed, however, that all polycrystalline polymers crystallize

* Registered trademark of Hercules Incorporated.

with the molecular chain axis of the crystallite oriented perpendicular
to the radial fibril direction of the spherulite. Starch, for example, has been
found to grow spherulitically in nature with the molecular chain axis
oriented parallel to the radial fibril direction[6] (Fig. 5).
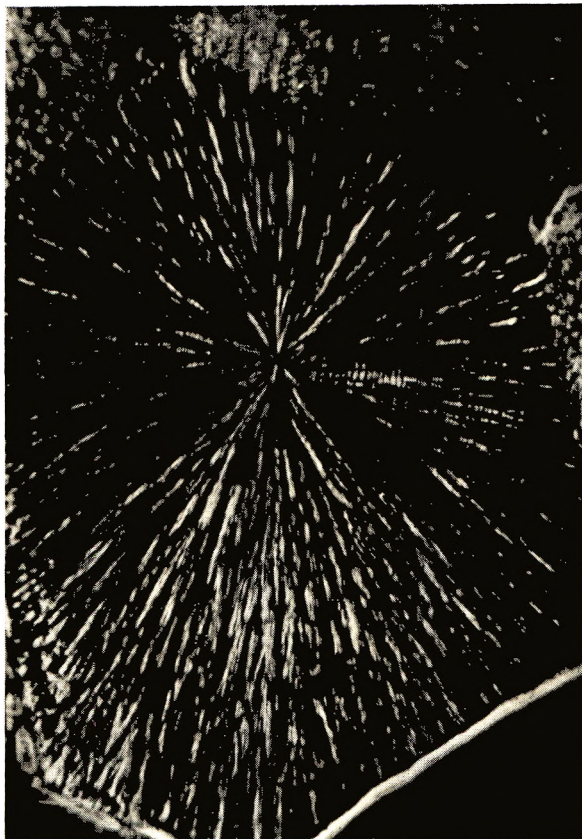
Fig. 3. Phase microscope photograph of an isotactic polypropylene spherulite.
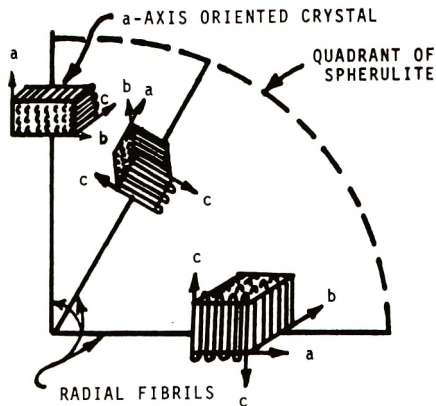
Fig. 4. Intraradial crystal arrangement in type II isotactic polypropylene spherulites.
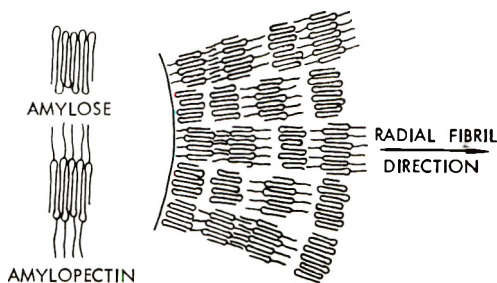
Fig. 5. Schematic representation of the intraspherulite molecular arrangement in starch.[12]

The characteristic preferred orientation of the crystallites with respect to the radial fibril direction in the spherulite imparts unique optical possibilities to the spherulite. Thus, depending on the processing conditions, the same polymer may form spherulites having positive, negative, or even mixed birefringence. Here the birefringence of the spherulite Δ_s is defined as $(n_r - n_t)$, where n_r is the refractive index parallel to the radial fibril direction and n_t is the refractive index perpendicular (tangential) to the radial fibril direction. If the noncrystalline polymer is assumed to be isotropic, the birefringence of the spherulite will be directly related to the birefringence of the crystallites along the radial fibril. In polymers, the largest refractive index n_γ is along the molecular chain axis while the refractive indices n_α and n_β are perpendicular to the molecular chain axis $(n_\beta > n_\alpha)$.

The spherulite type is characterized by the crystal unit cell and the sign of the birefringence of the spherulite. Hexagonal and tetragonal crystals are optically uniaxial, i.e., two of the axes of the crystal have the same length $(a = b)$ and are perpendicular to, and of different length than, the third axis (c axis). Thus, optically speaking, for a uniaxial crystal, $n_\alpha = n_\beta \neq n_\gamma$. If these uniaxial crystals are oriented along a radial fibril axis, so that the crystallites have rotational symmetry in the plane perpendicular to the radial fibril direction, two types of spherulite birefringence are possible. If the polymer chain axis is parallel to the spherulite radius (n_γ parallel to the radius) then $n_r > n_t$ [since under this condition $n_r = n_\gamma$, and $n_t = (n_\alpha + n_\beta)/2$] and the spherulite has a positive birefringence. If the chain axis is perpendicular to the spherulite radius (n_γ perpendicular to the radius) then $n_r < n_t$, since $n_t = (n_\alpha + n_\gamma)/2$, and $n_r = n_\beta (= n_\alpha)$. Consequently for this case the spherulite has a negative birefringence. The optical indicatrices representing these two conditions are shown in Figure 6.[11] The length of the lines representing n_r and n_t in the figure are drawn proportional in length to the crystal refractive index for light traveling parallel to the direction of that line. Since the index of refraction varies according to the vibration direction of light in the crystal in going from principal refractive index n_r to principal refractive index n_t, the trace of this path takes the form of an ellipse. On the other hand, since the crystals rotate randomly in the plane per-

$$n_r < n_t \qquad\qquad n_r > n_t$$
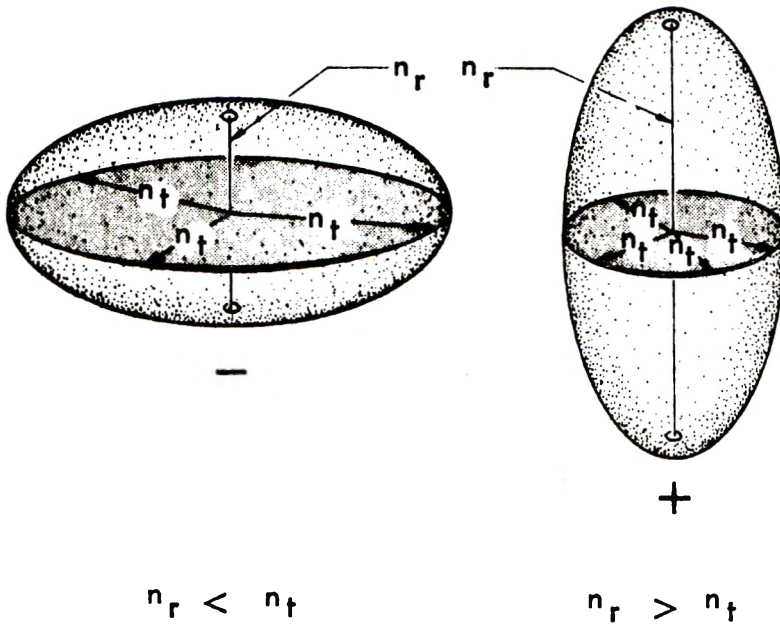
Fig. 6. Positive and negative uniaxial indicatrices. The circular section for each is heavily shaded.[11]

pendicular to n_r the crystal refractive indices in this plane have a common value n_t. Thus the sector lengths in the perpendicular plane are represented by a circle with a radius n_t.

Crystals of the orthorhombic, monoclinic, and triclinic classes are characterized by the fact that they all have crystal axes of different length $(a \neq b \neq c)$ and the angles between the crystal axes can be equal to, or different from, $90°$ depending on the specific crystal class. Such crystals will exhibit different refractive indices along the three principal axes (i.e., $n_\alpha \neq n_\beta \neq n_\gamma$) and are called biaxial crystals. If biaxial crystallites are oriented along a radial fibril so that they are rotationally symmetrical (i.e., randomly rotated) in the plane perpendicular to the radial fibril direction, then n_t will be equal to the average of the two perpendicular crystal refractive indices, the system will then be represented by a uniaxial indicatrix (Fig. 6), and the symmetry axis of the radial fibril will be parallel to the radial fibril direction. The unequal nature of the principal refractive indices of the biaxial crystallite, however, allows this system a further optical option in the spherulite. If the chain axis is parallel to the radial fibril direction (n_γ parallel to the radius) then, as with the uniaxial crystal, Δ_s will be positive. However, if the chain axis is perpendicular to the radial fibril axis (n_γ is perpendicular), two possibilities can be considered: (1) if n_α is parallel to the radius, the spherulite birefringence Δ_s is negative because n_α is less than both n_β and n_γ (see above) and hence $n_t > n_r$; (2) if n_β is parallel to the radius, n_r can be greater or smaller than n_t. Since

the molecular chain axis is rotationally symmetrical around the radial axis, n_t will equal the average refractive index of the two (n_γ and n_α) refractive indices. Depending on the magnitude of n_α, then, n_t can be either greater or smaller than n_r, (which is dependent only on n_β). If n_t is greater than n_r, the birefringence will be negative [as in (1)], but if n_t is smaller than n_r, the birefringence will be positive. Hence, the sign of the spherulite birefringence is a function of crystallite orientation.

The type II isotactic polypropylene spherulite (Fig. 3) is an example of how preferred orientation of biaxial crystallites can result in a negatively birefringent spherulite. The arrangement of the monoclinic crystallites within the spherulite is shown schematically in Figure 4. In isotactic polypropylene, n_α is along the a axis of the monoclinic crystal, n_β is along the b axis of the crystal, and n_γ is along the c axis (molecular chain axis) of the crystal. Under the conditions of preparation these crystals grow radially from the nucleating center with their fast growth face parallel to the radial fibril axis. This means the a axis of the crystallite is parallel to the radial fibril direction (i.e., parallel to the symmetry axis of the fibril), while the b axis and c axis are perpendicular and rotationally symmetrical with the radial fibril direction.[5] Thus, $n_r = n_\alpha$, while $n_t = (n_\beta + n_\gamma)/2$. Since $n_\gamma > n_\beta > n_\alpha$, the tangential refractive index n_t is greater than the radial refractive index n_r, and the spherulite birefringence ($\Delta_s = n_r - n_t$) is negative.

Starch granules, which grow as individual spherulites (Fig. 5),[12] are an example of positively birefringent spherulites. These spherulites, depending on the source, contain various proportions of the linear molecule amylose and the branched molecule amylopectin. Rice starch, which is used in this study to test the small-angle light-scattering theory, (see next section) is composed of approximately 18% amylose with the rest amylopectin. The crystallites show an A-type x-ray diffraction pattern, and the small-angle x-ray diffraction measurements yield a long spacing (distance between crystallite centers) of 90.2 Å. Micro x-ray diffraction of a starch granule[6] has shown that the molecular chain axis direction in the crystal is oriented parallel to the spherulite radial fibril axis ($n_r = n_\gamma$). Since here $n_t = (n_\alpha + n_\beta)/2$ and $n_\gamma > n_\beta > n_\alpha$, the starch spherulite must have a positive birefringence.

Experimental Verification of the Small-Angle Light-Scattering (SALS) Equations

A spherulite must be characterized optically as an anisotropic sphere. This is because the crystallites have preferred orientation along the spherically arrayed fibrils and impart optical anisotropy to them. Realizing this, Stein and Rhodes[1] developed the small-angle light-scattering theory based on a model of an anisotropic sphere immersed in either an isotropic or an anisotropic medium. An accurate experimental test of the validity of their equations would have required availability of individual, separable spherulites that could be immersed in media of different refractive indices.

Unfortunately, separable spherulites were not available, and investigators had to use spherulitic polymer films and fibers as substitutes.[1,5,13] Though these experimental systems did not fulfill the theoretical requirement of spherulite independence, the experimental results suggested, at least for H_V SALS behavior, that the form of the theoretical scattering envelope and the sphere size predictions were valid.

The correct form of the three dimensional small-angle light scattering equations for anisotropic spheres (see Appendix I for the theoretical treatment) is

$$I_{V_v} = A\rho^2 V_0^2 (3/U^3)^2 \{(\alpha_t - \alpha_s)(2 \sin U - U \cos U - \mathrm{Si}U)$$
$$+ (\alpha_r - \alpha_s)(\mathrm{Si}U - \sin U) + (\alpha_r - \alpha_t)[\cos^2(\theta/2)/\cos\theta] \cos^2\mu$$
$$\times (4 \sin U - U \cos U - 3\mathrm{Si}U)\}^2 \quad (1)$$

$$I_{H_v} = A\rho^2 V_0^2 (3/U^3)^2 \{(\alpha_r - \alpha_t)[\cos^2(\theta/2)/\cos\theta] \sin\mu \cos\mu$$
$$\times (4 \sin U - U \cos U - 3\mathrm{Si}U)\}^2 \quad (2)$$

where I_{V_v} and I_{H_v} denote scattered intensities; V_0 is the volume of the anisotropic sphere; α_t and α_r are the tangential and radial polarizabilities of the sphere, respectively; α_s is the polarizability of the surroundings; θ and μ are the radial and azimuthal scattering angles, respectively; and A is a proportionality constant. $\mathrm{Si}U$ is the sine integral defined by

$$\mathrm{Si}U = \int_0^U \frac{\sin x}{x}\, dx \quad (3)$$

and is solved as a series expansion sum for computational purposes. The geometric polarization correction term[2] ρ is defined as,

$$\rho = \cos\theta\,(\cos^2\theta + \sin^2\theta\,\cos^2\mu)^{-1/2} \quad (4)$$

and U is the sphere shape-factor;

$$U = (4\pi R_0/\lambda')\sin(\theta/2) \quad (5)$$

where R_0 is the radius of the anisotropic sphere, and λ' is the wavelength of light in the medium.

The theoretical equations above were programmed for an EMR 6130 computer with a Calcomp plotter attachment.[14] (The program is available from the author, C. E. Green of this laboratory.) With sample data sets 1 and 2 listed in the program, the computer was used as a mathematical diffractometer to produce the H_V SALS and V_V SALS patterns shown in Figure 7. These are constant intensity contour plots with the symbols representing different intensity levels. The intensity identification system used in this and the succeeding contour plots is that the squares represent the highest intensity profile, the crosses represent a medium intensity profile, and the triangles represent a week intensity profile. The theoretical SALS patterns in Figure 7 should be compared with the experimental SALS patterns in Figure 2. These experimental patterns
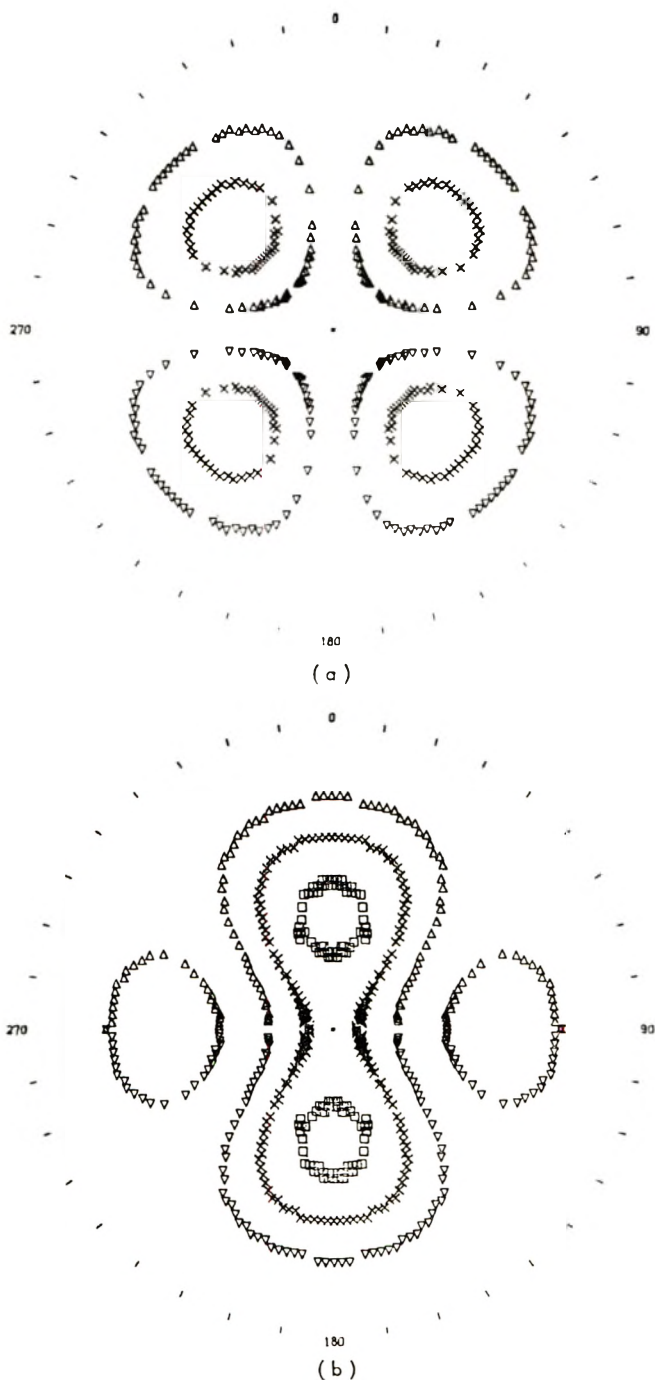
Fig. 7. Theoretical SALS patterns for unoriented isotactic polypropylene film (test patterns I and II). The polarization direction is vertical: (a) H_v; (b) V_v.

were obtained from a cast isotactic polypropylene film which contained undeformed type II, negatively birefringent spherulites.

H_V SALS: An Acceptable System

The similarity between the theoretical H_V SALS pattern in Figure 7 and the experimental one in Figure 2 suggests that the theoretical H_V SALS equation is correct and can be applied to a nonindependent spherulite scattering system.   The most obvious correspondence between the two patterns is that both have the same characteristic four-leaf-clover shape. Further examination of the theoretical H_V SALS pattern shows that the maximum intensity in any lobe of the pattern occurs at an azimuthal angle, μ, of 45°.   This is also visually obvious in the experimental pattern (Fig. 2) and has been photometrically demonstrated as well.[13]   Again in the theoretical H_V SALS pattern the highest intensity (squares) in any lobe of the four-lobed pattern always concentrates for a given spherulite diameter, at a particular radial angle, θ.   Here θ is represented by the distance of the intensity maximum of one of the lobes from the center of the whole pattern.   This particular aspect of the theory has led to a most important application of the H_V SALS measurement—the determination of spherulite size.

The characteristic behavior of the H_V SALS pattern is determined theoretically by the form of the shape factor, U.   In an undeformed film the spherulite is spherical in shape and the shape factor takes the form of eq. (5).   Owing to the dependence of the terms $(3/U^3)(4 \sin U - U \cos U - 3 \mathrm{Si}\ U)$ in the H_V equation on U, a maximum intensity will always be observed at a value of $U = 4.09$.   This means the average spherulite radius can be obtained from the H_V SALS pattern, since the distance from the center of the H_V SALS pattern to the intensity maximum of one of the lobes, in conjunction with the known sample-to-film distance, is a measure of the polar angle θ_{max}.   Once the value of the polar angle, θ_{max} has been obtained, and corrected for the refractive index of the polymer so that it equals the polar angle within the polymer film, the value of R_0 can be calculated by using the equation:

$$R_0 = 1.025\lambda'/\pi \sin (\theta_{max}/2)$$

Since the polar angle θ_{max}, at which maximum intensity appears, is inversely proportional to the radius R_0, of the spherulite, small spherulites will have a clover-leaf pattern with maxima at large radial angles while large spherulites will have maxima at small radial angles.   This is illustrated in Figure 8, where the effect of isotactic polypropylene spherulite size on the radial position of the H_V SALS pattern is shown.   These H_V SALS patterns were obtained by keeping the sample-to-film distance constant during the experiment.

The confidence gained through the excellent agreement of the theoretically predicted H_V SALS behavior with experimental observation has led to increasing application of this new technique to the solution of

SAMPLE TO PHOTOGRAPHIC FILM DISTANCE FIXED AT 70 MM.

AVERAGE SPHERULITE DIAMETER 1.6 μ

AVERAGE SPHERULITE DIAMETER 4.5 μ

AVERAGE SPHERULITE DIAMETER 8.2 μ
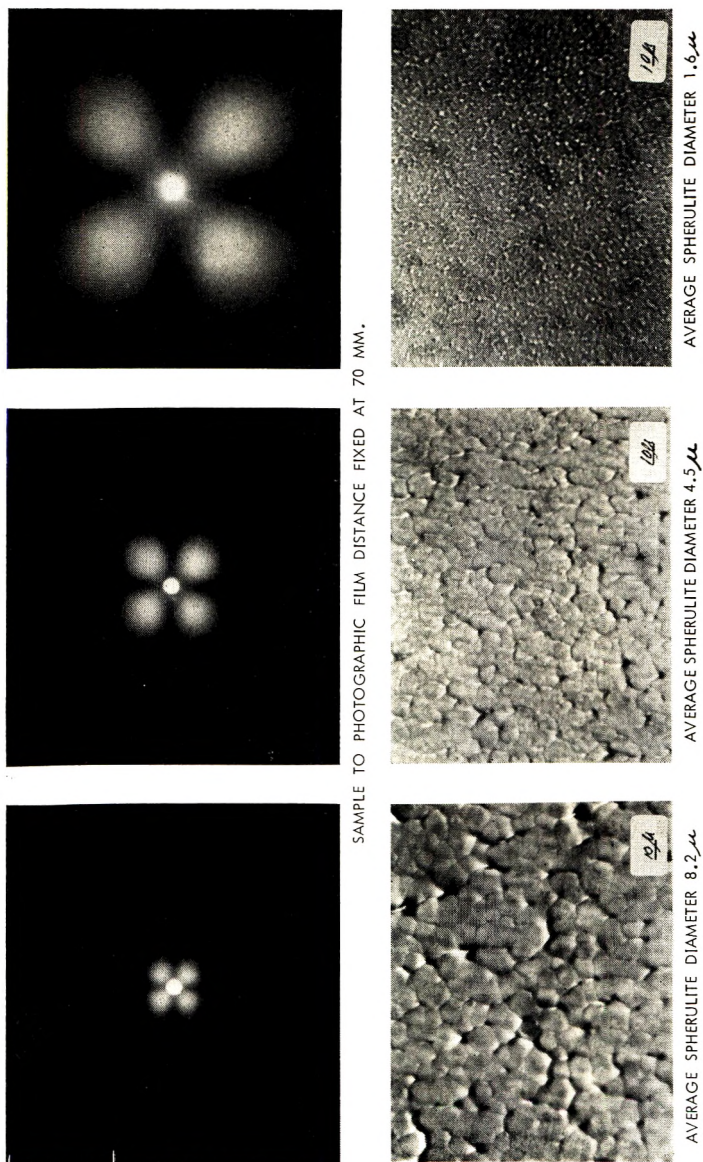
Fig. 8. Effect of spherulite size on the position of the H_v SALS pattern.
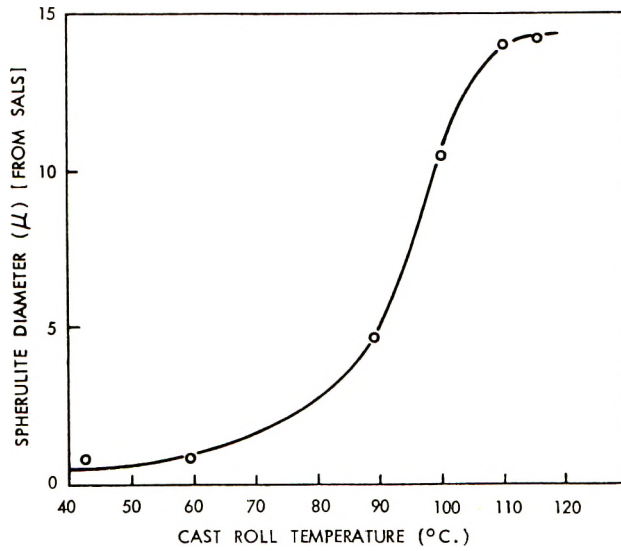
Fig. 9. Effect of casting roll temperature on spherulite size (speed and melt temperature constant).
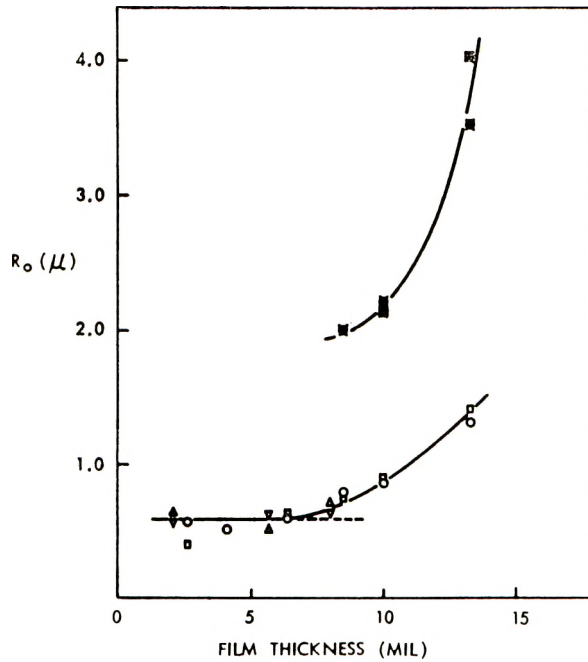
Fig. 10. Effect of film thickness and casting temperature on spherulite dimensions in cast and preheated films: (△) cast at 110°C; (▽) preheated at 110°C; (□, ⊠) cast at 135°C; (O, ■) preheated at 135°C.
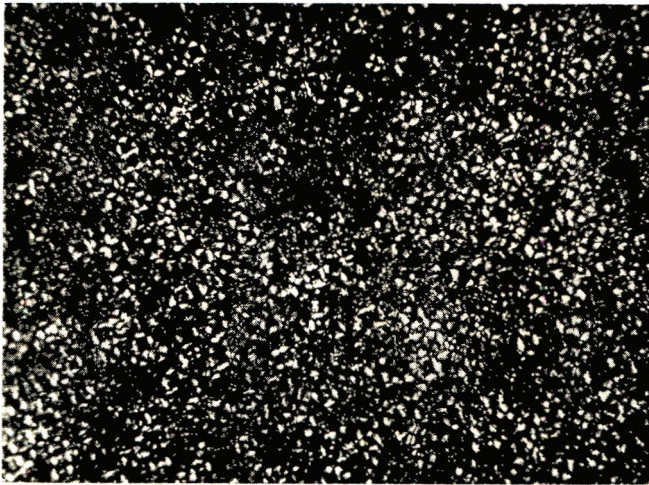
POLARIZING MICROSCOPE
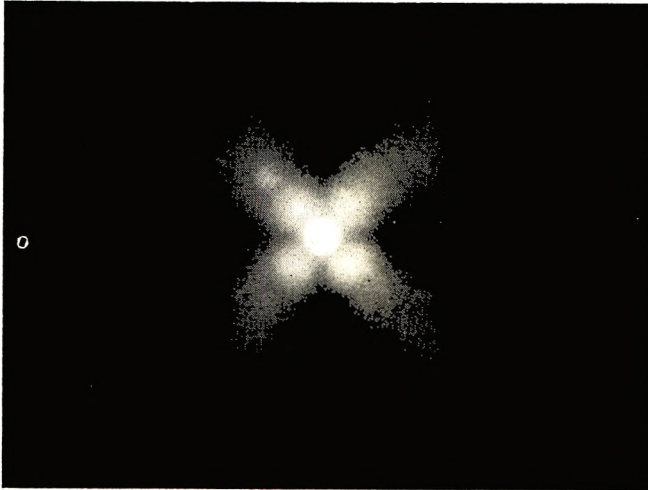
H_V SALS

Fig. 11. Effect of a bimodal spherulite size distribution on the H_v SALS pattern. Average spherulite diameters equal 2.5μ and 10.7μ.

practical problems. For example, average spherulite size determined from the H_V SALS pattern, can be correlated with cast roll temperature during film processing (Fig. 9). Similarly, the H_V SALS pattern can be used on a processing line to indicate when increased film thickness prevents efficient quench. Non-uniform quench causes spherulites of different sizes to form on the different film surfaces (Fig. 10). The manner in which the presence of two distinct size ranges of spherulites manifests itself in the H_V SALS pattern is illustrated in Figure 11. Here the more intense inner pattern yields the average size of the large spherulites while

the larger, weaker intensity, outer pattern yields the average size of the smaller spherulites.

The point to be made here is that in all cases the experimental H_V SALS results support the validity of the theoretical H_V SALS equations even though the experimental systems do not satisfy the criteria of independent anisotropic spheres.

V_V SALS: A Critical Examination

Anisotropic Spheres. A careful examination of the assumptions underlying the small-angle light scattering theory for anisotropic spheres shows that the H_V SALS equation [eq. (2)] is not the appropriate one to use to test the theory.   The H_V SALS equation is only sensitive to changes in the size of the spherulites (i.e., is only dependent on the shape factor U) and is independent of any polarizability anisotropy.   This is because the polarizability anisotropy term $(\alpha_r - \alpha_t)$ acts solely as a constant multiplier in the H_V SALS equation. Since polarizability anisotropy is the cornerstone of the optically anisotropic sphere model, a realistic test of the SALS theory requires an examination of V_V SALS scattering, which is highly sensitive to the polarizability anisotropy of both the spherulite and its surroundings [see eq. (1) and Appendix I].

A comprehensive examination of V_V SALS scattering from polymer films was published in 1968.[15] In this study V_V SALS patterns were obtained from both negative and positive spherulites of polypropylene, nylon 610, poly(ethylene terephthalate), and nylon 66, as well as from spherulites of polyethylene and Penton.   Some of these V_V SALS patterns are shown in Figure 12.   The experimentally observed V_V SALS patterns were then compared with patterns calculated by using the theoretical V_V SALS equation of Stein and Rhodes.[1]   It was concluded from the theoretical study that patterns corresponding in form to those observed experimentally could be produced by changing the anisotropy of the spherulite surroundings while keeping the magnitude and absolute sign of the spherulite birefringence constant.   In other words, the spherulite surroundings had to be assumed anisotropic in order to fit the existing theoretical equations to the experimental patterns.

In a polymer film the spherulites are space-filling.   This means that the background environment of any spherulite in the film would be the average polarizability of all the surrounding spherulites.   Thus, if there is an equivalent number of spherulites in all directions, the average background polarizability is expected to be isotropic.   However, since polymer films are not ideal systems experimentally, it is possible to rationalize the theoretically required anisotropic character of the background on the basis that, (1) the spherulites are not independent scatterers as required by the theory, (2) internal strains might be produced during cooling to produce an anisotropic background, (3) multiple scattering and interparticle interference effects might predominate, or (4) orientation of noncrystalline

NEGATIVE SPHERULITES POSITIVE SPHERULITES

NYLON 6, 10

POLY(ETHYLENE TEREPHTHALATE)

NYLON 6, 6
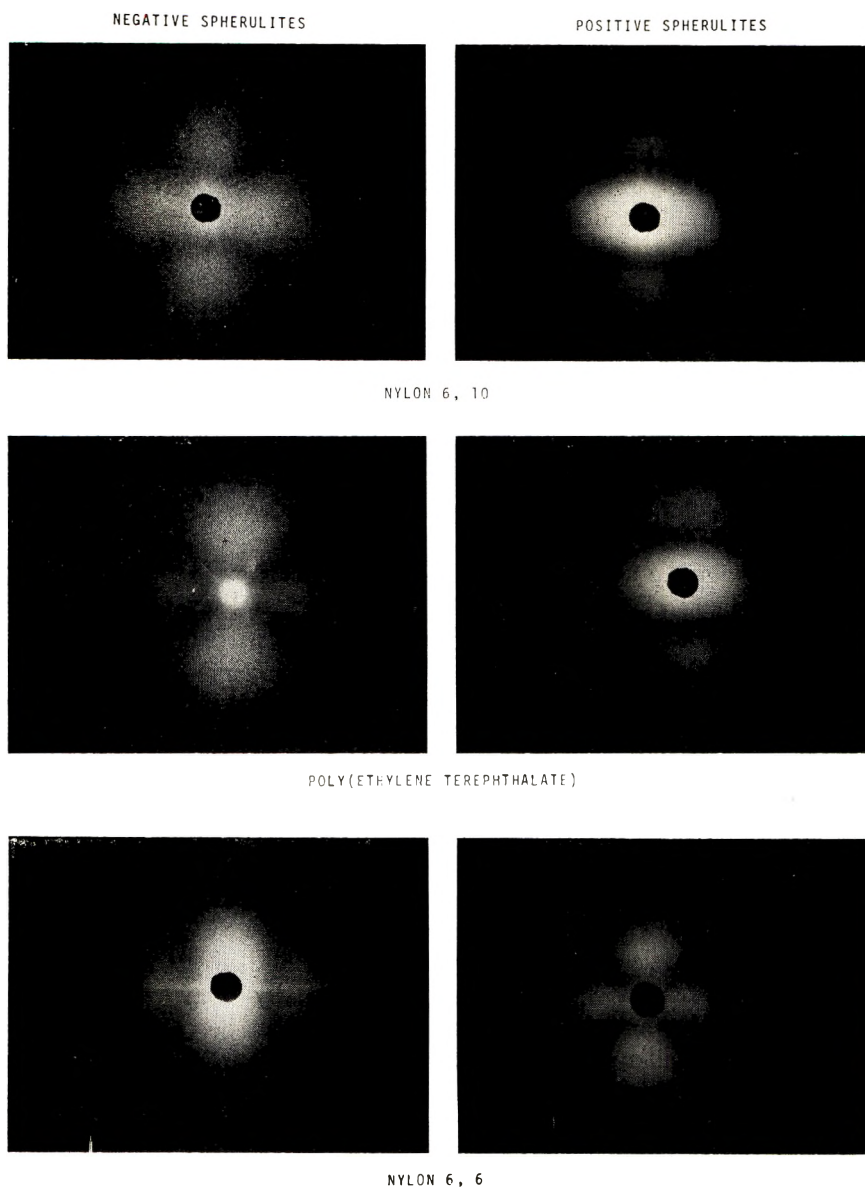
Fig. 12. Representative V_v SALS patterns from both negative and positive spherulites of several polymers.

chains might occur during crystallization, a factor not considered in the theory. Though these rationalizations might explain the theoretically required background anisotropy, a careful examination of the magnitude of the background anisotropy that was theoretically required to produce acceptable patterns makes this approach physically untenable. For in order to produce acceptable patterns from the theoretical V_v SALS equa-

tion it was necessary to assume that the background anisotropy was greater than that of the spherulite (see Appendix I).

Thus, the present state of the SALS theory for anisotropic spheres suggests that an in-depth study of the system is in order. In particular, it would be desirable to examine experimentally the quantitative effect of background environment on the V_V SALS scattering from spherulites which act as independent scatterers, and also to re-evaluate the theoretical V_V SALS equation. A re-evaluation of the V_V SALS equation is reported in Appendix I. The conclusion of the study reported in Appendix I is that there was an error in sign in the original V_V SALS equation[1] which was corrected but unrecognized in a later rederivation of the theory.[2] Due to this error the polarizability anisotropy term, which is correctly listed in eq. (1) as $(\alpha_r - \alpha_t)$, had the incorrect form $(\alpha_t - \alpha_r)$. This incorrect form of the equation is presently in general use.[16-19] It should be noted that, as a consequence of the present study, Stein et al.[20] have re-examined their earlier derivation and agree with us that there was an error in sign in the original SALS equations.

A change of the anisotropy term to the correct form shown in eq. (1) has a profound effect on the acceptability of the V_V SALS equation. The corrected V_V SALS equation predicts the experimentally observed form of the V_V SALS patterns on the assumption that the background medium is isotropic, a conclusion which is in agreement with physical expectations. Thus, the V_V SALS pattern shown in Figure 7b was calculated from eq. (1) with the assumption of an isotropic background. This theoretical V_V SALS pattern is seen to compare favorably with that obtained experimentally from type II isotactic polypropylene spherulites (Fig. 2b).

Starch Granules. The similarity between the shape of the theoretical V_V SALS patterns calculated by using the corrected equation, which contains the physically reasonable assumption of background isotropy, and the V_V SALS patterns observed experimentally from polymer films, suggests that the anisotropic sphere model can now be used to describe the observed small-angle light scattering from a spherulitic system. Still needed, however, to test the theory properly, is a quantitative characterization of the correspondence between theoretical and observed changes in the V_V SALS patterns. This requires observation of the scattering from separable spherulites of known optical character, as the refractive index of the surrounding isotropic medium is changed. Fortunately, a recent study by Borch and Marchessault[17] has shown that starch granules, which grow as isolated spherulites, produce H_V SALS and V_V SALS patterns. Thus, by using starch granules immersed in media of known refractive index as an ideal scattering system, it is possible to quantitatively test the anisotropic sphere scattering theory.

Our examination of a large number of starch systems (corn, wheat, rice, tapioca, waxy rice, and potato) showed that rice starch yields the most uniform scattering patterns when immersed in silicone oil. The

average diameter of the rice-starch spherulites ranged from 3 to 5 μ. Their average refractive index was determined as 1.530; the radial refractive index was 1.537; the tangential refractive index was 1.527; and the average birefringence was 1×10^{-2}. The average refractive index of the medium was calculated from the measured average refractive index of both the silicone oil and the rice starch by using the Gladstone-Dale relation,[21]

$$\frac{w(\bar{n}_{AV} - 1)}{\rho} = \frac{w_p(\bar{n}_p - 1)}{\rho_p} + \frac{w_s(\bar{n}_s - 1)}{\rho_s}$$

where, w, w_p, w_s are the sample, polymer, and solvent weights, respectively; ρ, ρ_p, ρ_s are the sample, polymer, and solvent densities; $\bar{n}_{AV}$ $\bar{n}_p$, n_s are the sample, polymer, and solvent refractive indices; and V, V_p, V_s are the sample, polymer, and solvent volumes (e.g. $V = w/\rho$). This relation can be rewritten as,

$$\bar{n}_{AV} = \beta \bar{n}_p + (1 - \beta)\bar{n}_s$$

where, $\beta = V_p/V$, is the volume fraction of polymer. The densities of the rice starch and silicone oil were taken as 1.50 g/cc and 1.156 g/cc, respectively. By substituting the measured refractive index values of both the spherulite and the background for the appropriate polarizability terms in the theoretical V_V SALS equation [eq. (1)], it is now possible to compute theoretical V_V SALS patterns and compare them directly with experimental patterns produced under the same optical conditions.

One final experimental condition, required by the anisotropic sphere theory, is that the spherulites should be present at a concentration low enough for them to act as independent scatterers. At the same time, the concentration must be high enough to obtain maximum information from the V_V SALS pattern. This concentration problem is illustrated in Figure 13. In each section of the figure, the photomicrograph and the V_V SALS pattern are from the same region of the sample, while the theoretical pattern was obtained by using eq. (1) in conjunction with the actual measured refractive indices of the sample. The intensity levels in the theoretical calculation were chosen to represent the level of information represented in the observed V_V SALS pattern. Figure 13a was obtained from a sample containing 6% by volume of starch (weight fraction 0.08). The V_V SALS pattern obtained from this sample is too weak; only the most intense lobes are observable. The low intensity horizontal streak is hidden behind the beam stop and is too weak to be resolved on the photographic film. Use of a longer exposure time only overexposes the film; it does not reveal additional information. Figure 13b was obtained from a sample containing 16.7% by volume of starch (weight fraction 0.20). The higher concentration increases the intensity of the V_V SALS pattern so that both the more intense lobes and weaker intensity horizontal streak are identifiable. Figure 13c was obtained from a sample containing 40% by volume of starch (weight fraction 0.46). This V_V SALS pattern

V_V SALS (THEORETICAL)
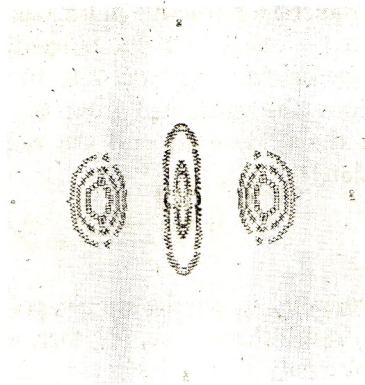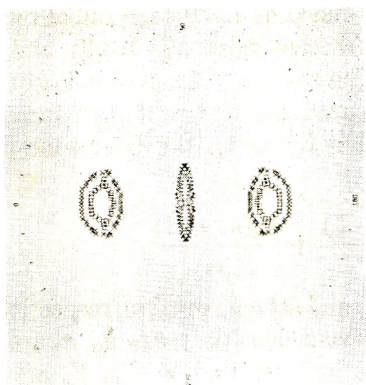
V_y SALS (EXPERIMENTAL)

PHOTOMICROGRAPH

a

b
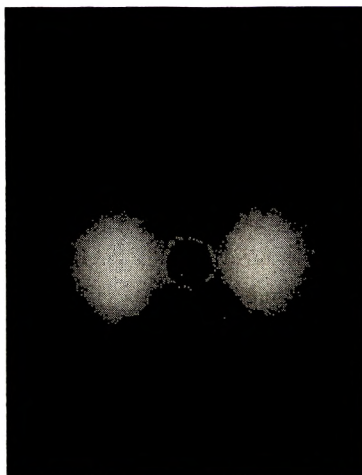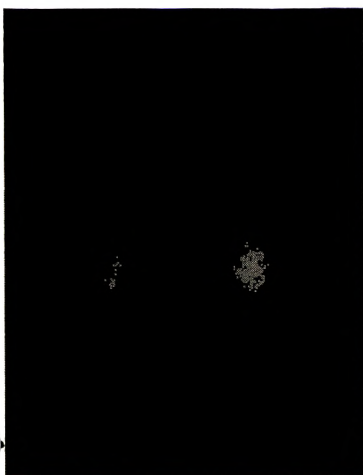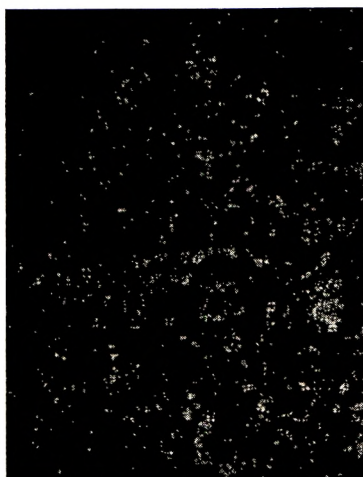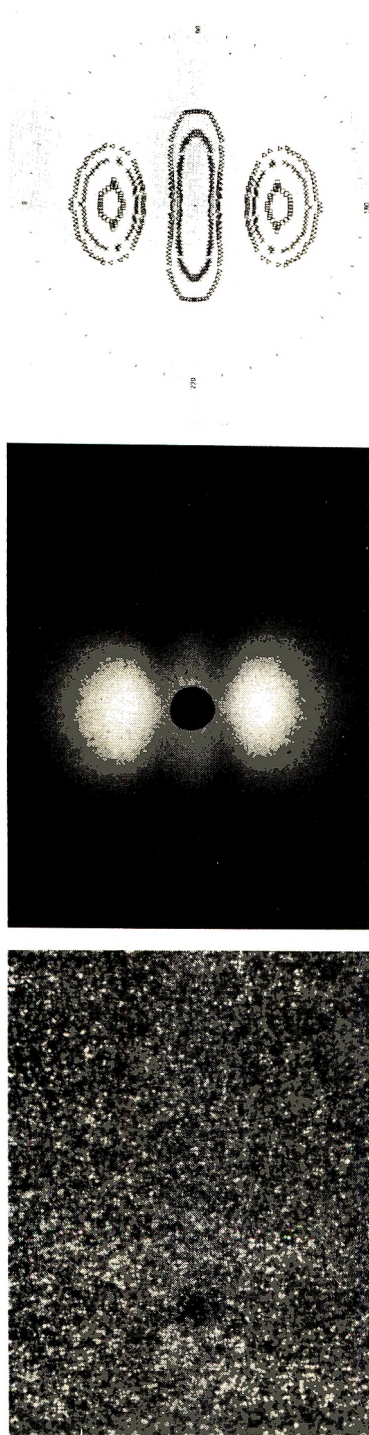
Fig. 13. Effect of increasing concentration on the V_v SALS pattern from rice starch granules: (a) 6% starch; (b) 16.7% starch; (c) 40% starch.
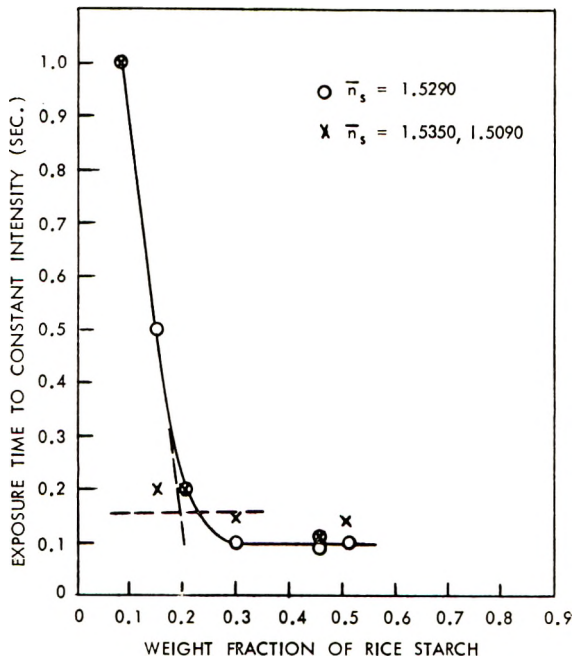
Fig. 14. Effect of rice starch concentration on the exposure time to constant intensity.

is more intense (and, therefore, more striking) than that of Figure 13*b* but contains no additional information.

Clearly, from the point of view of independence of spherulites, the lowest concentration of spherulites is preferred, while from an experimental point of view the highest concentration is desirable. Figure 14 shows how this problem was solved experimentally. The time required for the most intense region of the V_v SALS pattern to reach a given intensity was plotted against the weight fraction of starch in the sample. The time to a given intensity would be expected to decrease as a direct function of the concentration of starch in the region where the spherulites act independently (i.e., direct addition). When the scatterers no longer act independently the intensity will not be proportional to the fraction of scatterers and the rate of change of the time to a given intensity as a function of concentration will decrease. Different concentrations of starch immersed in three media were examined. The media consisted of silicone oil mixtures of low ($n_s = 1.5090$), high ($n_s = 1.5350$), and intermediate ($n_s = 1.5290$) refractive indices. The data are plotted in Figure 14. The highest concentration of starch still present on the initial linear region of the plot (weight fraction of 0.20) was chosen as the concentration to be used to test the small-angle light scattering theory.

Figures 15–17 show the V_v SALS patterns obtained experimentally from rice starch immersed in media of different refractive indices. The experimentally determined average refractive index (using the Gladstone-

Dale relation) is listed under each pattern. Alongside each experimental pattern is the theoretically predicted V_V SALS pattern calculated using the spherulite and background refractive indices found experimentally. Not only are the correct shapes of the V_V SALS patterns predicted but the correct trend in change of shape with changing background refractive index is also predicted. Thus, theory predicts (see Appendix I), for a positive spherulite, that the V_V SALS pattern observed when the spherulite is immersed in a medium of low refractive index (i.e., less than the value of the tangential refractive index of the spherulite) will have its maximum intensity in the central elliptical region of the pattern, with upper, outer lobes of weaker intensity (see $\bar{n} = 1.5193$ in Fig. 15). As the average refractive index increases and approaches the tangential refractive index of the spherulite (see $\bar{n} = 1.5272$ in Fig. 15) the high-intensity center lobe diminishes in size and intensity, while the upper, weaker lobes remain at the same intensity but draw in their crescent wings to form more nearly circular lobes. At this point, however, the center lobe is still more intense than the outer lobes.

As the average refractive index of the medium continues to increase toward the average refractive index of the spherulite (see $\bar{n} = 1.5308$ in Fig. 16), dramatic changes occur in the appearance of the V_V SALS pattern. The center lobe quickly diminishes in intensity and size to the point where the weak ellipse is only barely visible (see $\bar{n} = 1.5291$) on the photographic film. The upper lobes are now the most intense, not by virtue of any increase in intensity on their part, but simply as a consequence of the large decrease in intensity of the central region. This central region can be seen to split and form two side-lobes on the theoretical pattern, as the refractive index continues to increase, though their intensity is too low to pick up on the photographic film. This split and separation makes room for the outer lobes which now begin to extend down into the central region of the pattern. The predicted movement of the outer lobes of the V_V SALS pattern toward the center of the pattern can be readily followed, with increasing refractive index, in the experimental patterns of Figure 16.

As the refractive index increases beyond that of the average refractive index of the spherulite (see Fig. 17) the two upper lobes merge ($\bar{n} = 1.5327$) and increase in intensity (the squares denoting highest intensity reappear). This is a pattern of change that continues smoothly as the refractive index of the medium continues to increase ($\bar{n} = 1.5335$, $\bar{n} = 1.5340$).

These results demonstrate conclusively that the SALS theory of anisotropic spheres, as represented by eq. (1), correctly represents the observed scattering from spherulites. It is useful at this point to see how these theoretical and observed patterns from spheres differ from those predicted for disks having the same optical character. Such an examination is not academic. The accepted view has been that profound differences exist in the basic shape of the V_V SALS patterns obtained from disks and spheres,[22,23] a viewpoint which has already led to errors in the interpretation of experimentally determined patterns.[18]

EXPERIMENTAL   THEORETICAL

$\bar{n} = 1.5193$

$\bar{n} = 1.5234$
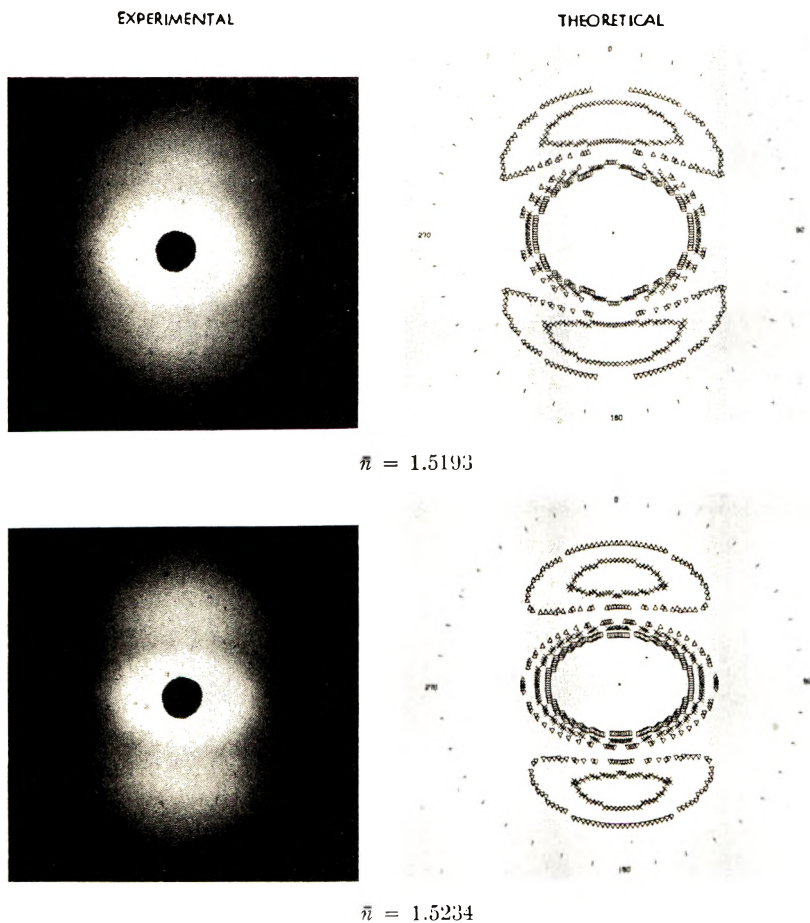
Fig. 15 (*continued*)

Anisotropic Disks.   The two-dimensional theory of SALS from optically anisotropic disks[22,24] and the three-dimensional theory for optically aniso-tropic spheres are functionally analogous (see Appendix 1).   This suggests that there should not be profound differences in the gross general form of the scattering envelopes predicted by the two theories, but instead only subtle differences in the character of the patterns should appear.   The disk V_V SALS equation derived from the two-dimensional theory for anisotropic disks[22,24] was programmed for the EMR-6130 computer.[14]   Theoretical V_V SALS patterns were then plotted for anisotropic disks using the same optical parameters previously used for the starch spheres.   The resulting anisotropic disk patterns are plotted in Figures 18 and 19.   These patterns should be compared to the equivalent patterns calculated for spheres in Figures 15–17.

It is apparent from comparing the V_V SALS patterns in Figures 18 and 19 with those in Figures 15–17 that the gross general shapes of the disk and sphere patterns are the same.   This is in contradiction to earlier conclu-

$\bar{n} = 1.5261$

$\bar{n} = 1.5272$
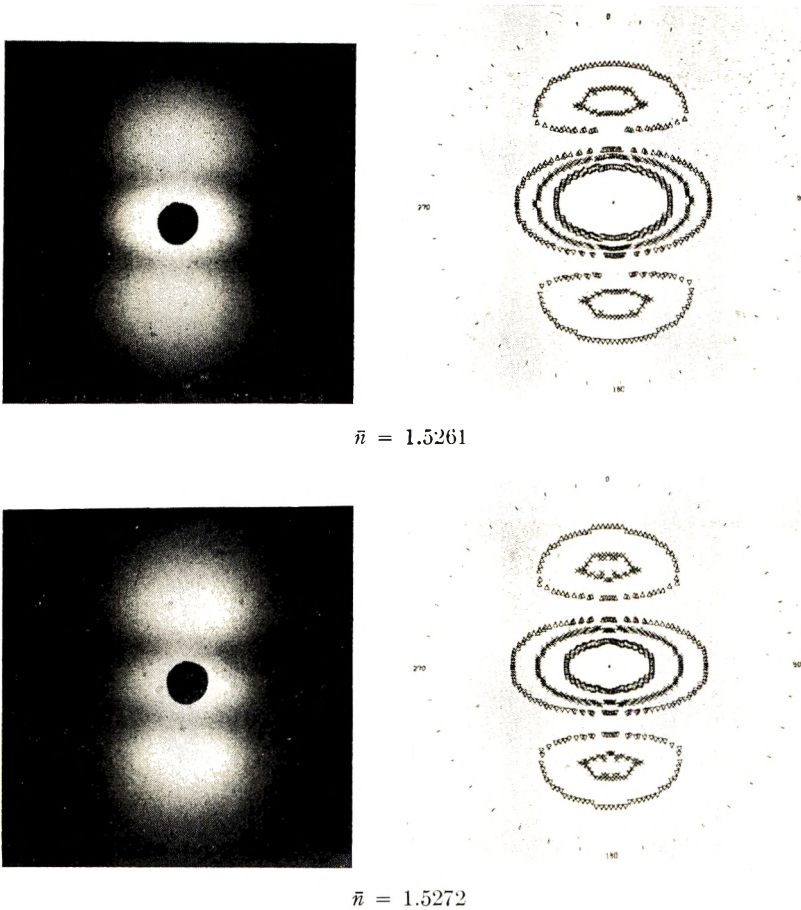
Fig. 15. Comparison of the experimentally observed V_v SALS patterns from rice starch granules with those predicted theoretically under the same optical conditions. The average refractive index of the background is listed under each set of V_v SALS patterns.

sions[22,23] and is a consequence of the present change in the V_V SALS equation for spheres [eq. (1)] from that originally reported.[1] There are, however, differences in both the relative intensity of the lobes, and in their observed rate of change of shape with changing refractive index. This suggests that the small-angle scattering of disks can be distinguished from that of spheres. Disk theory predicts (Fig. 18) for a positively birefringent disk, that if the disk is immersed in a medium of low refractive index (i.e., the refractive index of the medium is less than the value of the tangential refractive index of the disk) the observed V_V SALS pattern will have its maximum intensity in the central elliptical region of the pattern, and the upper outer lobes will be of weaker intensity (see $\bar{n} = 1.5193$ in Fig. 18). This characteristic of disk scattering behavior is the same as that predicted for spheres by sphere scattering theory. As the average refractive index of

EXPERIMENTAL   THEORETICAL

$\bar{n} = 1.5285$

$\bar{n} = 1.5291$
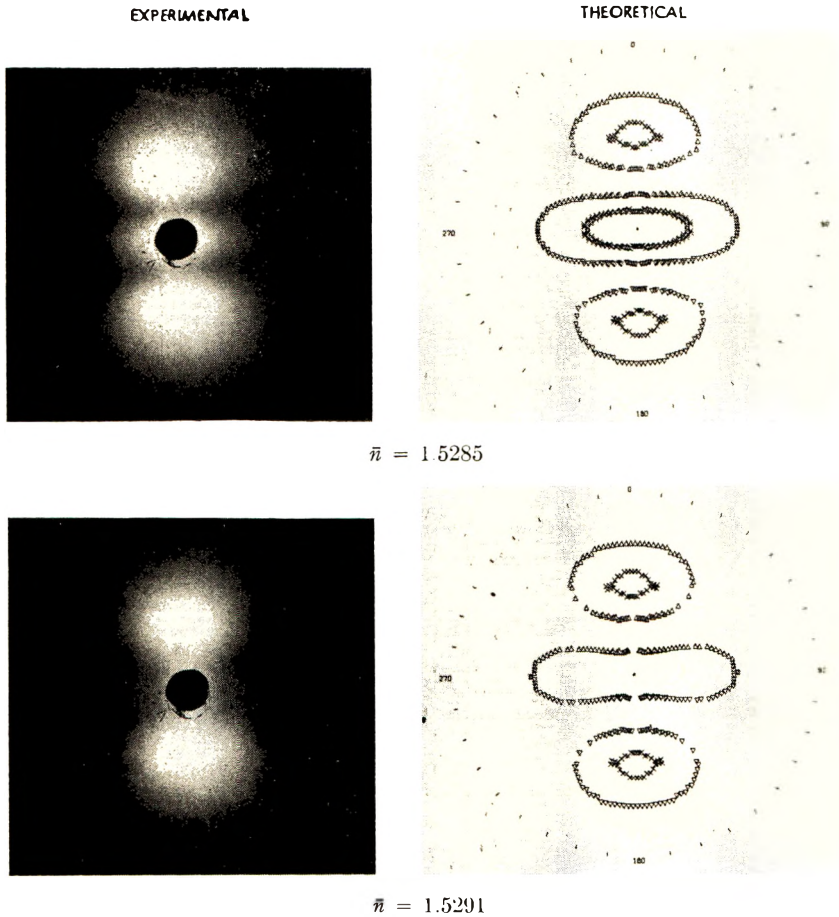
Fig. 16 (*continued*)

the medium increase in this region and approaches the tangential refractive index of the disk (see $\bar{n} = 1.5272$) in Fig. 18), the high-intensity center lobe diminishes in size and intensity, again in agreement with the prediction for spheres by sphere scattering theory. The upper weaker-intensity lobes of the disk patterns also decrease in intensity as the refractive index increases, and at a faster rate than that of the center ellipse. This is contrary to sphere scattering theory which predicts little or no change in the intensity of the upper lobes with increasing refractive index (see Fig. 15). At this point, however, the center ellipse of both the disk and sphere patterns is still more intense than the outer lobes, so that experimental identification of the character of the scattering source would be difficult.

As the average refractive index of the medium continues to increase toward the average refractive index of the disk (see $\bar{n} = 1.5308$ in Fig. 19), significant differences appear in the character of the scattering from disks which should make experimental identification possible. Thus, when a

$\bar{n} = 1.5298$

$\bar{n} = 1.5308$
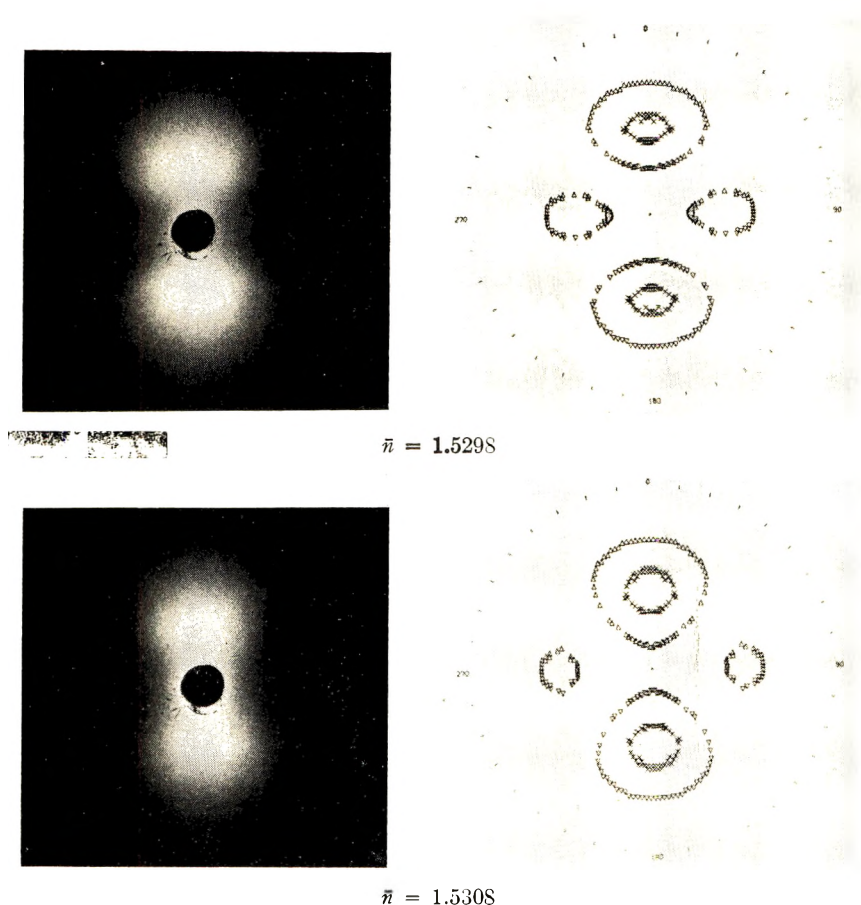
Fig. 16. Comparison of the experimentally observed V_v SALS patterns from rice starch granules with those predicted theoretically under the same optical conditions. The average refractive index of the background is listed under each set of V_v SALS patterns.

refractive index of 1.5291 is reached (Fig. 18), the intensity of the upper lobes of the disk pattern will be much weaker than that of the central ellipse. The predicted pattern for spheres at this refractive index is the exact reverse, with the central ellipse much weaker than the upper lobes (see Fig. 16). Such a reversal in the character of the intensity distribution would be experimentally observable. For example, direct observation of the intensity distribution in the experimental pattern at $\bar{n} = 1.5291$ in Figure 16 shows conclusively that the source of that V_v SALS pattern was an anisotropic sphere and not an anisotropic disk.

As the refractive index of the medium continues to increase from 1.5291 to the average refractive index of the disk (1.530), the intensity of the central ellipse steadily decreases. By the time the medium refractive index equals 1.5308 (see Fig. 19) the central ellipse of the disk V_v SALS pattern

EXPERIMENTAL   THEORETICAL

$\bar{n} = 1.5319$

$\bar{n} = 1.5327$
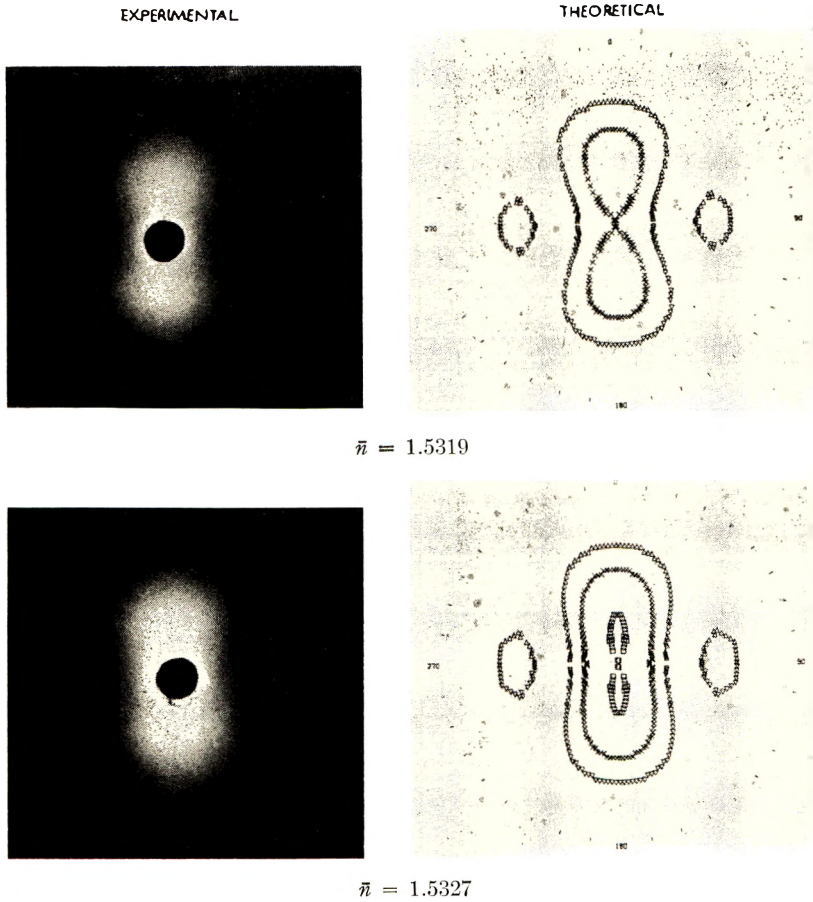
Fig. 17 (continued)

shows a decided pinch as it prepares to split into two lobes. The central pinched ellipse has weakened in intensity at this refractive index, but it is still stronger in intensity (through only slightly) than the intensity of the upper lobes. It should be noted that the central ellipse of the theoretical sphere pattern has already split into two lobes in a medium of refractive index 1.5298 (see Fig. 16), and the upper lobes have much higher intensity than the equatorial central-ellipse lobes of the pattern. With a medium of refractive index 1.5308 the more intense upper lobes of the anisotropic-sphere V_V SALS pattern have moved together until they almost touch vertically, and the weak, horizontal side-lobes have effectively disappeared, in sharp contrast to the character of the predicted disk pattern at this refractive index.

As the refractive index of the medium increases from the average refractive index of the disk (1.530) toward the radial refractive index of the disk (1.537), intensity differences are again discernible between the disk and
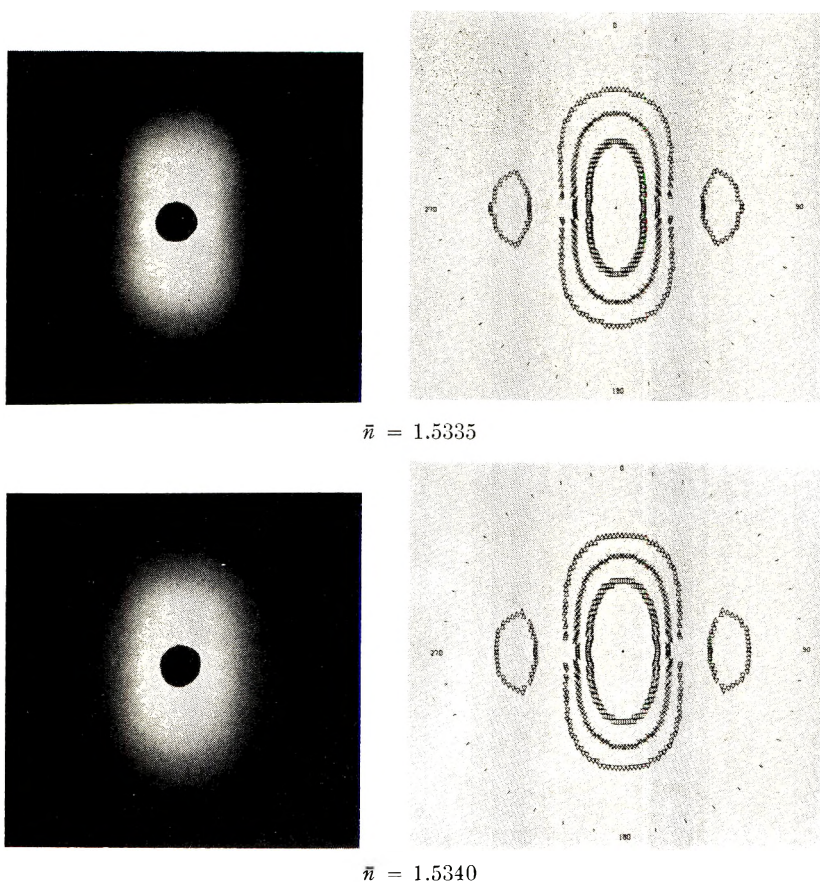
$\bar{n} = 1.5335$

$\bar{n} = 1.5340$

Fig. 17. Comparison of the experimentally observed V_v SALS patterns from rice starch granules with those predicted theoretically under the same optical conditions. The average refractive index of the background is listed under each set of V_v SALS patterns.

sphere scattering patterns. For a medium of refractive index 1.5319, the disk V_V SALS pattern in Figure 19 splits into four lobes. The equatorial lobes have slightly higher intensity and are slightly larger than the meridian outer lobes. This disk pattern is still different from the pattern behavior predicted for anisotropic spheres at this refractive index (Fig. 17). As the refractive index of the medium continues to increase, however, the meridian outer lobes merge and increase in intensity with respect to the horizontal lobes, so that for a medium of refractive index 1.5340, a vertical ellipse has formed of considerably higher intensity than the equatorial lobes. In fact, at a refractive index of 1.5340, it would again be experimentally difficult to distinguish the V_V SALS pattern produced by an anisotropic starch sphere from that produced by an anisotropic starch disk.

This comparison of the theoretically predicted anisotropic disk V_V SALS patterns, with those predicted and experimentally observed from aniso-

$\overline{n} = 1.5193$ $\overline{n} = 1.5234$

$\overline{n} = 1.5261$ $\overline{n} = 1.5272$

$\overline{n} = 1.5285$ $\overline{n} = 1.5291$
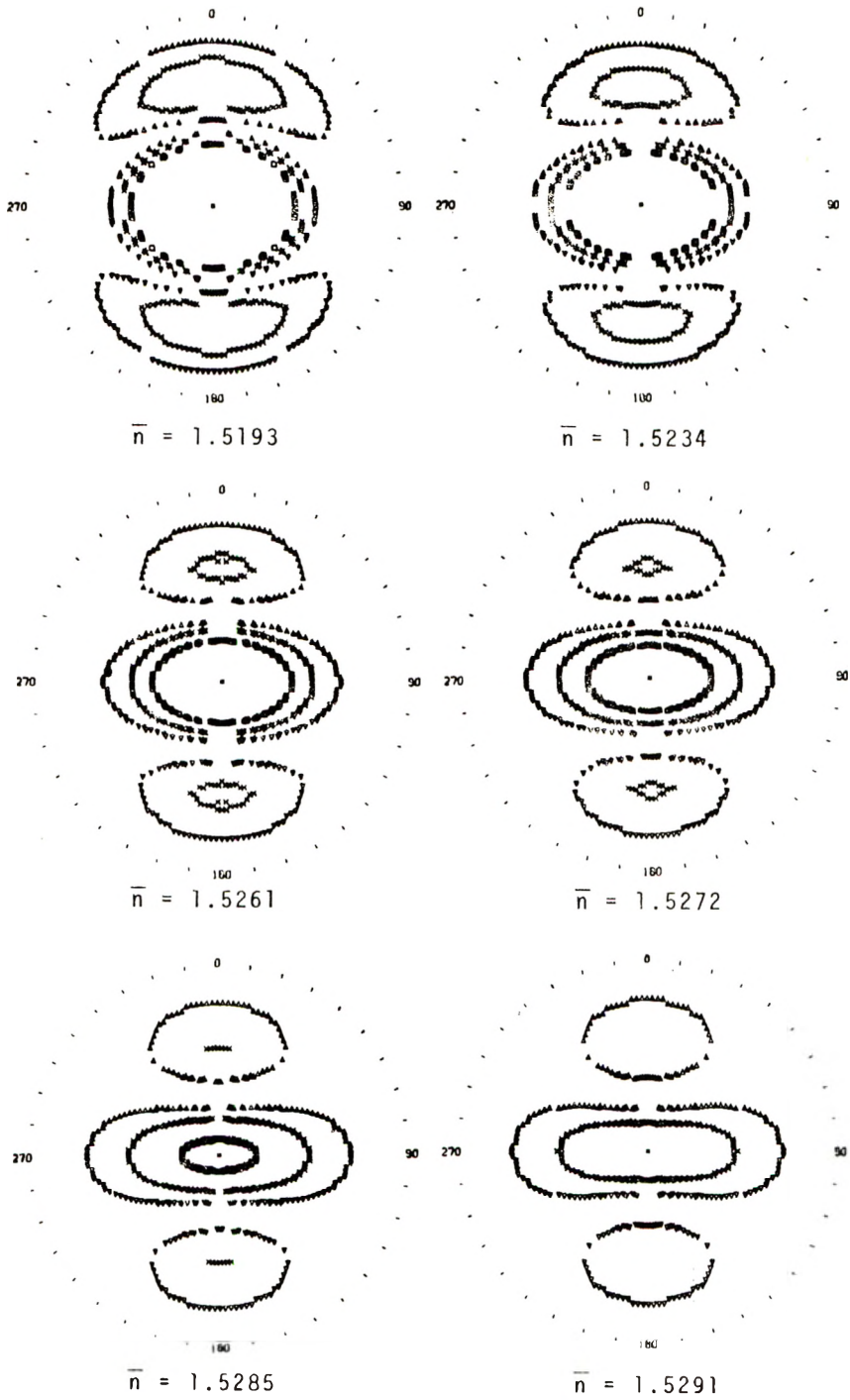
Fig. 18. Theoretical V_v SALS patterns for anisotropic disks using the same optical
parameters as for the rice starch granules.
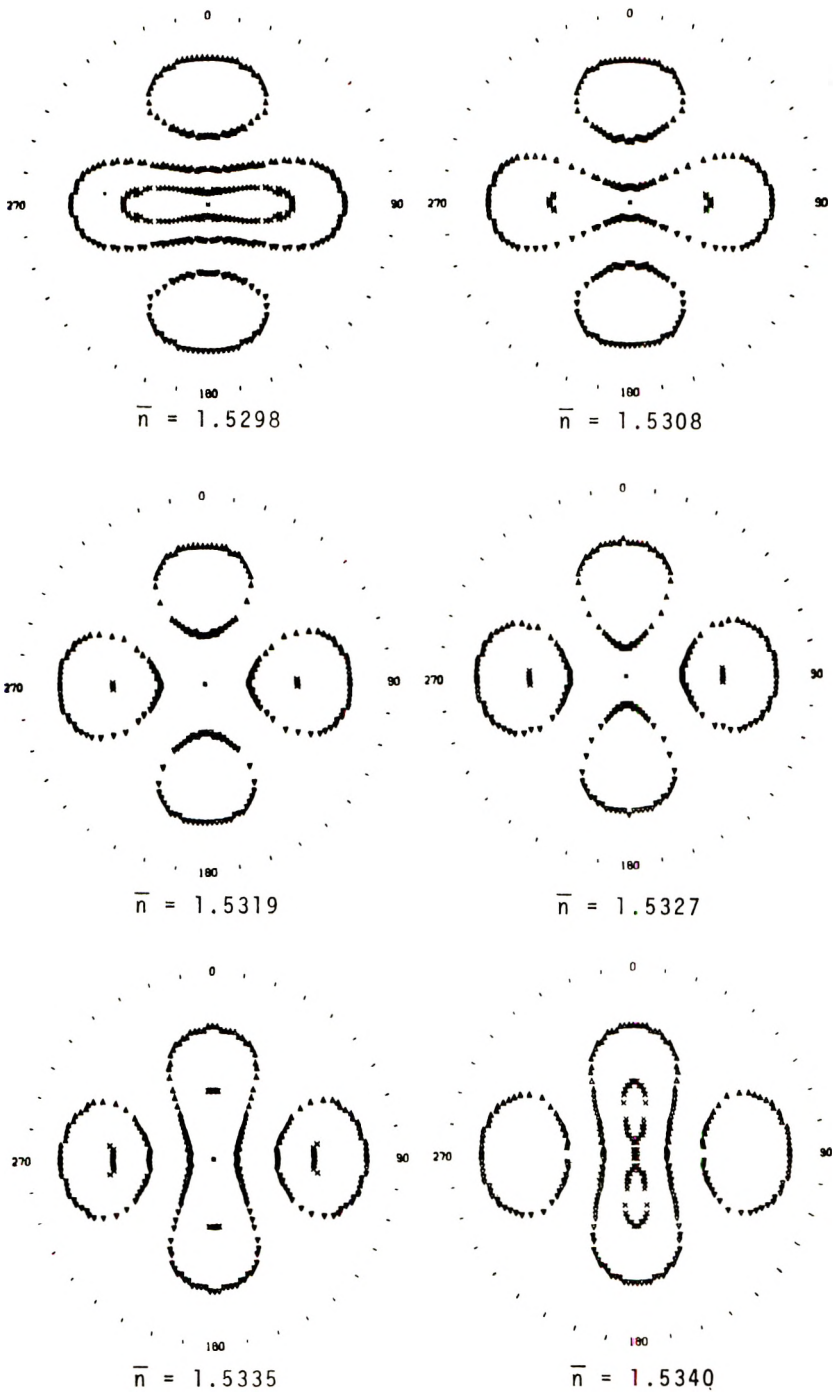
Fig. 19. Theoretical V_v SALS patterns for anisotropic disks using the same optical parameters as for the rice starch granules.

tropic starch spheres under the same optical conditions, illustrates some significant relations between these systems. Thus, it is now obvious that the general shape of the V_V SALS scattering patterns produced from the same optical environment by anisotropic spheres and anisotropic disks are similar. The source of the V_V SALS scattering pattern can be identified as either an anisotropic sphere or an anisotropic disk, provided the intensity distribution is examined on V_V SALS patterns that have been obtained under the special condition that the surrounding media have refractive indices in the region between the radial and tangential refractive index values of the anisotropic body under investigation. The observed V_V SALS patterns obtained from starch spherulites agree with those theoretically predicted for spheres and disagree with those theoretically predicted for disks of the same optical composition.

It is important to note here that the above analysis of V_V SALS patterns does not exclude the possibility that spherulites with a fixed birefringence might be found in a background environment which is anisotropic. To treat this case theoretically, eq. (1) must be so modified that the term $(\alpha_r - \alpha_s)$ has the form $(\alpha_r - \alpha_{s,r})$, and the term $(\alpha_t - \alpha_s)$ has the form $(\alpha_t - \alpha_{s,t})$. Here $\alpha_{s,r}$ and $\alpha_{s,t}$ denote the polarizability of the surroundings in the radial and tangential directions, respectively. The same theoretical patterns that were produced for the spheres and disks by an isotropic background of changing refractive index can now be produced for spheres and disks by changing the background refractive index in each direction from that of the spherulite in the same direction. All refractive indices must have the same positive absolute sign, however, for the patterns to be equivalent to the isotropic case when eq. (1) is used, and the magnitude of the anisotropy of the background should not exceed that of the spherulites. If background anisotropy does occur this is the only physically reasonable model for such an anisotropic system. The earlier form of the V_V SALS equation did not predict this, and its failure generated the present study. A catalog of the V_V SALS patterns predicted by the correct form of the sphere and disk equations with variation in the absolute sign and magnitude of an anisotropic background is given in Appendix II.

Isotactic Polystyrene. The fact that the general shape of the V_V SAL patterns predicted for spheres and disks are similar is very important practically; for expectations that they differ can create severe problems in the interpretation of experimental results. The dilemma that developed from a study of the small-angle light scattering from isotactic polystyrene spherulites[18] illustrates this point. The investigators chose isotactic polystyrene for study since it has a low crystallization rate and a large spherulite anisotropy. This allowed them to grow, in a film 20 μ thick, isolated spherulites with an average 10 μ diameter surrounded by amorphous isotactic polystyrene. The purpose of the study was to change the refractive index of the spherulite environment by swelling it with liquids of various refractive indices and to compare the resulting experimental V_V SALS patterns with those predicted by sphere and disk theory. Four refractive
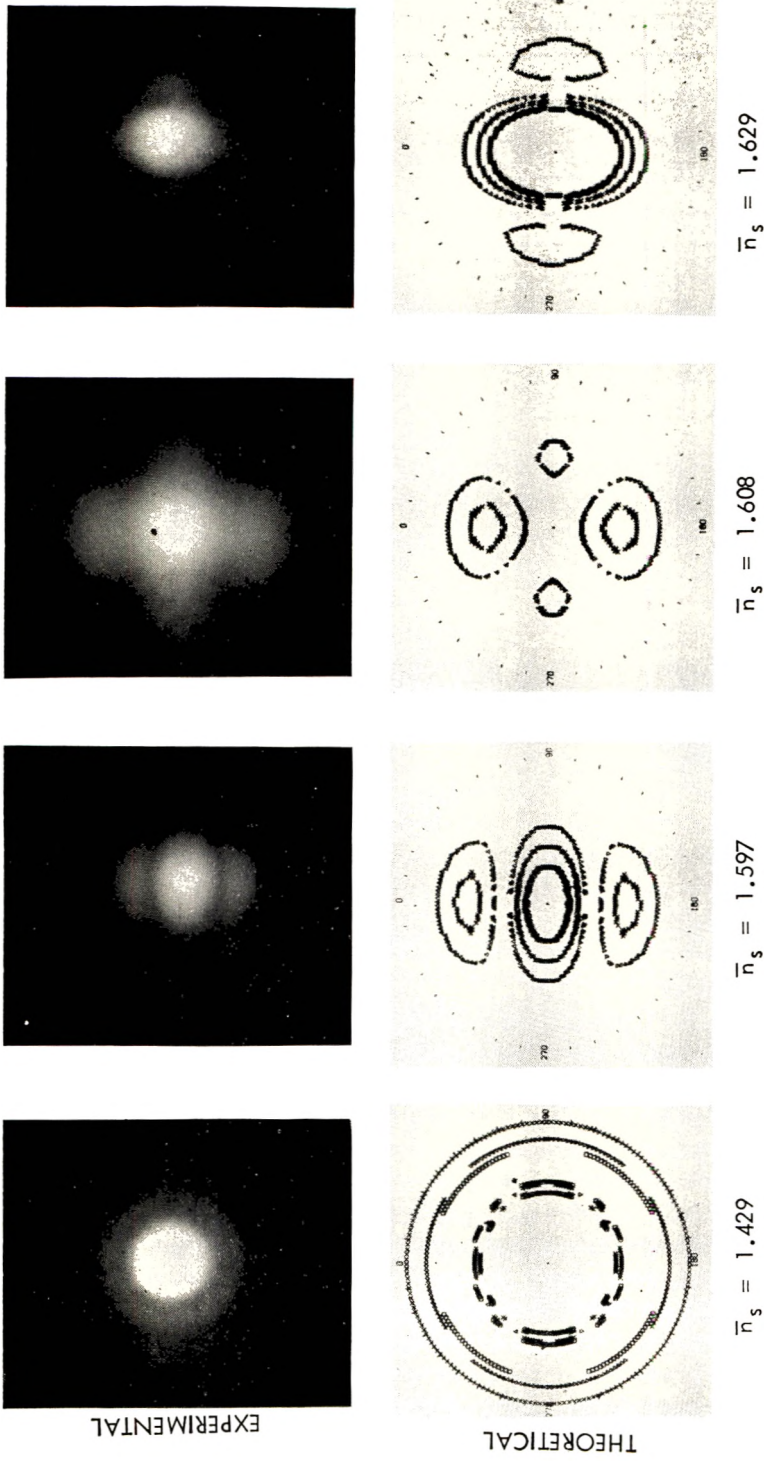
Fig. 20. Comparison of the experimentally observed V_v SALS patterns from isotactic polystyrene with those theoretically predicted for anisotropic spheres under the same optical conditions.
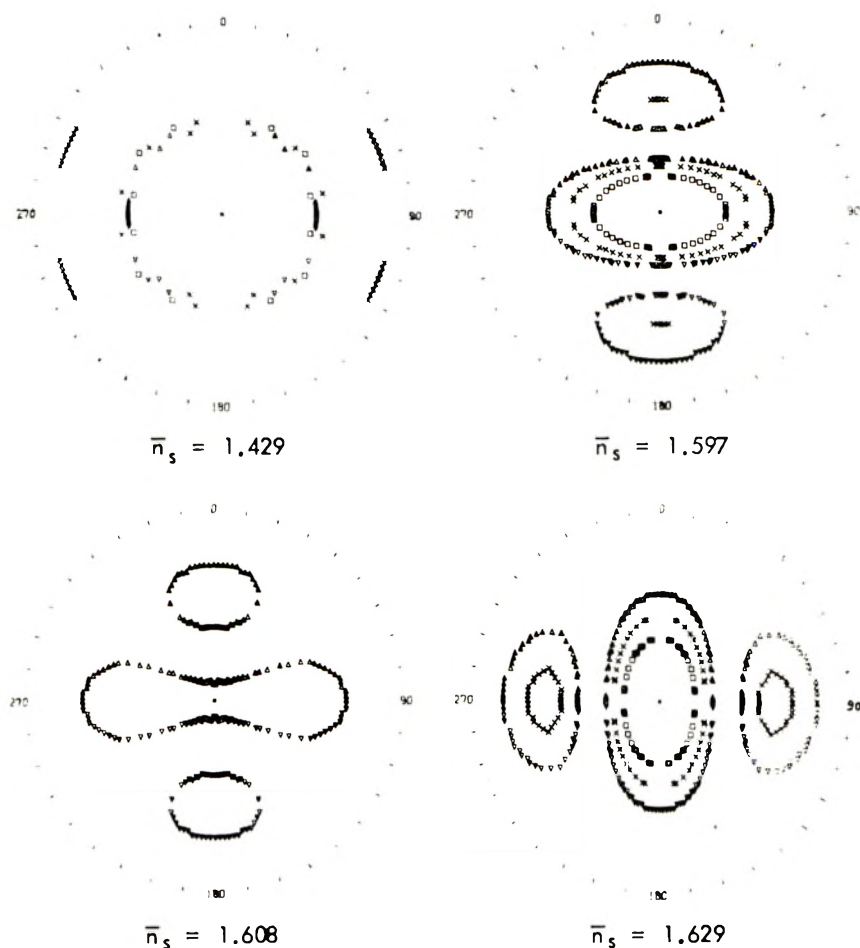
Fig. 21. Theoretical V_r SALS patterns for anisotropic disks with the same optical para-
meters as for the isotactic polystyrene spherulites.

indices were chosen for study of the scattering envelopes from the positively
birefringent isotactic polystyrene spherulites. These were (1) $\bar{n}_s = 1.429$,
a background refractive index much lower than the spherulite refractive
indices; (2) $\bar{n}_s = 1.597$, a background refractive index equal to the tan-
gential refractive index of the spherulite; (3) $\bar{n}_s = 1.608$, a background re-
fractive index equal to the average refractive index of the spherulite; and
(4) $\bar{n}_s = 1.629$, a background refractive index equal to the radial refractive
index of the spherulite. The experimental V_V SALS patterns that were
obtained under these background conditions are shown in Figure 20.
Comparison of the experimental patterns with those predicted by existing
small-angle light scattering theory[1,22,23] showed excellent agreement of the
experimental patterns with disk theory and complete disagreement with
sphere theory. The investigators were thus forced to conclude that, since

"the diameters of the spherulites studied were less than the film thickness, it is necessary to assume either that the disk shape or a stack of disks is the normal shape of isotactic polystyrene spherulites, or that crystallization is preferentially initiated at the surface of the glass plate."

This dilemma would not have occurred if the correct V_V SALS equation for anisotropic spheres had been available. The V_V SALS patterns predicted by disk theory for the same optical characteristics of the isotactic polystyrene spherulites used experimentally, are plotted in Figure 21. These theoretically predicted disk scattering patterns are indeed very similar to those experimentally observed (Fig. 20). The V_V SALS patterns theoretically predicted for these same isotactic polystyrene spherulites by the anisotropic-sphere theory according to eq. (1), are shown directly under the equivalent experimental patterns in Figure 20. The theoretically predicted correct anisotropic sphere patterns also agree with those obtained experimentally. In fact, because of overexposure from the main beam in the central region of the experimental V_V SALS patterns, it is difficult to distinguish whether the observed scattering is from spheres or disks. The small diameter of the spherulites with respect to the film thickness certainly suggests spherulites and not disks were the source of the scattering patterns and this seems to be supported by the weaker character of the side lobes in the experimental pattern at $\bar{n}_s = 1.608$. This conclusion could be proved by examination of further V_V SALS patterns that are obtained using other background refractive indices whose values fall between the tangential and radial refractive indices of the spherulite.

Since the two-dimensional disk theory examined here[22,24] assumes that the plane of the disk is parallel to the plane of the film, and it is under this restriction that the above conditions prevail, another experimental technique which might be used to identify the scatterers shape is to observe the effect of tilting the polymer film on the V_V SALS pattern. For disk scattering one would expect the scattering pattern to change with tilt angle, whereas with sphere scattering there should be no change (except for that produced by refraction).

A third method that could be used for identification of the scatterer shape would be extraction of the scatterers from the polymer film by dissolving away the noncrystalline polymer. This technique has been used by Stein[25] to obtain separate structures from isotactic polystyrene films. The separated structures were observed to be spherulites and not disks, in agreement with the above analysis of isotactic polystyrene film scattering.

Condensed Systems

Starch: Effect of Concentration on the V_V SALS Patterns

The foregoing study was undertaken in order to examine the validity of the small-angle light-scattering equations under controlled, quantitatively measurable environments. One aspect of that environmental control was

minimization of the concentration of spherulites in order to eliminate any effects that might be produced by interparticle interference, multiple scattering, internal strain, and anisotropic background. Now that the validity of the theoretical V_V SALS equations has been verified experimentally, it becomes practical to consider how severely spherulite proximity affects the observed V_V SALS pattern.

The absolute intensity of scattering is certainly dependent on the concentration of scattering centers. This is strikingly demonstrated in Figure 14. At low concentrations of scattering centers the intensity is proportional to the number of independent scatterers. When the concentration of spheres increases beyond some maximum value, interparticle interference and multiple scattering effects brought on by the close proximity of the spheres diminish the effect of each independent scatterer on the intensity of the total system. When this happens, the rate of increase of the intensity is observed to decrease with increasing concentration. The question that must be asked here is whether the character of the V_V SALS pattern also changes as the concentration of spherulites increases, or is it only the overall intensity that is affected? If the different regions of the V_V SALS pattern are influenced identically by interparticle effects, then the observed V_V SALS pattern will be the same at low and high concentrations of spherulites. This would mean that polymer films, in which the spherulites are space-filling, can be evaluated quantitatively from the V_V SALS equations.

Starch samples were prepared at the highest concentration shown on Figure 14 (46% by volume of starch, 51% by weight of starch) in media of several different refractive indices. The average refractive index of each system was then calculated from the measured refractive index of the immersion medium and the known average refractive index of the starch granules by using the Gladstone-Dale relation. This calculation corrected refractive index of the medium for the increased contribution of the higher concentration of starch spherulites. The V_V SALS patterns from these concentrated starch systems were then experimentally measured and compared with the V_V SALS patterns theoretically predicted by eq. (1) under identical optical conditions. The experimental and theoretical V_V SALS patterns obtained from the concentrated starch systems are shown in Figures 22–24.

The agreement between the experimentally determined V_V SALS patterns and the V_V SALS patterns predicted for the concentrated starch systems by eq. (1) is excellent. In fact, it looks as though the improved resolution of the experimental V_V SALS patterns, as a consequence of their higher scattering intensity, has resulted in at least as good and possibily better correspondence between theory and experiment than had been observed with the more dilute systems. Certainly there is no indication that concentrating the system until 46% of the volume is composed of spherulites has in any way interfered with the predictive value of the SALS equations.

An attempt was made to prepare films completely composed of starch spherulites. Such films would be comparable to films of synthetic polymers in which the spherulites are space-filling. Starch spherulites are quite

EXPERIMENTAL

THEORETICAL

$\bar{n} = 1.5232$

$\bar{n} = 1.5263$

$\bar{n} = 1.5276$
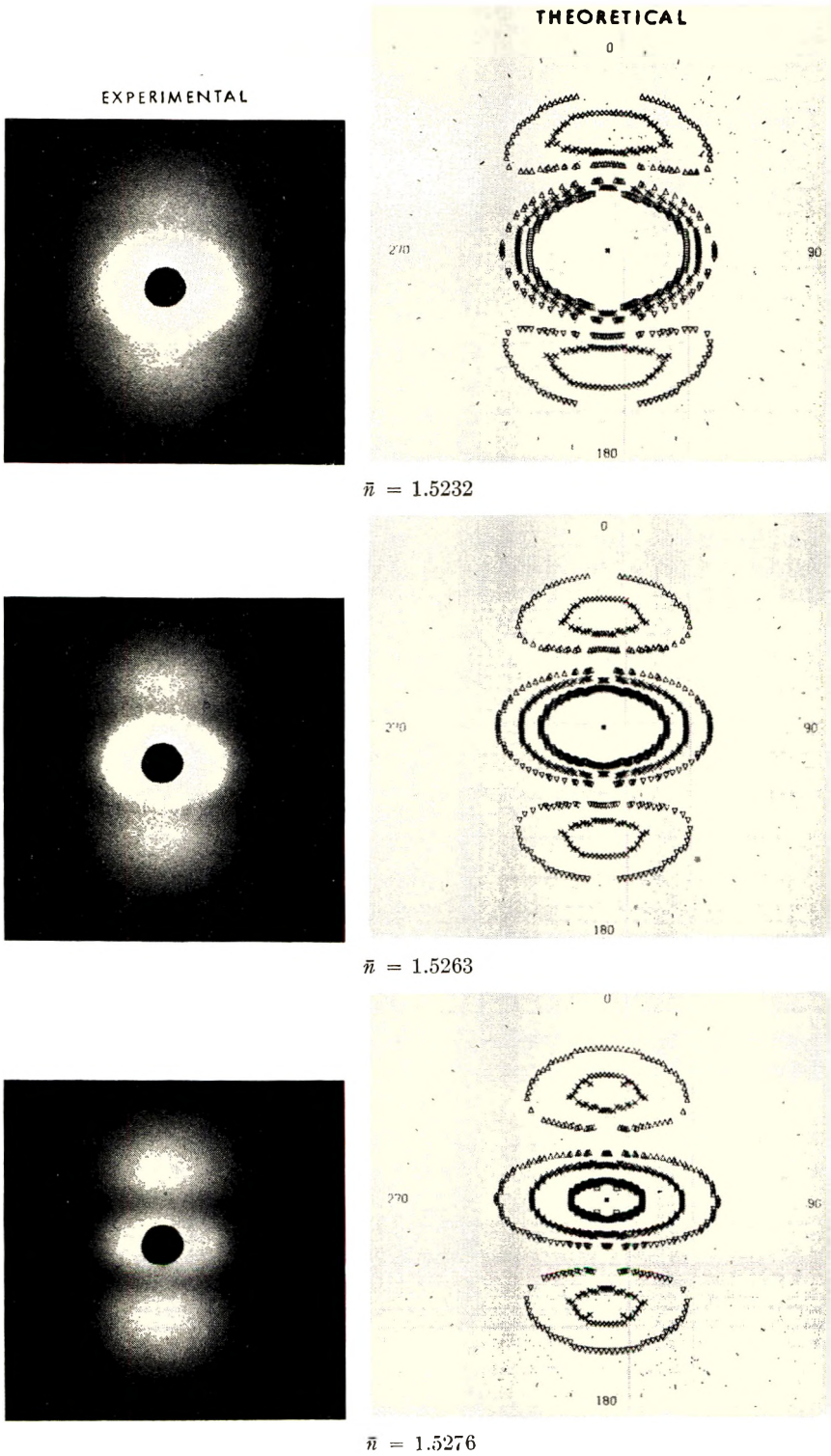
Fig. 22. Effect of high starch concentration on the measured and theoretically predicted V_v SALS patterns. The average background refractive index is listed under each set of V_v SALS patterns.

EXPERIMENTAL
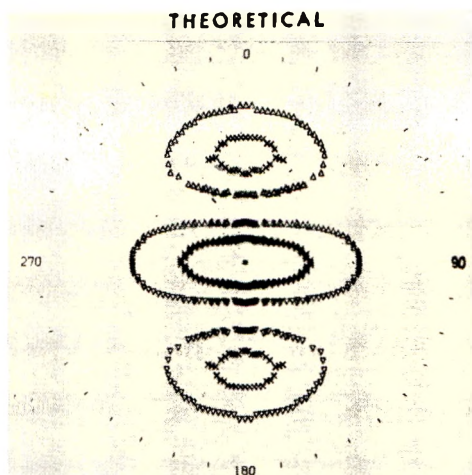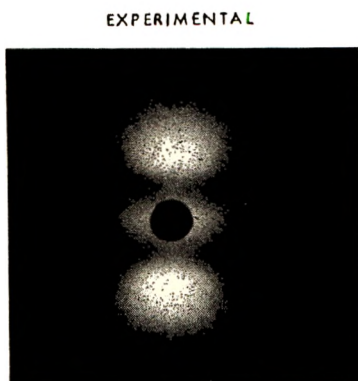
$\bar{n} = 1.5284$
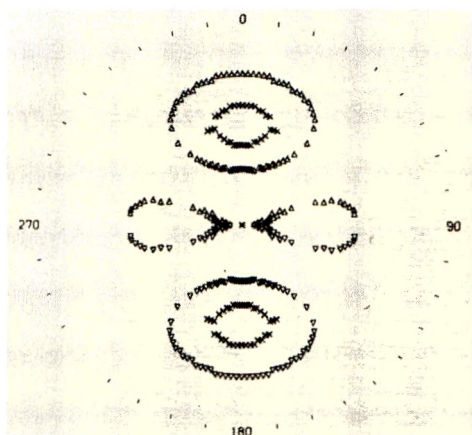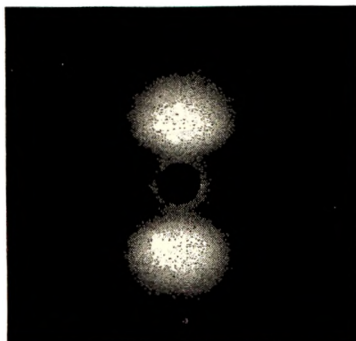
$\bar{n} = 1.5296$
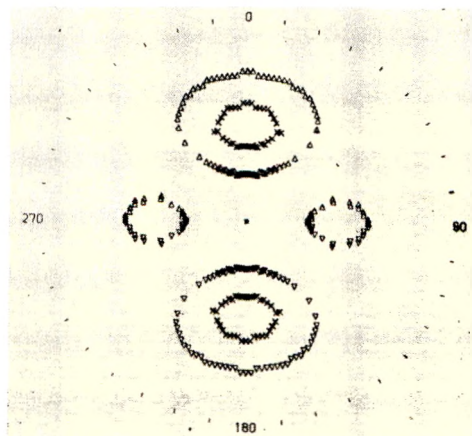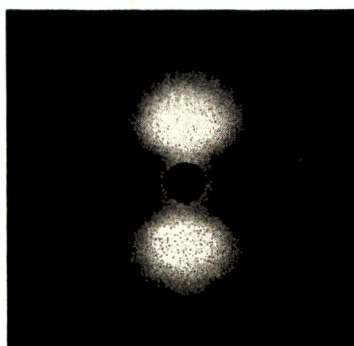
$\bar{n} = 1.5301$

Fig. 23. Effect of high starch concentration on the measured and theoretically predicted V_v SALS patterns. The average background refractive index is listed under each set of V_v SALS patterns.

EXPERIMENTAL

THEORETICAL

$\bar{n} = 1.5314$

$\bar{n} = 1.5325$

$\bar{n} = 1.5328$

Fig. 24. Effect of high starch concentration on the measured and theoretically predicted V_v SALS patterns. The average background refractive index is listed under each set of V_v SALS patterns.

$\bar{n}_s = 1.50240$

$\bar{n}_s = 1.51706$

$\bar{n}_s = 1.52525$

$\bar{n}_s = 1.52884$

$\bar{n}_s = 1.53261$

$\bar{n}_s = 1.53409$
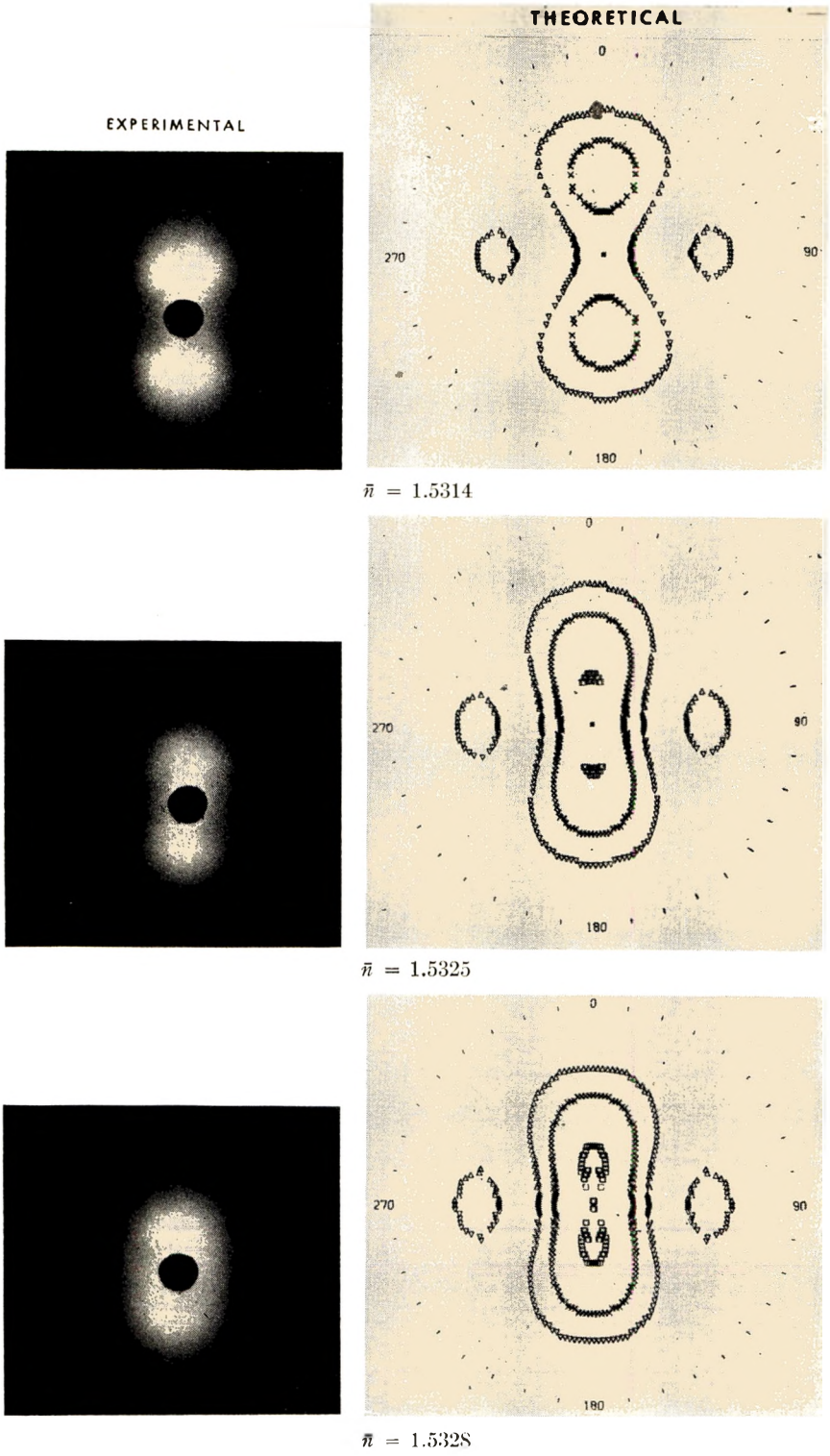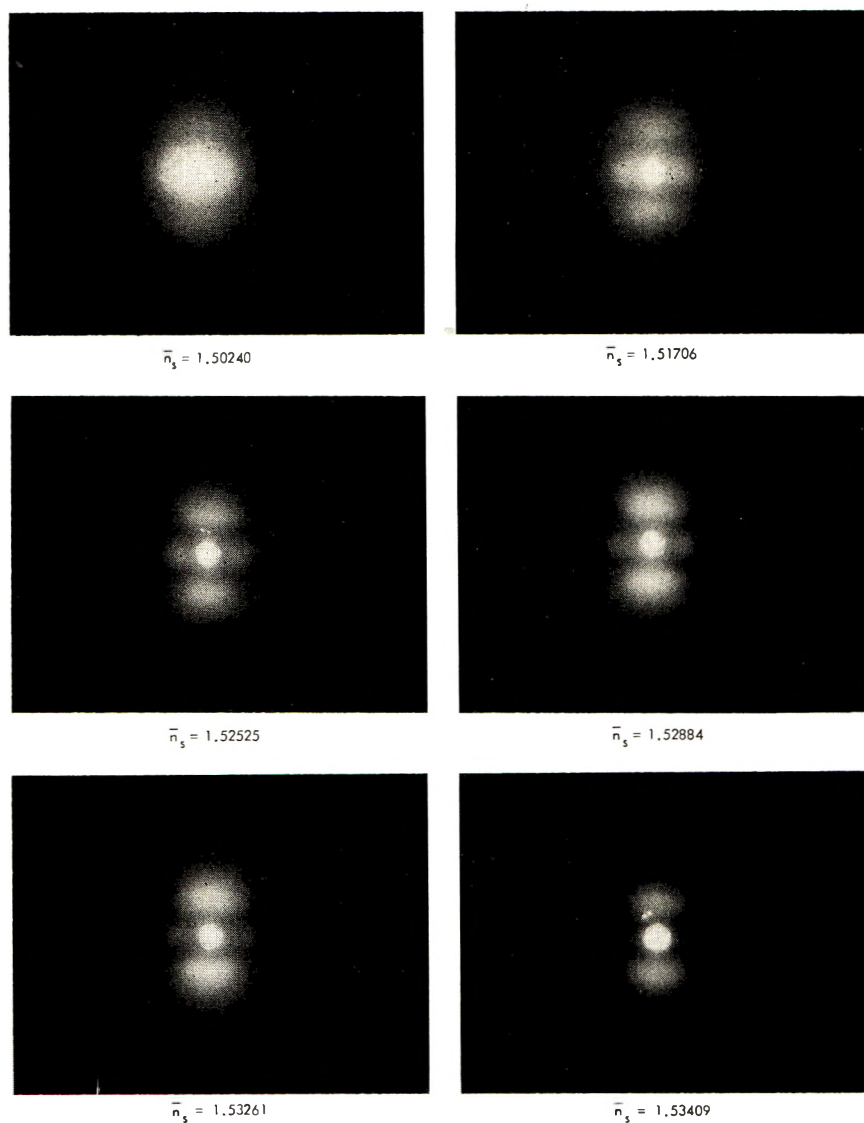
Fig. 25. V_v SALS patterns from starch films. The refractive index of the immersion oil is listed under each V_v SALS pattern.

strong and resilient. Brittle, opaque films could be produced only by sub-jecting 300 mg of rice starch to high pressure (85 ton/in.³) for 3–5 min. The resulting films averaged 3 mils in thickness, and the spherulites did not appear to be damaged. When silicone oil was placed on the surface of these opaque films, they became clear. Whether this was due solely to elimina-tion of surface scattering or to penetration of the film by the oil was not completely resolved. Silicone oils of high and low refractive index and

mixtures of these, were placed on the surface of the films in order to get V_V SALS patterns. The V_V SALS patterns obtained from the films are shown in Figure 25. The character of the patterns indicates that in most cases some oil penetration must have occurred as the patterns show shape and intensity changes characteristic of differences in background refractive index. The amount and character of the penetration (i.e., whether one or both components of the mixture medium penetrated the film) are not known. Certainly, quantitative interpretation of these V_V SALS patterns cannot be attempted.

It is informative to examine qualitatively how these patterns are changed. The symbol $\bar{n}_s$ in Figure 25 represents the refractive index of the immersion medium before it was applied to the film. Even if only a small amount of the immersion medium penetrates the film, it will change the average refractive index of the spherulite background. The greater the difference between the refractive index of the immersion medium and the spherulite, the greater will be its effect on changing that background. Thus, as we examine the character of the V_V SALS patterns in Figure 25, we see the same trend in the changes in the pattern with change in refractive index, as observed earlier; however, the patterns observed do not correspond quantitatively to those which would be expected if the listed refractive index of the immersion medium were the true background refractive index. If we therefore ignore the absolute value of the refractive index of the immersion medium, and look at the patterns as being produced only by background refractive indices that follow an increasing trend from some initial low value, we find that the patterns themselves resemble the V_V SALS patterns already observed from the low and high concentration starch systems. That is to say, there is nothing unusual about either the shape or intensity distribution of these V_V SALS patterns to indicate that interference effects from the intimate proximity of the spherulites in the film have changed the character of the scattering significantly. At the lowest refractive index, the central-ellipse intensity is greater than that of the outer lobes. As the refractive index increases, both the size of the central ellipses and its intensity relative to the outer lobes decreases. As the immersion medium refractive index continues to increase to higher values, the intensity of the outer lobes becomes greater than that of the central ellipse, until finally the ellipse disappears and only the outer lobes remain. All these observations are consistent with the changes in the V_V SALS pattern that were observed from both the dilute and concentrated starch systems with increasing refractive index. This supports the conclusion that the increasing proximity of spherulites does not significantly affect the anisotropic character of the V_V SALS pattern but only affects the overall absolute intensity.

It should be noted that recent theoretical studies[26] of the effect of spherulite concentration on interparticle interference suggest that for certain ranges of sphere size and concentration there will be a dependence of intensity on the radial angle θ. These theoretically predicted effects are not observed experimentally in the present study.

Isotactic Polypropylene

Effect of Optical Sign. The present study has demonstrated that the SALS theory is valid for both dilute and concentrated starch systems and correctly predicts the observed scattering from films containing isotactic polystytene spherulites. A feature of the theory that has not been tested, because both starch and isotactic polystyrene have positively birefringent spherulites, is the effect of the optical sign of the spherulite birefringence on the V_V SALS pattern. Theory predicts (see Appendix I) that the V_V SALS patterns from spherulites with opposite optical signs will have the same general features, but that the change in shape of the patterns with respect to changing background refractive index will be in opposite directions for spherulites of opposite sign. Negatively birefringent spherulites with changing background refractive index are required to test this aspect of the theory.

A 10-mil film of isotactic polypropylene is composed of space-filling negatively birefringent spherulites approximately 7 μ in diameter when it is prepared by room temperature quenching from the melt. The spherulites remain negatively birefringent and keep their size as the film is heated all the way to the melting point. Since it has already been shown that the V_V SALS patterns from condensed phases of spherulites resemble those from dilute systems, the isotactic-polypropylene negative spherulite system may be used to study the effect of the optical sign on the behavior of the V_V SALS pattern.

The average refractive index of a film depends on the relative amount of crystalline and noncrystalline polymer present. The greater the crystallinity (or density) the greater will be the average refractive index. Films quenched at room temperature were heated in an oven for ten minutes at different temperatures. The density, average refractive index, and V_V SALS pattern were then obtained from each film at room temperature. The relation between the annealing temperature and the average refractive index of the film is shown in Figure 26. As expected, the higher the annealing temperature the higher was the measured refractive index of the film. The increase in refractive index is due to an increase in the crystallinity (density) of the film. The relation between density and average refractive index of the annealed films is shown in Figure 27. The solid line in the figure is the relation predicted by Schael[27] for isotactic polypropylene.

The V_V SALS patterns obtained from these films are shown in Figure 28. Under each pattern are the measured average refractive index of the film $\bar{n}$, and the annealing temperature of the film (in parentheses). The change in the V_V SALS patterns from the negatively birefringent spherulites as the average background refractive index increases is clearly evident. The V_V SALS pattern changes from one having an intense vertical ellipse with no horizontal side lobes at a low background refractive index, to one where the vertical ellipse has split into two vertical lobes and the side lobes have appeared and increased in intensity at high background refractive index.

The shapes of the V_v SALS patterns are the same as those obtained from starch and isotactic polystyrene spherulites, but the direction of change of the V_v SALS patterns with changing background refractive index is opposite to that observed for the positive spherulites of starch and poly-
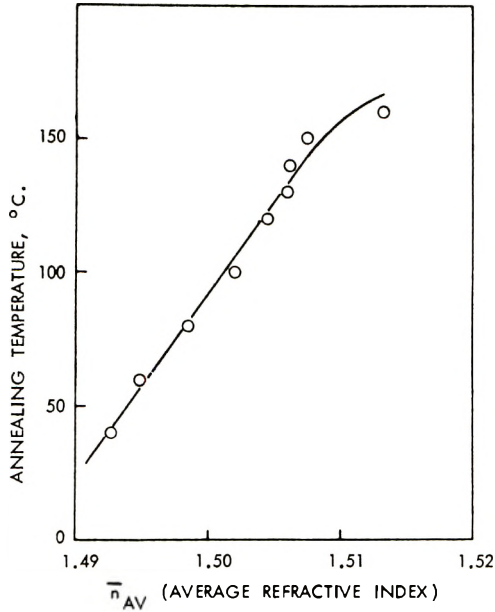
Fig. 26. Relation between the annealing temperature (for 10 min) and the average refractive index of cast isotactic polypropylene film.
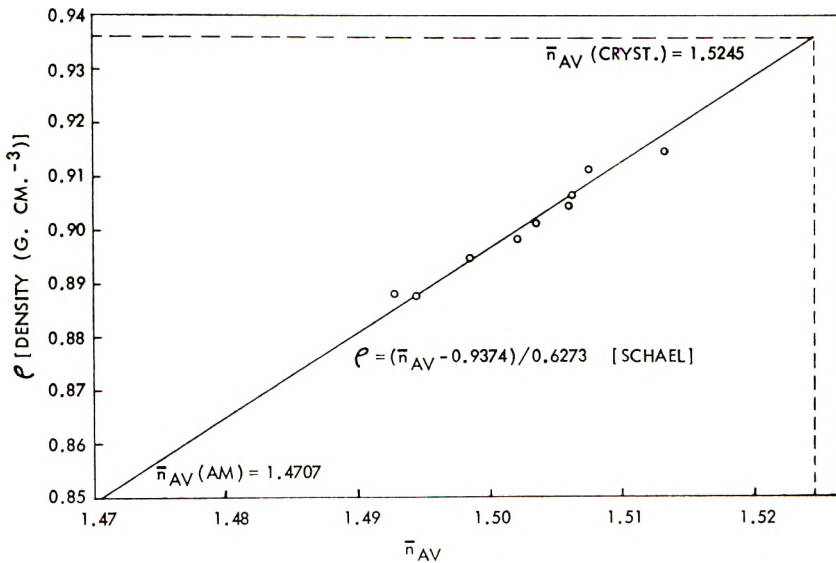
Fig. 27. Relation between the density of annealed, cast, isotactic polypropylene films and their average refractive index.
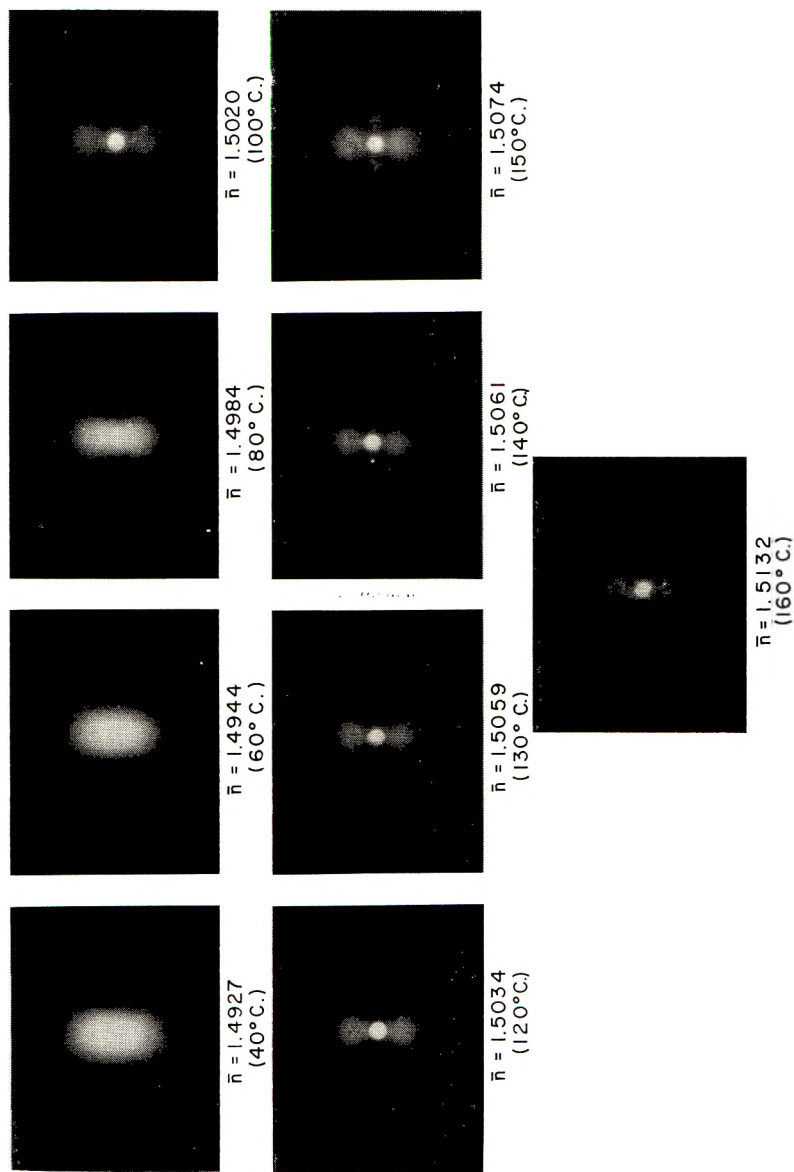
Fig. 28. V_v SALS patterns from annealed, cast, isotactic polypropylene films. The average film refractive index and the annealing temperature (in parenthesis) are listed under each V_v SALS pattern.

styrene. For positive spherulites the theory predicts an intense vertical lobe at high background refractive index (see Fig. 17), while it predicts the same pattern will appear at low background refractive index if negative spherulites are present (Fig. 28). Again, the theory predicts that two vertical lobes with weaker side lobes will be present in the V_V SALS pattern at low background refractive index for positive spherulites (Fig. 16) and at high background refractive index for negative spherulites (Fig. 28). Clearly, the observations correspond exactly to that predicted by the SALS theory (Appendix I).

High-Temperature Measurements. Some of the crystallization in the annealed samples examined above must have occurred after the isotactic polypropylene was removed from the oven and introduced to a room temperature environment. It is reasonable to consider how the difference between these environments will affect the character of the observed V_V SALS patterns. Certainly, at oven temperatures, the average refractive index of the film and the average crystallinity of the film will be different from the room temperature values. The crystal unit-cell dimensions and crystallite orientation may also change with temperature. It is even conceivable that crystallite orientation changes, or melting of crystals with preferred orientation, could lead to a change in the optical sign of the spherulite at elevated temperatures.

Polypropylene film was examined under oven conditions to see if any significant difference could be observed in the character of the observed V_V SALS patterns. A film containing an imbedded thermocouple was prepared by pressing the polymer between microscope cover glasses on a hot plate, with subsequent quenching with tap water. An H_V SALS pattern then taken of the film showed the polymer to be composed of negatively birefringent spherulites 7 μ in diameter. This preparative treatment was required in order to avoid the need for an immersion liquid, which could have adversely affected the polymer during heating. The film was then placed in a specially designed oven which had windows on opposite sides of the film surface, and which could be vertically mounted in the sample position of the SALS apparatus. The sample was heated to the lowest desired temperature (40°C), kept at that temperature for 10 min while a V_V SALS pattern was obtained, and then heating was continued to the next higher temperature. This process was repeated until the highest temperature that would yield a good V_V SALS pattern was reached (160°C). The resulting V_V SALS patterns, obtained while the samples were in the special oven at the temperatures listed, are shown in Figure 29. These oven produced V_V SALS patterns should be compared with the V_V SALS patterns obtained from samples that were annealed for 10 min at the same temperature (Fig. 28) and then brought to room temperature.

The character of both sets of V_V SALS patterns is very similar in spite of their different thermal histories. Certainly the change in shape and relative intensity of the lobes with increasing temperature is identical in both sets of patterns, showing that a reversible change in optical sign did
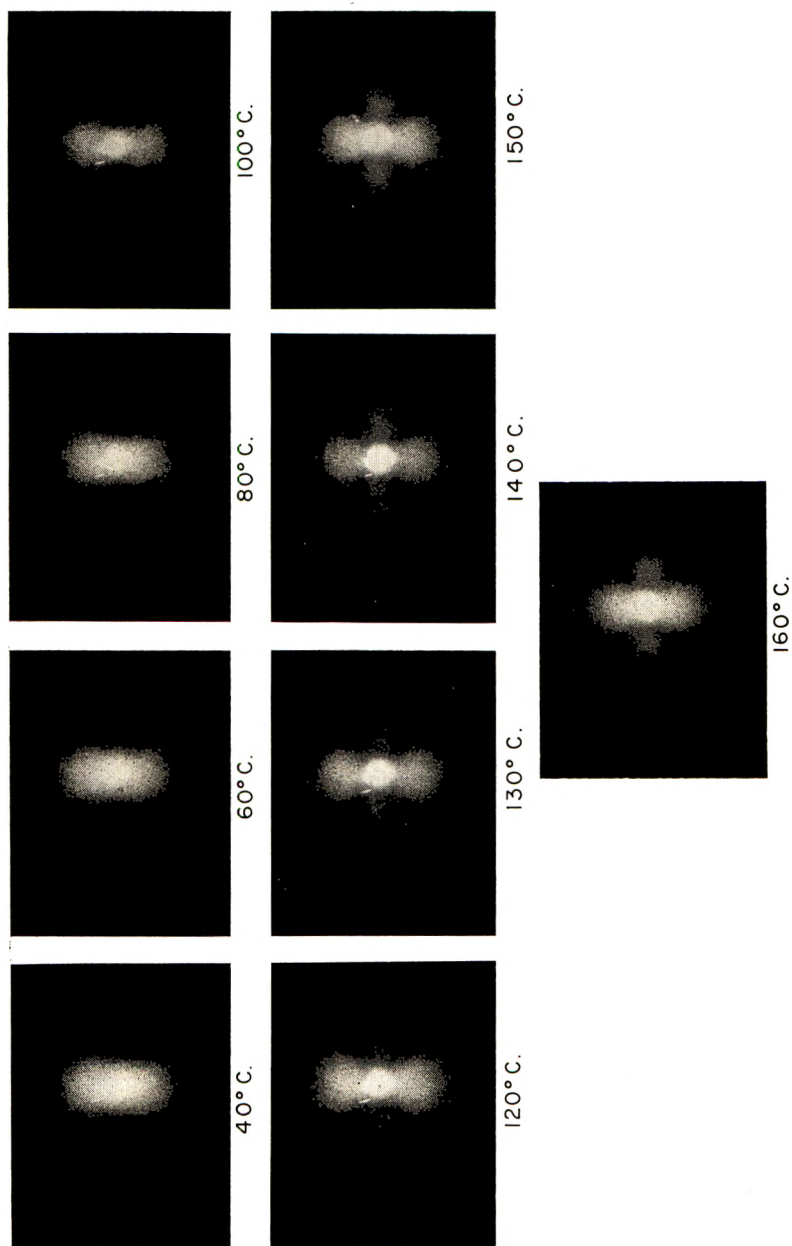
Fig. 29. V_v SALS patterns obtained at the annealing temperature listed from cast isotactic polypropylene films mounted in a special oven.

not occur at elevated temperatures. The close similarity of the two sets of V_V SALS patterns also suggests that the relative crystallinity level between the spherulites and the background is developed within the first 10 min of annealing, and that once developed, the relative difference remains fairly constant for some time. Also, at least for this study, subsequent cooling to room temperature did not seem to have a significant effect on the V_V SALS pattern, suggesting similar crystallization processes occur in both the spherulite and background during cooling to room temperature.

Determination of the Optical Sign of the Spherulite

A desirable application of the small-angle light-scattering technique would be the determination of the optical sign of spherulites that are too small to be identified in the optical microscope. Other techniques, such as electron microscopy, which are presently used to examine spherulites in this small-size range, are not capable of characterizing optical parameters. Thus SALS could become a unique tool in the growing arsenal of polymer characterization systems.

Theory predicts that the change in V_V SALS pattern with changing background refractive index will be in opposite directions for positive and negative spherulites. This was experimentally demonstrated with the negatively birefringent isotactic polypropylene spherulites (Fig. 28 and 29) and the positively birefringent starch and isotactic polystyrene spherulites (Figs. 15, 16, 17, and 20). Thus, if both positive isotactic polystyrene and negative isotactic polypropylene spherulites are prepared under conditions such that both have a low background refractive index with respect to their radial and tangential refractive indices, their optical sign could be easily identified from their V_V SALS patterns. For example, the V_V SALS pattern from positively birefringent spherulites of isotactic polystyrene when $\bar{n}_s = 1.597$ (low background refractive index) in Figure 20 is the opposite of that obtained from the negatively birefringent spherulitic sample of isotactic polypropylene annealed at 40°C (low background refractive index) in Figure 28.

However, SALS theory also predicts that under proper conditions the same V_V SALS pattern can be obtained from both positive and negative spherulites. This prediction is experimentally verified by the similarity between the V_V SALS patterns from negatively birefringent spherulites of poly(ethylene terephthalate) and positively birefringent spherulites of nylon 66 shown in Figure 12. The prediction is further verified by the similarity between many of the V_V SALS patterns obtained from negatively birefringent spherulites of isotactic polypropylene (Figs. 28 and 29) and positively birefringent spherulites of starch and isotactic polystyrene (Figs. 15, 16, 17, and 20). These observations show that, at least for different polymers, the optical sign of a spherulite cannot be identified simply by examining a single V_V SALS pattern since the method of preparation could lead to identical V_V SALS patterns from spherulites of oppoiste sign.

Does this same reasoning hold true for V_V SALS patterns from positive and negative spherulites grown from the same polymer? Such positive and negative spherulites usually must be prepared under very different environmental conditions. This leads to V_V SALS patterns from negative and positive spherulites of a given polymer that are generally quite different. Since the observed V_V SALS pattern is determined by the relative difference in refractive index between the spherulite and its background and not by the absolute refractive index values, it does not seem reasonable to assume that the observed form of the V_V SALS pattern from positive and negative spherulites of the same polymer will always be different. Certainly experimental conditions should be possible which can produce V_V SALS patterns that are the same.

Such a special situation can be demonstrated experimentally. Small positive spherulites of nylon 610 were prepared by quenching from the melt. A film of small negative spherulites was prepared by cooling from the melt to 190°C under pressure. The V_V SALS patterns from these film samples are shown in Figure 30 (25°C). The two V_V SALS patterns are quite different. The characteristic form of the V_V SALS pattern from the positive spherulites of nylon 610 shows that the background refractive index in this sample is lower than that of the spherulite (see for example, Fig. 15). The V_V SALS pattern obtained from the negative spherulites suggests that the spherulite and background refractive indices are about the same in this film, with the background region possibly having a slightly higher refractive index (see Fig. 28). Each of these films was heated for 10 min at increasing temperatures to increase the background refractive index. The changes that occurred in their V_V SALS patterns with heating are also shown in Figure 30. The observed changes with annealing of positively birefringent nylon 610 are the same as those observed with changing refractive index for starch and isotactic polystyrene spherulites (Figs. 15, 16, 17, and 20) and opposite to those observed from annealed negatively birefringent spherulites of isotactic polypropylene (Fig. 28). The negative spherulites of nylon 610 were grown at a high temperature (190°C), and therefore only a small difference appears on annealing. However, the observed direction of change in the patterns with annealing is opposite to that of the positive spherulites. The important features to observe from Figure 30 are (1) that V_V SALS patterns obtained by annealing the positive spherulites of nylon 610 are comparable to the V_V SALS patterns obtained from negative spherulites of the same polymer (compare positive at 125° with negative at 25°C and positive at 25° with negative at 150°C) and (2) that the direction of change with changing background refractive index predicted by theory (Appendix I) is again confirmed. Obviously then, simple examination of the V_V SALS pattern from a single sample cannot be considered a reliable method for determining the optical sign of the birefringence of the spherulites, since the same pattern may be obtained from both spherulite types.

POSITIVE SPHERULITES

25°C.   125°C.   164°C.   200°C.

NEGATIVE SPHERULITES

25°C.   100°C.   150°C.   207°C.
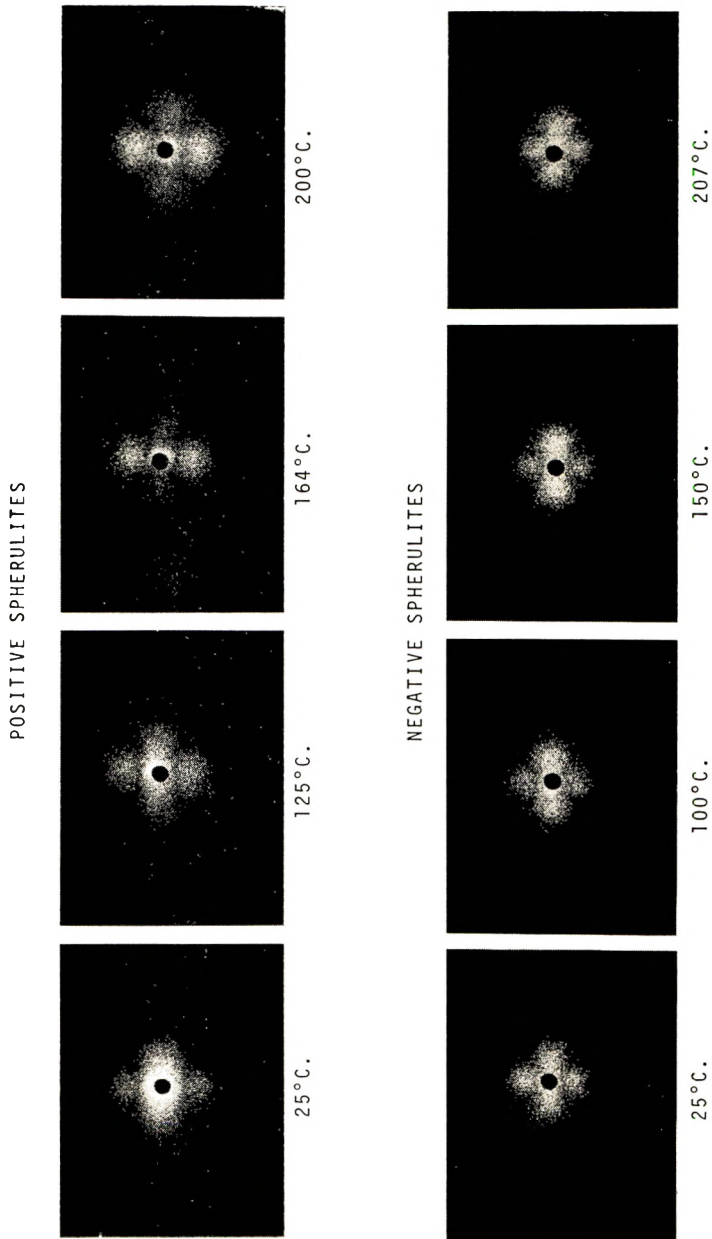
Fig. 30. V_v SALS patterns from as-prepared and annealed films of positive spherulitic and negative spherulitic films of nylon 610. The annealing temperature is listed under each V_v SALS pattern.

Since the direction of change of the V_V SALS pattern with changing background refractive index is decidedly different for negative and positive spherulites, this knowledge could be applied to the determination of the optical sign of the spherulites. Thus, it seems obvious from the observed direction of change of the V_V SALS patterns from isotactic polypropylene (Fig. 28) that these spherulites are negatively birefringent, and that the V_V SALS patterns from the positive spherulites of nylon 610 (Fig. 30) do arise from positively birefringent spherulites. This distinction is deceptive, however, and care must be taken in its use. If the spherulite refractive indices are fixed (as they were in the starch study) and the background refractive index increases, the direction of change of the V_V SALS pattern with increasing background refractive index will be in opposite directions for spherulites of opposite sign. In polymer films the refractive index of both the spherulites and the background is changing. When the refractive index of the background increases faster than that of both the positive and negative spherulites of a given polymer, the direction of change in the V_V SALS pattern can be used to identify the optical sign of the spherulites. If, however, the spherulite refractive index increases faster than the background refractive index, the direction of change of the V_V SALS patterns will reverse with increasing average refractive index even though the total average refractive index of the film is increasing.

Can this problem be resolved? The experimental data suggest a possible partial solution. In all cases examined to date the V_V SALS pattern from the initially prepared positive spherulite of a given polymer was quite different from that obtained from the initially prepared negative spherulites of the same polymer (Fig. 12). This is probably because the positive spherulite morphology is quite different from the negative spherulite morphology, and very specific and quite different conditions are required to produce each type. Thus, though it will not be universally true, it is probably likely that the V_V SALS patterns obtained from "as produced" positive and negative spherulites of the same polymer will be different. This does not mean that a single V_V SALS pattern will identify the optical sign, but it does suggest that in many cases such an approach may be practical. The type of experiment envisioned here would be (1) to prepare spherulites that are large enough for both the optical sign and the V_V SALS pattern to be determined, and (2) to compare the V_V SALS patterns obtained from the spherulites of known optical sign with those obtained from spherulites produced under closely similar conditions but which are too small to resolve in the optical microscope.

The experimental data from isotactic polypropylene and nylon 610 offer further encouragement. With these polymers both the optical sign and the V_V SALS patterns were obtained before and after annealing. Thus it was possible to observe the direction of change of the V_V SALS patterns, while at the same time ensuring there was no change in the optical sign. In all three experimental studies, annealing was observed to increase the refractive index of the background at a faster rate than that of the spherulites.

This suggests that once the spherulites have formed, the spherulite refractive index is more difficult to change than that of the background. This seems reasonable, since, thermodynamically, ordered structures are more stable than disordered ones. Thus it seems likely that, in general, annealing of preformed spherulitic structures will result in a more rapid refractive index increase in the background regions of the polymer than will be found spherulitically.

This suggests another step in the experimental verification of the sign of the birefringence of spherulites too small to be seen in the optical microscope. First, the spherulites which were large enough for the determination of both the optical sign and the V_V SALS pattern should be annealed at different temperatures, and both the optical sign and the V_V SALS pattern should be followed with temperature. In this way it will be possible to observe whether the more likely processes of a more rapid refractive index increase of the background over that of the spherulites occurs with this polymer. Once this has been confirmed, a sample which contains spherulites prepared under closely similar conditions but which are too small to be resolved in the optical microscope should be annealed at similar increasing temperatures. If the change in the V_V SALS pattern with annealing temperature of these spherulites follows the same sequence as did the larger spherulites of known optical sign, then the optical sign of the smaller spherulites can be considered confirmed.

CONCLUSIONS

Any new area of investigation will only progress rapidly toward general practical application if there is confidence in the correctness of the theoretical foundations. Though there has been growth over the past decade in the field of small-angle light scattering, this growth has concentrated principally on the practical application of H_V SALS scattering while the potentially more fruitful area of V_V SALS scattering theory has been largely neglected. The purpose of this study has been to examine the SALS theory in depth in order to locate any theoretical errors, and then to place the V_V SALS scattering behavior on a sound theoretical and experimental foundation.

The goals of this study have been achieved. An error was found in the original light-scattering theory.[1] This error had undergone a more recent unrecognized correction,[2] so that both the earlier incorrect and later correct form of the theory are in active use. This incongruous situation can, and should, now be corrected.

The SALS theory has been put to a definitive experimental test through a quantitative experimental examination of V_V SALS scattering from rice starch along with a complementary theoretical study of the observed patterns. The correct form of the theoretical V_V SALS equation has been identified and can now be considered experimentally verified as a consequence of this study.

Once the validity of the SALS theory was established, a more comprehensive examination of SALS behavior could be considered. The problem of most general practical interest was the application of the SALS theory to condensed systems. The SALS theory had originally been derived for a system of independent scatterers, but it has generally been applied to the analysis of polymer films and fibers. Is such an application of the theory reasonable? Examination of this question experimentally for rice starch and isotactic polystyrene spherulites has shown that, for the systems studied, spherulite proximity affects only the magnitude of the observed intensity and not the anisotropy of spherulite scattering. Thus the observed character of the V_V SALS patterns obtained from dilute and concentrated systems was identical.

At the present time it is generally believed that the V_V SALS patterns observed from spheres will be different in kind from those observed from disks under the same optical conditions.[22,23] Analysis of the correct form of the sphere and disk light scattering equations has shown this belief to be incorrect. Though differences do exist between the predicted V_V SALS patterns from disks and spheres, these differences appear only under specified conditions, and only as subtle intensity differences in otherwise similar patterns.

Another theoretical problem that has been examined in this study is the effect of the optical sign of the spherulite on the character of the V_V SALS behavior when the background refractive index changes. Theory predicts that the V_V SALS patterns obtained from a positively birefringent spherulite under changing background refractive index conditions will be the reverse of those observed from negatively birefringent spherulites under similar background refractive index conditions. This predicted reversal in scattering behavior has now been experimentally demonstrated by comparing the scattering patterns obtained from starch, isotactic polystyrene, isotactic polypropylene, and nylon 610 spherulites under changing background refractive index conditions.

Of more practical concern, an evaluation was made of the possibility of using SALS patterns to determine the optical sign of spherulites that are too small to be identified in the optical microscope. Both positive and negative spherulites of nylon 610 were used to illustrate different aspects of this important problem. The study has shown that the optical sign determination can be made, provided a specially outlined procedure is followed.

APPENDIX I

Small-Angle Light-Scattering (SALS) Theory

A spherulite is a three-dimensional, spherically symmetrical aggregate of crystalline and noncrystalline polymer. Thus, any theory which purports to describe SALS behavior of spherulites must use as its model the known three-dimensional structure of the spherulite as observed by light and electron microscopy. The amplitude method for calculating the

intensity envelope of scattered radiation is most useful for the theoretical small angle light scattering approach since it requires a model for its derivation. By choosing a model which realistically represents the known morphological characteristics of the spherulites, the observed SALS behavior from spherulites should be predictable.

Since the undeformed spherulite is spherical, the simplest model to apply to the amplitude method to describe the observed scattering behavior would be that of a uniform isotropic sphere of polarizability α_0 and radius R_0. Starting with this model, the following expression is obtained for the scattered intensity:[28]

$$I = AV_0^2\alpha_0^2[(3/U^3)\ (\sin U - U \cos U)]^2$$

where I is the intensity, A is a proportionality constant, and V_0 is the volume of the isotropic sphere. The shape factor is

$$U = (4\pi R_0/\lambda')\ \sin\ (\theta/2) \tag{5}$$

λ' denoting the wavelength of light in the medium, and θ the polar scattering angle.

The undeformed spherulite is not isotropic; instead, it has different radial and tangential refractive indices due to the ordered arrangement of anistropic crystallites along its radii. Thus, a more reasonable model with which to represent the undeformed spherulite is that of an anisotropic sphere.

Stein and Rhodes[1] first considered the problem of the SALS patterns to be expected from a homogeneous anisotropic sphere is an isotropic or anisotropic medium. They assumed in their derivation that the optic axis was parallel to the radial fibril axis, and that there was rotational symmetry in the plane perpendicular to the fibril axis (a uniaxial indicatrix). Later, van Aartsen[2] rederived their equations and extended them to include the case where the angle between the optic axis and the radial fibril direction (defined as β) could be $90°$. The correct form of the equations relating the intensity of the scattered light to the optical parameters. for the case where the optic axis is parallel to the radial fibril axis (this corresponds to Stein and Rhodes' original restrictions, i.e., $\beta = 0°$) are:

$$I_{V_v} = A\rho^2V_0^2(3/U^3)^2\{(\alpha_1 - \alpha_{s1})\ (SiU - \sin U) + (\alpha_2 - \alpha_{s2})$$
$$\times\ (2 \sin U - U \cos U - SiU) + (\alpha_1 - \alpha_2)[\cos^2\ (\theta/2)/\cos \theta]\cos^2 \mu$$
$$\times\ (4 \sin U - U \cos U - 3SiU)\}^2 \tag{1}$$

$$I_{H_v} = A\rho^2V_0^2(3/U^3)^2\{(\alpha_1 - \alpha_2)[\cos^2\ (\theta/2)/\cos \theta] \sin \mu \cos \mu$$
$$\times\ (4 \sin U - U \cos U - 3SiU)\}^2 \tag{2}$$

where V_0 is the volume of the anisotropic sphere, θ and μ are the radial and azimuthal scattering angles, and A is a proportionality constant. SiU is the sine integral defined by

$$SiU = \int_0^U (\sin x/x)\ dx \tag{3}$$

and is solved as a series expansion sum for computational purposes. U has the same definition as in the isotropic sphere model [eq. (5)] with R_0 now the radius of the anisotropic sphere. U has the same definition for both the isotropic and anisotropic sphere models, since U depends only on the shape of the model. ρ is a geometric polarization correction term defined as

$$\rho = \cos\theta\,(\cos^2\theta + \sin^2\theta\,\cos^2\mu)^{-1/2} \tag{4}$$

The terms α_1, α_2, α_{s1}, and α_{s2} are polarizability terms. In van Aartsen's derivation,[2] the polarizabilities of the cylindrically symmetrical volume elements are α_1 in the direction of the optic axis and α_2 perpendicular to it. The symbols α_{s1} and α_{s2} represent here the polarizability of the surrounding medium in the α_1 and α_2 directions, respectively. When β, the angle between the optic axis and the spherulite radial-fibril direction, is zero (i.e., the optic axis is parallel to the radial fibril direction), $\alpha_1 = \alpha_r$, where α_r is the polarizability parallel to the radial fibril direction, and $\alpha_2 = \alpha_t$, where α_t is the polarizability perpendicular to the radial fibril direction. Thus, for the case of $\beta = 0°$ the polarizability term in the expression for H_V SALS [Equation (2)] becomes $(\alpha_r - \alpha_t)$, while the polarizability terms in the V_V SALS expression [eq. (1)] are:

$$
\begin{aligned}
(\alpha_1 - \alpha_{s1}) &= (\alpha_r - \alpha_{sr}) \\
(\alpha_2 - \alpha_{s2}) &= (\alpha_t - \alpha_{st}) \\
(\alpha_1 - \alpha_2) &= (\alpha_r - \alpha_t)
\end{aligned}
\tag{6}
$$

Here α_{sr} and α_{st} are the polarizabilities of the surroundings in the radial and tangential directions, respectively. The distinction that the term $(\alpha_1 - \alpha_2)$ equals $(\alpha_r - \alpha_t)$ was overlooked by van Aartsen,[2] and thus he concluded that eqs. (1) and (2) were "directly comparable" to that derived by Stein and Rhodes earlier.[1] However, in the Stein-Rhodes equations for I_{H_v} and I_{V_v} the term $(\alpha_1 - \alpha_2)$ is written as $(\alpha_t - \alpha_r)$.[1] Though this small error will have no effect on the evaluation of H_V SALS patterns, it has serious consequences for the evaluation of V_V SALS patterns.

The equations describing the intensity distribution of scattered light for the case when the optic axis is perpendicular to the radial fibril direction ($\beta = 90°$), have the form:

$$I_{V_v} = A'\rho^2 V_0^2 (3/U^3)^2 \big\{ (\alpha_2 - \alpha_{s2})(\mathrm{Si}U - U\cos U)$$
$$+ (\alpha_1 - \alpha_{s1})(2\sin U - U\cos U - \mathrm{Si}U)$$
$$+ (\alpha_2 - \alpha_1)[\cos^2(\theta/2)/\cos\theta]\cos^2\mu(4\sin U - U\cos U - 3\mathrm{Si}U)\big\}^2 \tag{7}$$
$$I_{H_v} = A'\rho^2 V_0^2 (3/U^3)^2 \big\{ (\alpha_2 - \alpha_1)[\cos^2(\theta/2)/\cos\theta]\sin\mu\cos\mu$$
$$\times (4\sin U - U\cos U - 3\mathrm{Si}U)\big\}^2 \tag{8}$$

When $\beta = 90°$, the radial polarizability α_r equals α_2. Now, however, since the polarizability α_1 is in the direction of the optic axis, and the optic axis is perpendicular to the radius and rotates randomly about it; there will be two polarizabilities perpendicular to the radius, α_1 in the optic-axis direc-

tion, and α_2 in the direction perpendicular to the radius and to the optic axis, with random rotation of the optic axis about the radius. The effective tangential polarizability will therefore be $(\alpha_1 + \alpha_2)/2$ as pointed out in the Results and Discussion section on spherulite optics, where n_α and n_γ were used instead of n_1 and n_2. If this substitution is made, it then follows for the case where $\alpha_{s1} = \alpha_{s2}$, that,

$$(\alpha_2 - \alpha_s) = \alpha_r - \alpha_s$$

$$\alpha_t = (\alpha_1 + \alpha_2)/2$$

So

$$\alpha_1 = 2\alpha_t - \alpha_r$$

$$(\alpha_1 - \alpha_s) = (2\alpha_t - \alpha_r) - \alpha_s = 2(\alpha_t - \alpha_s) - (\alpha_r - \alpha_s)$$

and

$$(\alpha_2 - \alpha_1) = \alpha_r - (2\alpha_t - \alpha_r) = (\alpha_r - 2\alpha_t + \alpha_r) = 2(\alpha_r - \alpha_t) \quad (9a)$$

Thus, for the case $\beta = 90°$, the polarizability term in the expression for H_V SALS (eq. 8) becomes $2(\alpha_r - \alpha_t)$, while the first two terms in the V_V SALS expression (eq. 7) become:

$$(\alpha_2 - \alpha_s)(SiU - U \cos U) + (\alpha_1 - \alpha_s)[2 \sin U - U \cos U - SiU]$$

$$= (\alpha_r - \alpha_s)(SiU - U \cos U) + [2(\alpha_t - \alpha_s)$$

$$- (\alpha_r - \alpha_s)][2 \sin U - U \cos U - SiU]$$

$$= (\alpha_r - \alpha_s)[SiU - U \cos U - 2 \sin U + U \cos U + SiU]$$

$$+ 2(\alpha_t - \alpha_s)[2 \sin U - U \cos U - SiU] = 2(\alpha_r - \alpha_s)$$

$$\times (SiU - \sin U) + 2(\alpha_t - \alpha_s)(2 \sin U - U \cos U - SiU) \quad (9b)$$

since $(\alpha_2 - \alpha_1) = 2(\alpha_r - \alpha_t)$, eq. (7) becomes

$$I_{V_v} = A'\rho^2 V_0^2 (3/U^3)^2 \{2(\alpha_r - \alpha_s)(SiU - \sin U)$$

$$+ 2(\alpha_t - \alpha_s)(2 \sin U - U \cos U - SiU) + 2(\alpha_r - \alpha_t)$$

$$\times [\cos^2 (\theta/2)/\cos \theta] \cos^2 \mu (4 \sin U - U \cos U - 3SiU)\}^2 \quad (9c)$$

The constant multiplier A' in eqs. (7) and (8) is defined by van Aartsen[2] as $A' = A/4$. Extracting the constant term $(2)^2$ from the three terms in the brace and placing it with the constant multiplier A' yields, $4A' = 4(A/4) = A$, and

$$I_{V_v} = A\rho^2 V_0^2 (3/U^3)^2 \{(\alpha_r - \alpha_s)(SiU - \sin U)$$

$$+ (\alpha_t - \alpha_s)(2 \sin U - U \cos U - SiU) + (\alpha_r - \alpha_t)$$

$$\times [(\cos^2 (\theta/2)/\cos \theta)] \cos^2 \mu (4 \sin U - U \cos U - 3SiU)\}^2 \quad (7')$$

Also, eq. (8) is now:

$$I_{H_v} = A\rho^2 V_0^2 (3/U^3)^2 \{(\alpha_r - \alpha_t)[\cos^2 (\theta/2)/\cos \theta)] \sin \mu \cos \mu$$

$$\times (4 \sin U - U \cos U - 3SiU)\}^2 \quad (8')$$

Equations (1) and (7') for I_{V_v} and eqs. (2) and (8') for I_{H_v} are now identical when examined in terms of the fibril polarizabilities α_r and α_t.

Equations (7') and (8') have been programmed by C. E. Green for an EMR 6130 computer with a Calcomp plotter attachment.[14] Two sample data sets for spherulites and two sample data sets for disks are listed with the program. When the spherulite data sets are inserted in the system, the H_V SALS and V_V SALS patterns shown in Figure 7 are computed and plotted. These patterns should be compared with those obtained experimentally from undeformed, negatively birefringent, isotactic polypropylene spherulites (Fig. 2). With this program the computer can be used as a mathematical diffractometer to evaluate theoretical SALS patterns.

In the H_V SALS relations, eqs. (2) and (8') the magnitude of A and $(\alpha_r - \alpha_t)$ affect only the absolute magnitude of the calculated intensity and not the position of θ_{max}. Thus these parameters do not influence the calculation of spherulite size from the H_V SALS patterns. The calculation of the V_V SALS pattern, however, is affected by the magnitude and the sign of the polarizabilities of both the spherulite and the environment. The V_V SALS equation [see eq. (1)] is made up of three terms. The first term, $(\alpha_r - \alpha_{sr})$ $(SiU - \sin U)$, has spherical symmetry, the second term, $(\alpha_t - \alpha_{st})$ $(2 \sin U - U \cos U - SiU)$, has spherical symmetry in the low-angle regions but manifests some anisotropy in the weaker-intensity higher angular range. The third term, $(\alpha_r - \alpha_t)$ $[\cos^2(\theta/2)/\cos\theta] \cos^2\mu(4\sin U - U \cos U - 3SiU)$, is the major anisotropy term and is the primary contributer of anisotropy to the system. This is illustrated in Figure 31, which shows the computer calculation of the intensity distribution for each of the three terms in the I_{V_v} equation individually. The final V_v SALS pattern will be a composite of these three basic forms and will depend strongly on the magnitude of the polarizability weighting factors and their sign, as this determines whether, and by how much, these terms add or subtract.

The sensitivity of the V_V SALS patterns to the magnitude and the sign of the spherulite and background polarizabilities is shown in Figure 32. Four theoretical V_V SALS patterns were calculated from eq. (1) with constant values for α_r and α_t of 1.5093 and 1.5115, respectively, (a negative spherulite) and varying values for the magnitude of the background polarizabilities. In cases A and B the background polarizability is assumed to be isotropic ($\alpha_{sr} = \alpha_{st}$). In case A the background is assumed equal in magnitude to that of the tangential polarizability of the spherulite (1.5115) and thus $(\alpha_t - \alpha_{st}) = 0$, and $\alpha_t = \alpha_{st} = \alpha_{sr}$. In case B the background polarizability is assumed to be that corresponding to the radial refractive index of the spherulite (1.5093). Here $(\alpha_r - \alpha_{sr}) = 0$ and $\alpha_r = \alpha_{sr} = \alpha_{st}$. In each of these two cases only two of the terms in eq. (1) are added as the third term in the equation [either the term with the prefix $(\alpha_t - \alpha_{st})$ or $(\alpha_r - \alpha_{sr})$] is equal to zero. The difference in the form of the two theoretical figures is obvious.
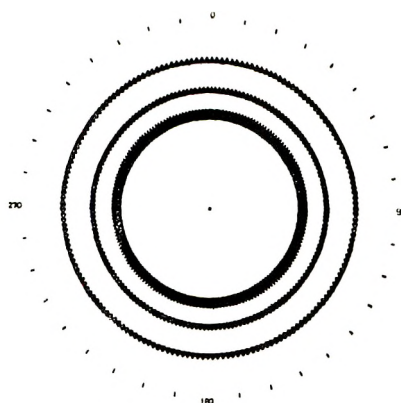
$$I_{V_V} = A\rho^2 V_0^2 (3/U^3)^2 (SiU - sinU)^2$$
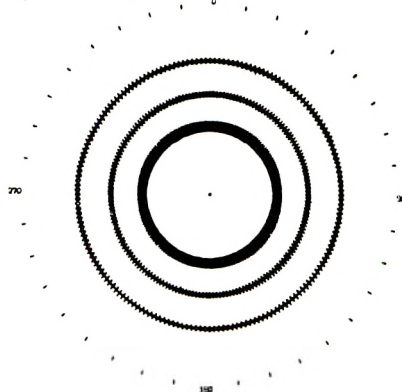
$$I_{V_V} = A\rho^2 V_0^2 (3/U^3)^2 (2 \, sinU - U \, cos \, U - SiU)^2$$
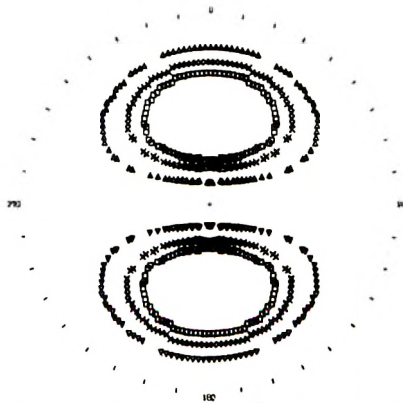
$$I_{V_V} = A\rho^2 V_0^2 (3/U^3)^2 [cos^2(\Theta/2)/cos\theta] cos^2\mu (4 \, sin \, U - U \, cos \, U - 3SiU)]^2$$

Fig. 31. Intensity distribution for each of the three terms in the V_v SALS equation for anisotropic spheres.
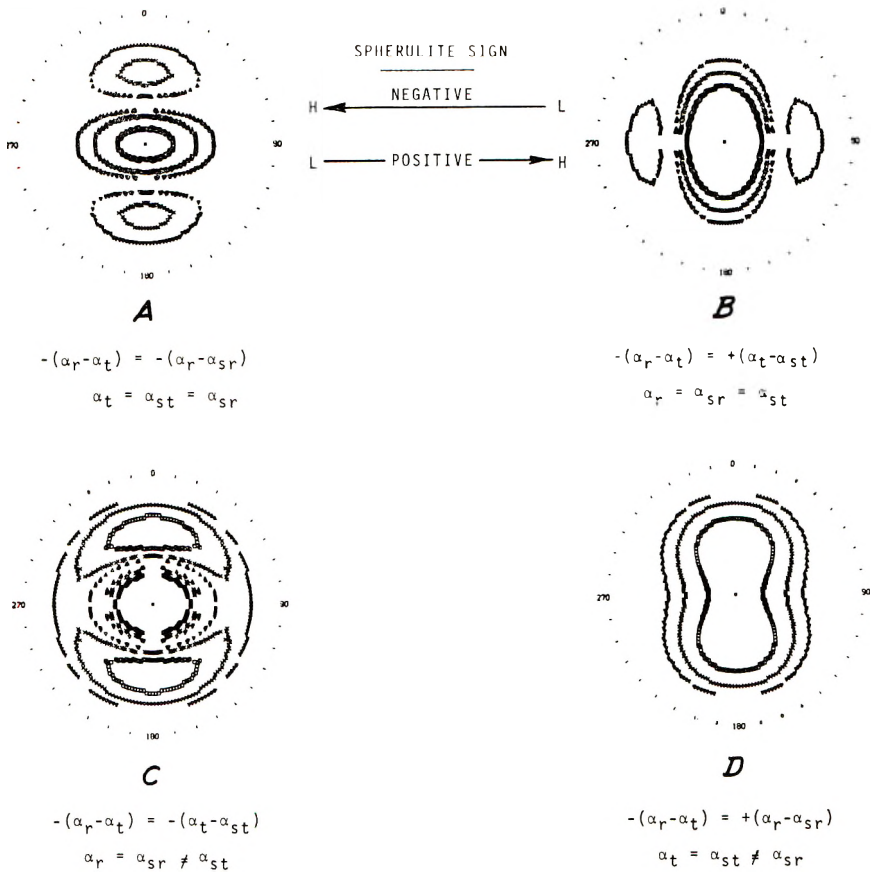
Fig. 32. Effect of both the magnitude and the sign of the spherulite and background polarizabilities on the theoretical V_v SALS pattern from anisotropic spheres.

The bottom two V_V SALS patterns were obtained by assuming that the background polarizability is anisotropic. Only in this way can the $(\alpha_t - \alpha_{st})$ term be added to the $(\alpha_r - \alpha_t)$ term while $(\alpha_r - \alpha_{sr}) = 0$, to produce the V_v SALS pattern shown in Figure 32C; or can the $(\alpha_r - \alpha_{sr})$ term be subtracted from the $(\alpha_r - \alpha_t)$ term while $(\alpha_t - \alpha_{st}) = 0$, to produce the V_V SALS pattern shown in Figure 32D. In both these calculations, the anisotropy of the background required to produce the figures was $(\alpha_{sr} - \alpha_{st}) = -4.4 \times 10^{-3}$, a higher anisotropy than that of the spherulite $[(\alpha_r - \alpha_t) = -2.2 \times 10^{-3}]$. Thus, the conditions required to produce theoretical Figures 32C and 32D are highly unrealistic from a physical point of view, as it is difficult to imagine a likely physical system which would have undeformed spherulites in a medium which has a higher anisotropy than the spherulites themselves.

Whether the prefix of the third term in eq. (1) is $(\alpha_r - \alpha_t)$ or $(\alpha_t - \alpha_r)$ determines which of the sets of two patterns in Figure 32 represents those which should be obtained from an isotropic background. The experi-

mentally observed V_V SALS patterns from solid polymer films all fall into the general category of theoretical Figures 32A and 32B. When the prefix of the third term in eq. (1) equals $(\alpha_t - \alpha_r)$,[1] these same figures can only be computed mathematically if an anisotropic background is assumed. This is why an earlier analysis of V_V SALS theory[15] concluded that the background in synthetic polymer films must be anisotropic. As the correct form of the prefix for the third term in eq. (1) has now been shown to be $(\alpha_r - \alpha_t)$, this difficulty is removed, and the background in polymer films can now be considered isotropic.

It is interesting to note that V_V SALS patterns A and B in Figure 32 represent only two of a large range of patterns that would be obtained if the birefringence of the spherulite is fixed and the refractive index of the isotropic background is changed. Under these conditions theory predicts that the direction of the change in the V_V SALS patterns will depend on the sign of the birefringence of the spherulite. When the birefringence of the spherulite is negative [i.e., $(\alpha_r - \alpha_t)$ is negative] α_t is greater than α_r and theoretical V_V SALS pattern A in Figure 32 would appear at a higher background refractive index than V_V SALS pattern B. Conversely, for a positive spherulite such as rice starch α_r is greater than α_t, and V_V SALS pattern B would be predicted to occur at a higher background refractive index than V_V SALS pattern A (see Figs. 15, 16, and 17). Thus, theoretically the same V_V SALS pattern can be obtained from either a positive or negative birefringent spherulite, depending on the refractive index of its background, but the direction of change in the V_V SALS pattern with changing background refractive index will be determined by the sign of the birefringence of the spherulite. This theoretical prediction is confirmed experimentally.

Correspondence of the Sphere and Disk Equations

A decrease in the dimensionality of a model from three to two simplifies the mathematics and is thus more likely to lead to equations which can be solved in a closed form. An optically anisotropic disk can be considered as the two-dimensional analog of a three-dimensional, optically anisotropic spherulite. Stein and Wilson[22] derived the SALS equations for an optically anisotropic disk, and Stein and Clough[24] extended them to include such variables as optic axis alignment and disk deformation. These variables could be included in the disk equations only because of the simplifications attending the decrease in dimensionality of the model.

Since the two-dimensional and three-dimensional optically anisotropic models are functionally analogous, the final derived equations are expected to yield similar results. Comparison of the V_V SALS patterns predicted for spherulites by Stein and Rhodes' three-dimensional equations[1] with that predicted for disks by Stein and Wilson's[22] two-dimensional equations showed that the disk patterns would be entirely different from those predicted for spheres under the same optical conditions. Recognition of this difference led Picot[18] to the erroneous conclusion that isotactic polystyrene

spherulites had to have disk-like character in order to produce the experimentally observed V_v SALS patterns.

Picot's problem was his acceptance of the reliability of the V_v SALS equations. The two-dimensional disk equations were correct but the sphere equations were in error. When the correct form of the three dimensional optically anisotropic sphere equation is used, the predicted sphere V_v SALS patterns now become similar in form to those predicted for disks. In fact the final forms of the equations themselves also become very similar and suggest the correspondence further interrogation verifies.

For the case where the optic axis lies in the plane of the disk the V_v SALS equation for anisotropic disks has the form:[22,24]

$$I_{V_v} = \{A\rho A_0 (2/\omega^2)[(\alpha_r - \alpha_{s,r})J' + (\alpha_t - \alpha_{s,t})(J'' - J')$$
$$+ (\alpha_r - \alpha_t)\cos^2\mu(J'' - 2J')]\}^2 \quad (10)$$

This should be compared with the analogous expression for three-dimensional anisotropic spheres:

$$I_{V_v} = \{A\rho V_0(3/U^3)[(\alpha_r - \alpha_{s,r})S' + (\alpha_t - \alpha_{s,t})(S'' - S')$$
$$+ (\alpha_r - \alpha_t)\cos^2\mu F(S'' - 3S')]\}^2 \quad (1')$$

where

$$
\begin{aligned}
J' &= 1 - J_0(\omega) \\
J'' &= \omega J_1(\omega) \\
S' &= \mathrm{Si}U - \sin U \\
S'' &= \sin U - U\cos U
\end{aligned}
\quad (11)
$$

Here, eq. (1') for anisotropic spheres is identical to eq. (1). The term F equals $[\cos^2(\theta/2)/\cos\theta]$, which for the small angles considered in this discussion can be assumed equal to unity ($F' = 1$).

Identical terms have the same definition in eqs. (10) and (1'). Thus α_r and α_t denote the polarizability parallel and perpendicular, respectively, to the radial fibril direction of the sphere or disk, and $\alpha_{s,r}$ and $\alpha_{s,t}$ denote the polarizability of the disk or sphere background in the radial and tangential directions, respectively. In both the disk and sphere case $\alpha_{s,r} = \alpha_{s,t} = \alpha_s$ when the background polarizability is isotropic. In eq. (11), ω is the form factor for disks, i.e. the two-dimensional analog of the sphere form factor U. Thus

$$\omega = (2\pi R_0/\lambda')\sin\theta \quad (12)$$

while

$$U = (4\pi R_0/\lambda')\sin(\theta/2) \quad (5)$$

Here R_0 is the radius of the disk in eq. (12) and the radius of the sphere in eq. (5). The similarity between these expressions is obvious. $J_0(\omega)$

is the zero-order Bessel function and $J_1(\omega)$ is the first-order Bessel function of ω.

The symmetry between eqs. (10) and (1′) goes even further. Thus in the two-dimensional case [eq. (10)] the three optical anisotropic terms are multiplied by both A_0, the area of the disk $(A_0 = \pi R_0^2)$ and the term $(2/\omega^2)$, while the comparable three-dimensional terms in eq. (1′) are V_0, the volume of the sphere $[V_0 = (4/3)\pi R_0^3]$ and the term $(3/U^3)$. Thus, even the numerical magnitudes, the constant 2 and the second power of ω for the two-dimensional case, and the constant 3 and the third power of U for the three-dimensional case, carry over the symmetry of these expressions. A similar numerical relation exists between the constant 2 in the third optical anisotropic term $(J'' - 2J')$ of eq. (10) and the constant 3 in the third anisotropic term $(S'' - 3S')$ of eq. (1′).

An examination of the expression $(3/U^3)$ $(4 \sin U - U \cos U - 3SiU)$ from eq. (2) for spheres has shown that $U_{\max} = 4.02$. Here, $U_{\max}$ is the value of U at which the intensity is a maximum. A knowledge of $U_{\max}$ resulted in a quantitative expression between R_0 and the radial angle $\theta_{\max}$, the radial angle at which maximum intensity appears; and led from there to a practical technique for determining the size of spherulites from the H_V SALS pattern. The H_V SALS equation for disks is:

$$I_{H_v} = A\rho^2 A_0^2(\alpha_r - \alpha_t)^2 \sin^2 2\mu(1/\omega^2)^2\{2J' - J''\}^2 \tag{13}$$

The expression $(1/\omega^2)(2J' - J'')$ from eq. (13) for disks yields a value of $\omega_{\max} = 3.92$. Here $\omega_{\max}$ is the value of ω at which the intensity reaches a maximum, that is, $\omega_{\max}$ is the two-dimensional analog of $U_{\max}$. Substitution of the value of $\omega_{\max}$ into eq. (12) leads to the following relation between R_0 (disk) and $\theta_{\max}$:

$$R_0(\text{disk}) = 1.96\lambda'/\pi \sin \theta_{\max} \tag{14}$$

The comparable equation for spheres is:

$$R_0(\text{sphere}) = 1.025\lambda'/\pi \sin (\theta_{\max}/2) \tag{15}$$

The constant, 1.96, in eq. (14) is almost twice that of 1.025 in eq. (15). However the denominator in eq. (14), $\sin \theta_{\max}$, is twice that of $\sin (\theta_{\max}/2)$ in eq. (15), so that the two equations represent almost identical relations. For example, a spherulite with a radius of $1\ \mu$ will have a H_V SALS intensity maximum at $\theta_{\max} = 23.8°$ if λ' is 6320 Å. For the same wavelength of light in the medium, a disk with a radius of $1\ \mu$ will have a H_V SALS intensity maximum at $\theta_{\max} = 23.3°$. Thus the intensity maximum in the H_V SALS pattern obtained from a disk and from a sphere of the same radius will fall in the same radial angular region.

The obvious symmetry of these functionally analogous expressions suggests that the V_V SALS patterns produced by them under comparable optical conditions should be similar. This conclusion was verified by computer interrogation as shown in Figures 15–21 and in Appendix II. The characteristic predictions for H_V SALS behavior are also analogous. Thus by

use of the correct form of the anisotropic sphere equations the expected correspondence between the two-dimensional and three-dimensional models has now been confirmed.

APPENDIX II

A Catalog of V_v SALS Patterns

In this section a catalog of disk and sphere V_v SALS patterns is presented. The V_v SALS patterns illustrate the characteristic modes of transformation that occur during progression from one of the limiting patterns in Figure 32 to another. The purpose of this catalog is to supply investigators who do not have access to a computer with a ready means for extracting useful information from their experimental V_v SALS patterns. By using this catalog as a guide, investigators can determine whether their patterns are representative of disk or sphere structures, as well as something about the anisotropic optical character of their material.

The catalog also has obvious instructional uses. It makes available a complete overview of the forms V_v SALS patterns can take. Since the manner of transformation from one pattern to another often has an unusual and unexpected character, prior familiarity with these changing forms is desirable. Similarly, having disk and sphere V_v SALS patterns produced under identical optical conditions identifies visually those special conditions for which sphere and disk patterns differ. This information should be helpful in guiding the investigator along fruitful experimental directions.
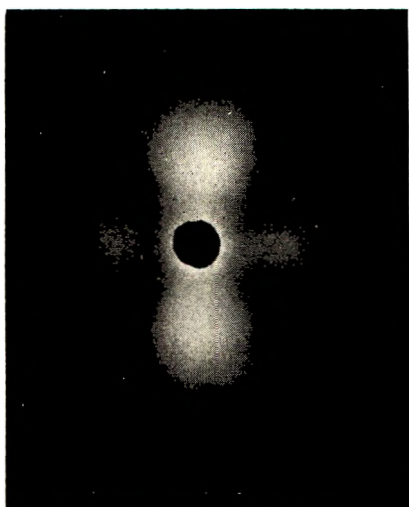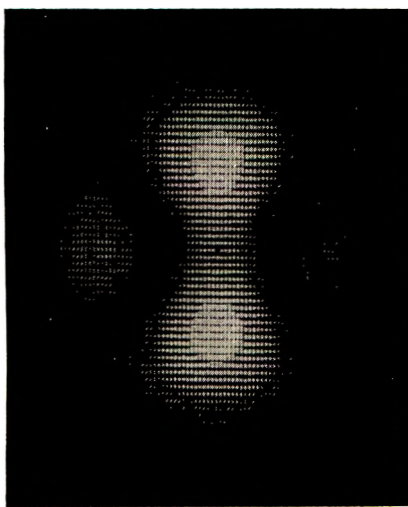
EXPERIMENTAL   THEORETICAL

Fig. 33. Comparison between an experimental V_v SALS pattern from cast isotactic polypropylene film and theoretical V_v SALS test pattern 1 produced by the line-printer program.
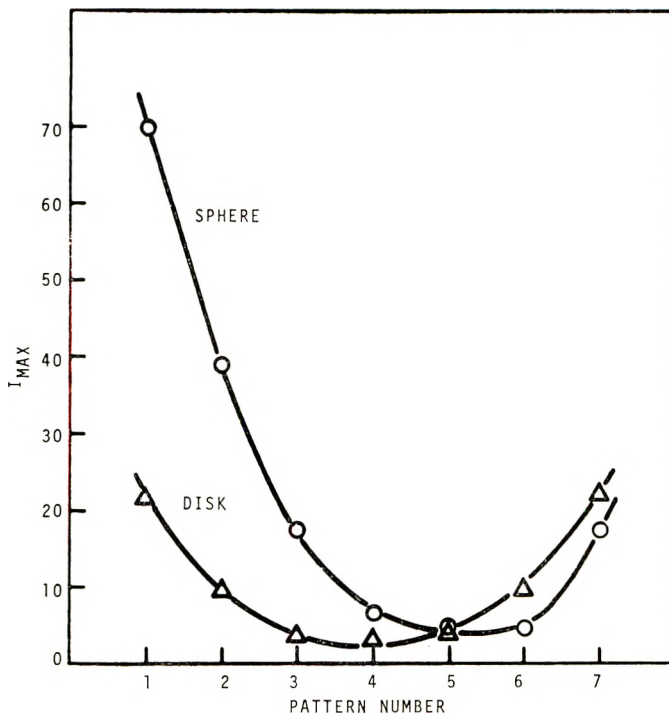
Fig. 34. Relation between the maximum pattern intensity I_{max} and the V_v SALS pattern identification number for the first set of cataloged V_v SALS patterns (pattern B to pattern A): (O) spheres; (Δ) disks.

Other instructional aspects of this catalog are discussed in some detail below.

Operationally the theoretical V_v SALS patterns are presented in the catalog in a form which closely represents the visual character of the experimentally photographed patterns. This was accomplished by applying the pictorial output approach of Macleod[29] to the SALS computer program so that a representation of the complete intensity spectrum of the computed V_v SALS pattern could be produced by a line printer.[30]* A scale of twenty different intensity values was created with the line printer by selection of type characters and overprints. The intensity values of these typed characters were measured with a reflectometer in order to select a linear intensity sequence. The calculated theoretical intensity values of a V_v SALS pattern are then normalized over these twenty intensity characters and plotted in their correct spatial positions by the line printer. The result is a V_v SALS pattern that looks like a negative of the experimentally obtained pattern. A photonegative is then made of the line printer V_v SALS pattern so that it more nearly resembles the experimental patterns. This is illustrated in Figure 33, where an experimental V_v SALS pattern

*The computer program may be obtained from the authors, C. E. Green and O. W. Marks of this laboratory.
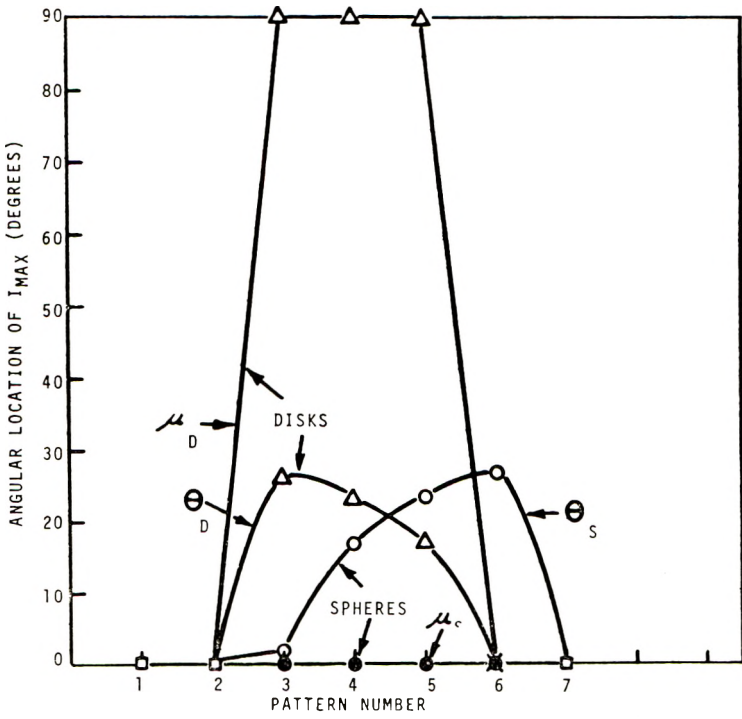
Fig. 35. Angular location of I_{max} in the first set of cataloged V_c SALS patterns (pattern B to pattern A): (○) spheres, θ at I_{max}; (●) spheres, μ at I_{max}; (△) disks, θ at I_{max}; (▲) disks, μ at I_{max}; (□) $\theta = \mu = 0°$ for both disks and spheres; (×) $\theta = \mu = 0°$ for disks and $\mu = 0°$ for spheres.
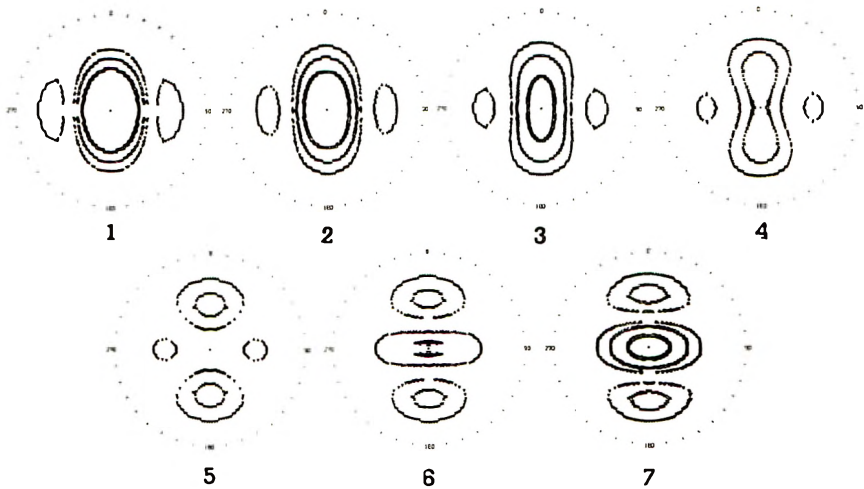
Fig. 36. Fixed-intensity contour plot representation of the changes that occur in anisotropic-sphere V_c SALS patterns with changing optical background. This is the same sequence, using the same optical parameters, as in Fig. 38 (see Table I).

TABLE 1A

Transformation of Theoretical V_V SALS Patterns: Anisotropy Parameters

Polarizability term	Basic V_V SALS Patterns (Fig. 37)			
	A	B	C	D
$(\alpha_r - \alpha_t)$	-0.0030	-0.0030	-0.0030	-0.0030
$(\alpha_t - \alpha_{st})$	0	$+0.0030$	-0.0030	0
$(\alpha_r - \alpha_{sr})$	-0.0030	0	0	$+0.0030$

obtained from isotactic polypropylene is compared with the theoretical V_V SALS pattern from test pattern 1 (see Fig. 7b) which was produced using this modified program. Note that the intensity goes from white at the maximum to black at the minimum for the calculated patterns.

In order to make this catalog as versatile as possible, an anisotropic optical background is used to produced the patterns. The four patterns in
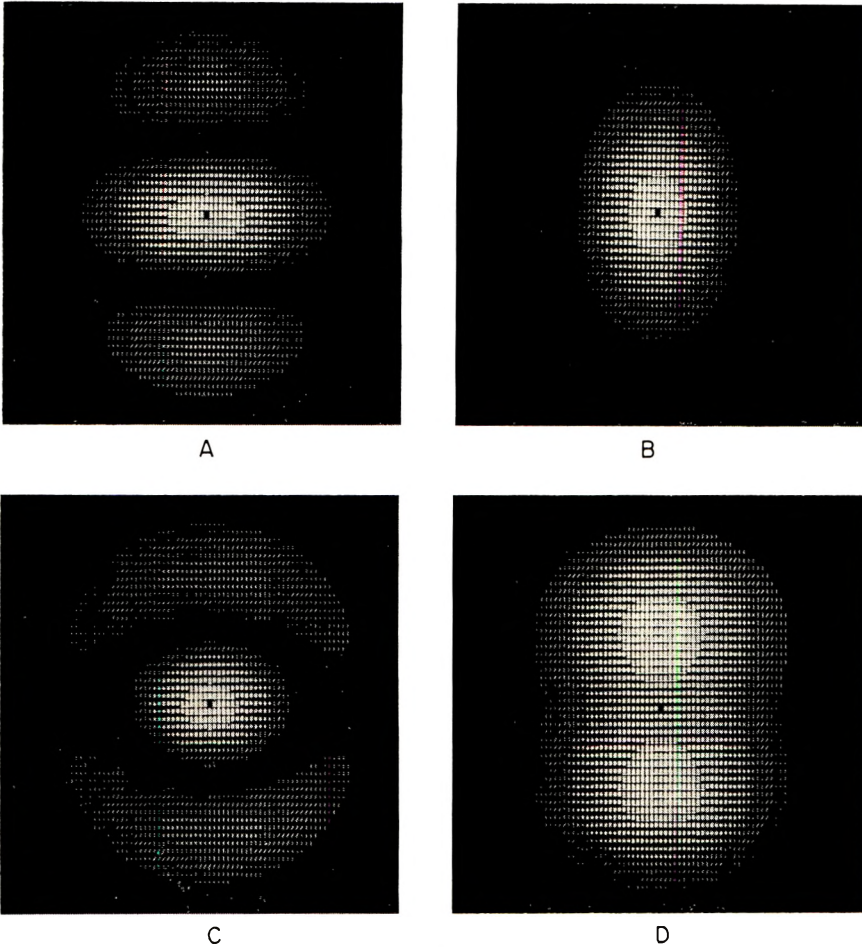
Fig. 37. Basic theoretical V_V SALS patterns.

R. J. SAMUELS

TABLE IB

Transformation	Polarizability term	Pattern number						
		1	2	3	4	5	6	7
$B \rightarrow A$ (Figs. 38, 39)	$(\alpha_r - \alpha_t)$	-0.0030	-0.0030	-0.0030	-0.0030	-0.0030	-0.0030	-0.0030
	$(\alpha_t - \alpha_{st})$	$+0.0030$	$+0.0025$	$+0.0020$	$+0.0015$	$+0.0010$	$+0.0005$	0
	$(\alpha_r - \alpha_{sr})$	0	-0.0005	-0.0010	-0.0015	-0.0020	-0.0025	-0.0030
$D \rightarrow B$ (Figs. 40, 41)	$(\alpha_r - \alpha_t)$	-0.0030	-0.0030	-0.0030	-0.0030	-0.0030	-0.0030	-0.0030
	$(\alpha_t - \alpha_{st})$	0	$+0.0005$	$+0.0010$	$+0.0015$	$+0.0020$	$+0.0025$	$+0.0030$
	$(\alpha_r - \alpha_{sr})$	$+0.0030$	$+0.0025$	$+0.0020$	$+0.0015$	$+0.0010$	$+0.0005$	0
$D \rightarrow C$ (Figs. 42, 43)	$(\alpha_r - \alpha_t)$	-0.0030	-0.0030	-0.0030	-0.0030	-0.0030	-0.0030	-0.0030
	$(\alpha_t - \alpha_{st})$	0	-0.0005	-0.0010	-0.0015	-0.0020	-0.0025	-0.0030
	$(\alpha_r - \alpha_{sr})$	$+0.0030$	$+0.0025$	$+0.0020$	$+0.0015$	$+0.0010$	$+0.0005$	0
$D \rightarrow A$ (Figs. 44, 45)	$(\alpha_r - \alpha_t)$	-0.0030	-0.0030	-0.0030	-0.0030	-0.0030	-0.0030	-0.0030
	$(\alpha_t - \alpha_{st})$	0	0	0	0	0	0	0
	$(\alpha_r - \alpha_{sr})$	$+0.0030$	$+0.0020$	$+0.0010$	0	-0.0010	-0.0020	-0.0030
$C \rightarrow A$ (Figs. 46, 47)	$(\alpha_r - \alpha_t)$	-0.0030	-0.0030	-0.0030	-0.0030	-0.0030	-0.0030	-0.0030
	$(\alpha_t - \alpha_{st})$	-0.0030	-0.0025	-0.0020	-0.0015	-0.0010	-0.0005	0
	$(\alpha_r - \alpha_{sr})$	0	-0.0005	-0.0010	-0.0015	-0.0020	-0.0025	-0.0030
$C \rightarrow B$ (Figs. 48, 49)	$(\alpha_r - \alpha_t)$	-0.0030	-0.0030	-0.0030	-0.0030	-0.0030	-0.0030	-0.0030
	$(\alpha_t - \alpha_{st})$	-0.0030	-0.0020	-0.0010	0	$+0.0010$	$+0.0020$	$+0.0030$
	$(\alpha_r - \alpha_{sr})$	0	0	0	0	0	0	0

Figure 32 (see Fig. 37 for comparisons) can be produced only if anisotropic background conditions are used. In this way all of the patterns from the disk and sphere equations are available for examination and evaluation. The spherulite anisotropy $(\alpha_r - \alpha_t)$ is fixed at a value of -0.0030 (a negative spherulite), and the background polarizability is varied in an anisotropic manner so as to produce a transformation between two of the patterns in Figure 32 in seven stages. Six different transformation paths are reproduced in this catalog.

In order to facilitate comparative studies, the catalog has the following format. (1) A table of variables is listed for each set of transformations (Table I). An identification number is listed with each set of variables. The number corresponds to the particular V_V SALS pattern these variables produced. (2) Two sets of seven V_V SALS patterns are produced from each set of variables. The first set shows patterns produced from the sphere equation and the second set shows patterns produced by the disk equation under the same set of conditions. (3) Each V_V SALS pattern is numbered to correspond with the numbering in the table of optical variables (Table I). (4) The maximum scaling intensity is listed above the designation number for each pattern.

It is necessary to record the intensity maximum (I_{max}) with each pattern if the patterns are to be compared. This is because the maximum intensity varies as a function of the distance of the background polarizabilities from the radial and tangential polarizabilities, and the character of that variation is different for spheres and disks. This intensity variation is not trivial, as it allows spheres and disks to be differentiated. Since each pattern is scaled to the maximum intensity calculated for that pattern, the intensity value must be recorded to prevent confusion during comparison.

This important feature of the V_V SALS patterns is best illustrated by examination of the first set of transformations in the catalog (Figs. 38 and 39 and Table I) along with Figures 34 and 35. This set of patterns corresponds to those produced under isotropic background conditions with $\beta = 0°$ (see for example Figs. 15–19). In Figure 34 the I_{max} value listed under each pattern is plotted as a function of the pattern number for both disks and spheres. It is apparent from this figure that the maximum intensity is greatest when the background polarizability is equal to one of the sphere or disk polarizabilities. For disks the intensity varies symmetrically between the two extreme high values, decreasing to a minimum when the two background polarizabilities are equal to each other and to the average for the disk. Sphere intensity variation is asymmetric, with the highest intensity for pattern number 1 (an intensity much higher than the comparable value for a disk), the minimum at pattern 6, and a second maximum (comparable in value to the equivalent disk) at pattern 7. The high maximum intensity for sphere pattern 1 causes the very low-intensity side lobes on the pattern to disappear. A similar phenomenon was observed with starch (see Figure 17). With pattern 1 for disks, the intensity differential

between the maximum and that of the side lobes is much smaller, and the side lobes appear in the pattern.

Examination of sphere patterns 5, 6, and 7 (Fig. 38) illustrates the importance of the I_{max} values for comparative purposes.   In pattern 7 the maximum intensity (lightest region) occurs at the center of the horizontal ellipse.   (The 0,0 position is always shown dark irrespective of its actual value since this position is computationally difficult; the dark center should be looked at as a small beam stop.)   In pattern 6 both the center of the upper lobes and that of the center ellipse have almost the same intensity, and by pattern 5 the upper lobes have the highest intensity.   Without a knowledge of I_{max} for each pattern, it would seem that the upper lobes in pattern 5 are as intense as the center ellipe was in pattern 7.   Examination of the I_{max} values shows this is not true (see also Figs. 15 and 16).   What has actually happened is that by pattern 5 the maximum intensity has decreased in the center lobe until it is weaker than that of the upper lobe in pattern 7; but the upper-lobe intensity has not changed at all in going from pattern 7 to pattern 5.

This point is further illustrated in Figure 36.   Here the same sphere patterns are calculated from the same variables (Table I Fig. 38) in the fixed intensity line profile form.   Again, the highest intensity is represented by squares, the next weakest by crosses, and the lowest value chosen by triangles.   Examination of patterns 5, 6, and 7 in this figure reveals that the intensity of the upper lobes remains constant during the transformation from pattern 7 to pattern 5, but the intensity of the center ellipse changes drastically.   Where the highest intensity squares appear only in the center ellipse in pattern 7, only weak triangle side-lobes appear along the equator of pattern 5.   Thus identification of I_{max} is necessary if a valid interpretation of the patterns in the catalog is to be made.

One final note on the catalog.   Comparison of the sphere and disk patterns under comparable optical conditions show under what optical conditions the spheres and disks can be differentiated experimentally.   The primary difference between the disk and sphere patterns in the sensitive transition region is in their intensity variation.   This point can be illustrated by examination of the sphere and disk patterns from the first set of transformations in the catalog (Figs. 38 and 39) along with Figure 35. In Figure 35 the variation in the radial angle θ and azimuthal angle μ at which I_{max} appears in the V_V SALS pattern is plotted against the pattern number.   This figure illustrates how differently the intensity varies spatially within the transition region for disks compared to spheres.   Outside the transition region, in patterns 1, 2, and 7 the intensity maximum is in the same position ($\theta = 0°$, $\mu = 0°$) for both spheres and disks and differentiation of form would be difficult.   By pattern 3, however, differentiation between spheres and disks has become pronounced.   In pattern 3 for spheres the high intensity region of the pattern remains along the meridian ($\mu_s = 0°$) with its center near the center of the pattern.   Only very weak side-lobes appear in this theoretical pattern.   In contrast, pattern 3 for
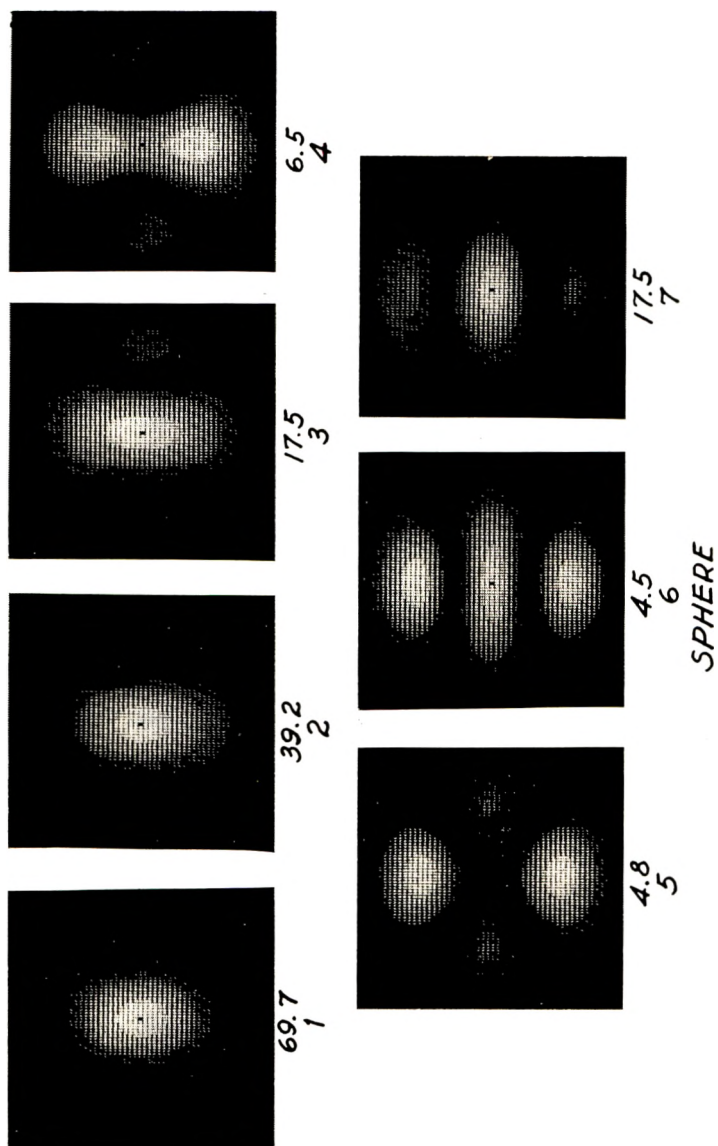
Fig. 38. Transformation of theoretical V_v SALS sphere pattern B to pattern A.
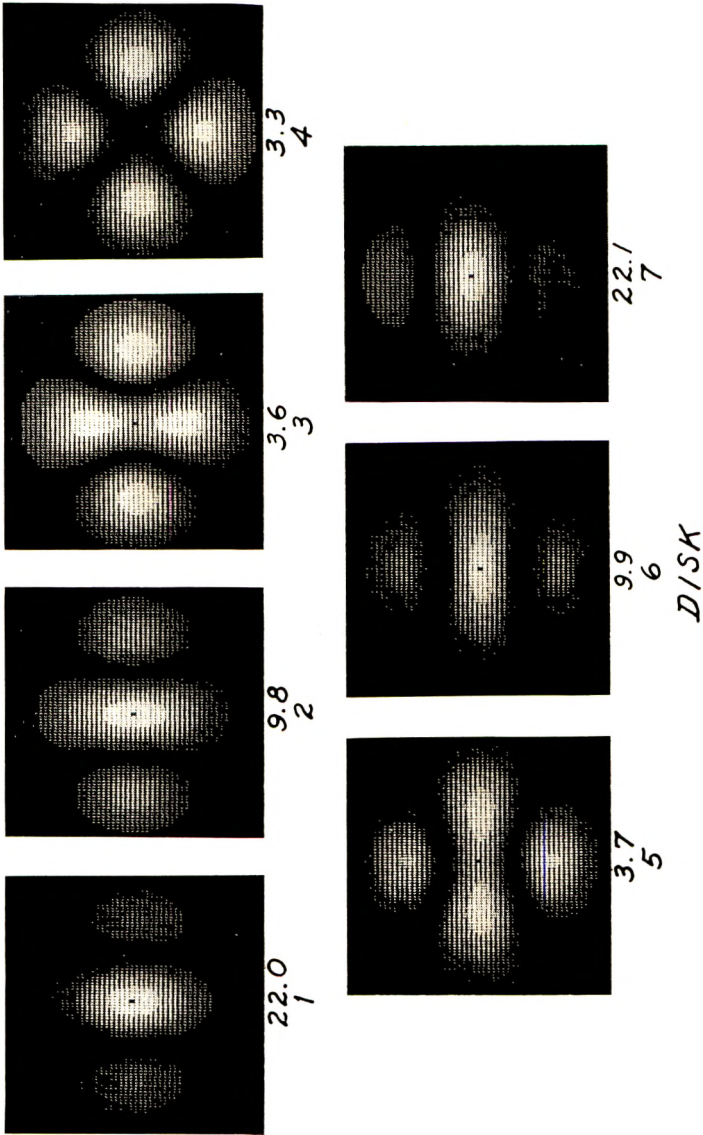
Fig. 39. Transformation of theoretical V_v SALS disk pattern B to pattern A.
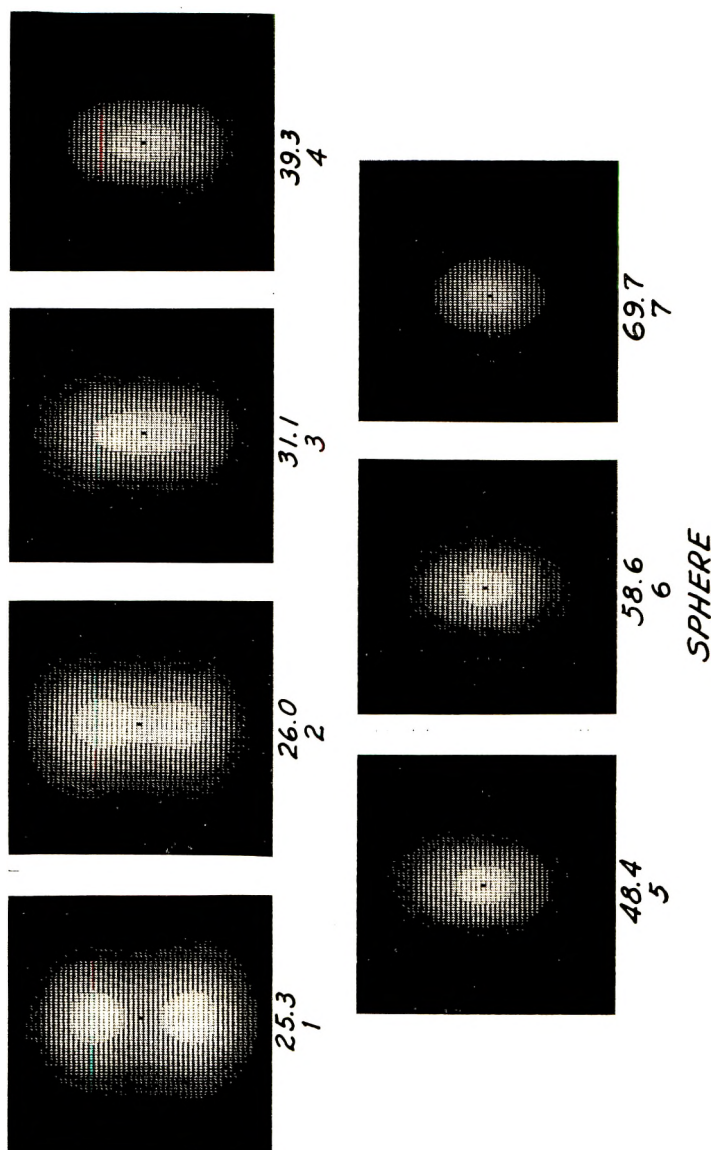
Fig. 40. Transformation of theoretical V_v SALS sphere pattern D to pattern B.
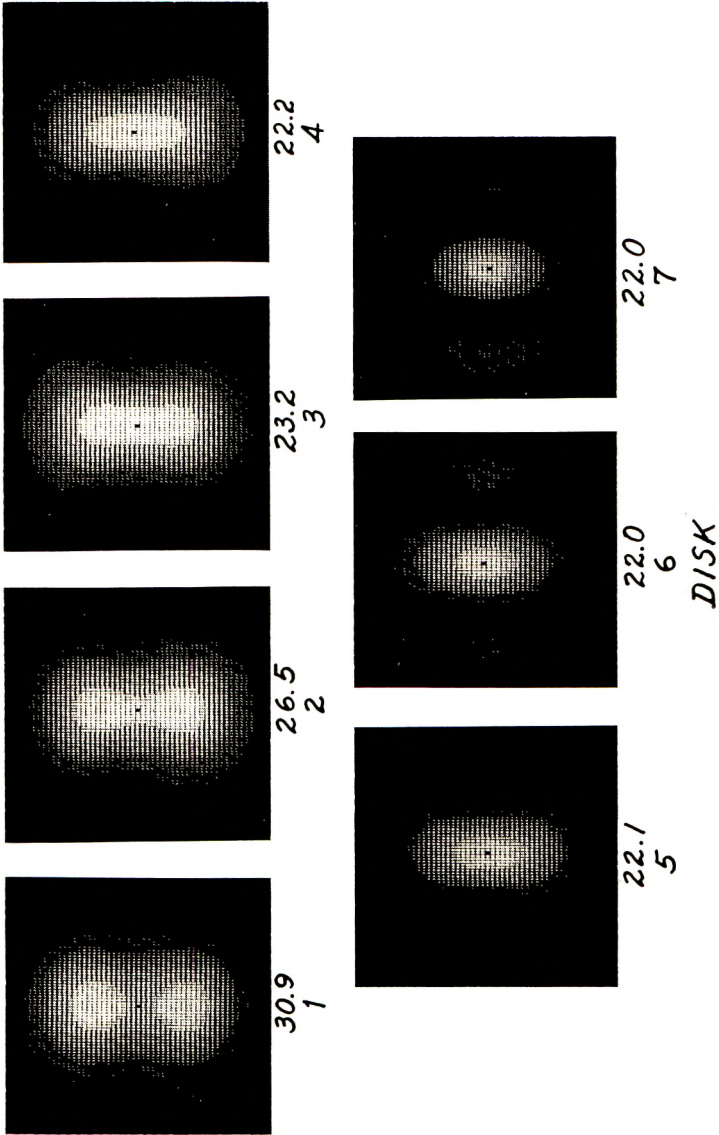
Fig. 41. Transformation of theoretical V_v SALS disk pattern D to pattern B.
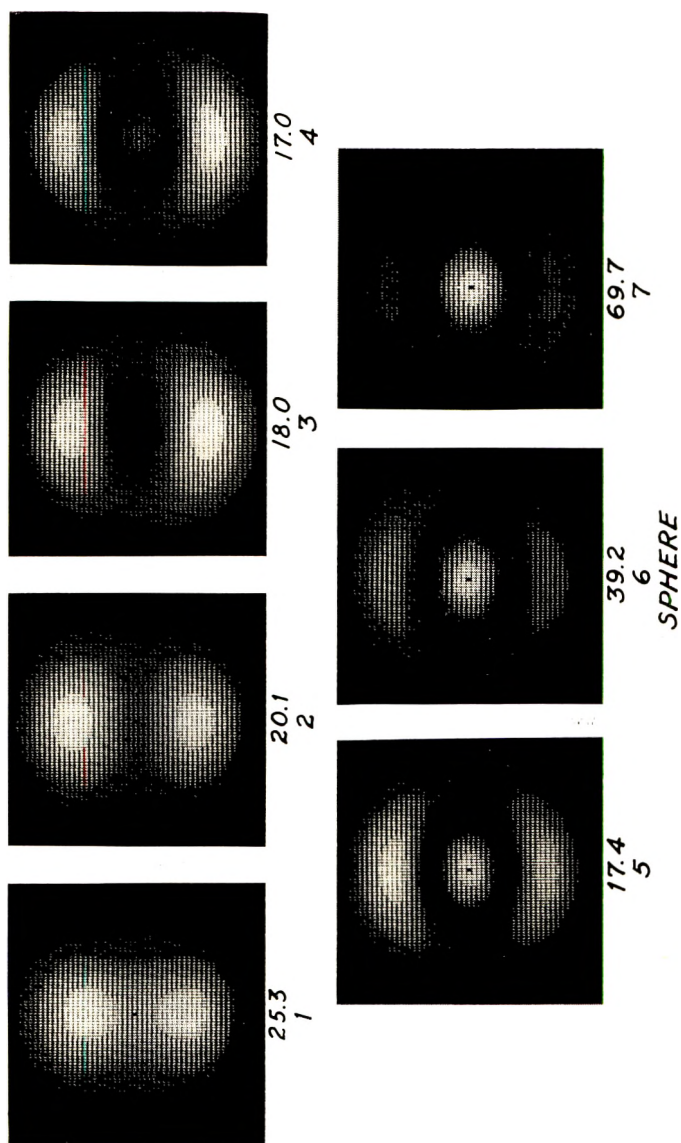
Fig. 42. Transformation of theoretical V_v SALS sphere pattern D to pattern C.
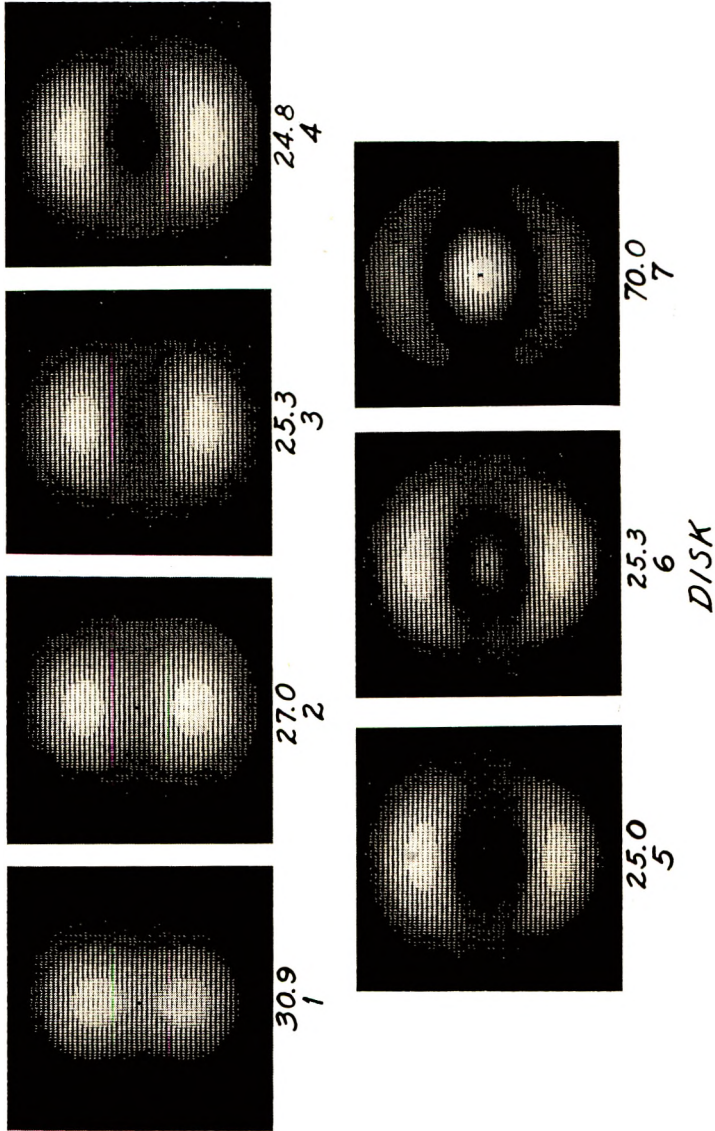
Fig. 43. Transformation of theoretical V_v SALS disk pattern D to pattern C.
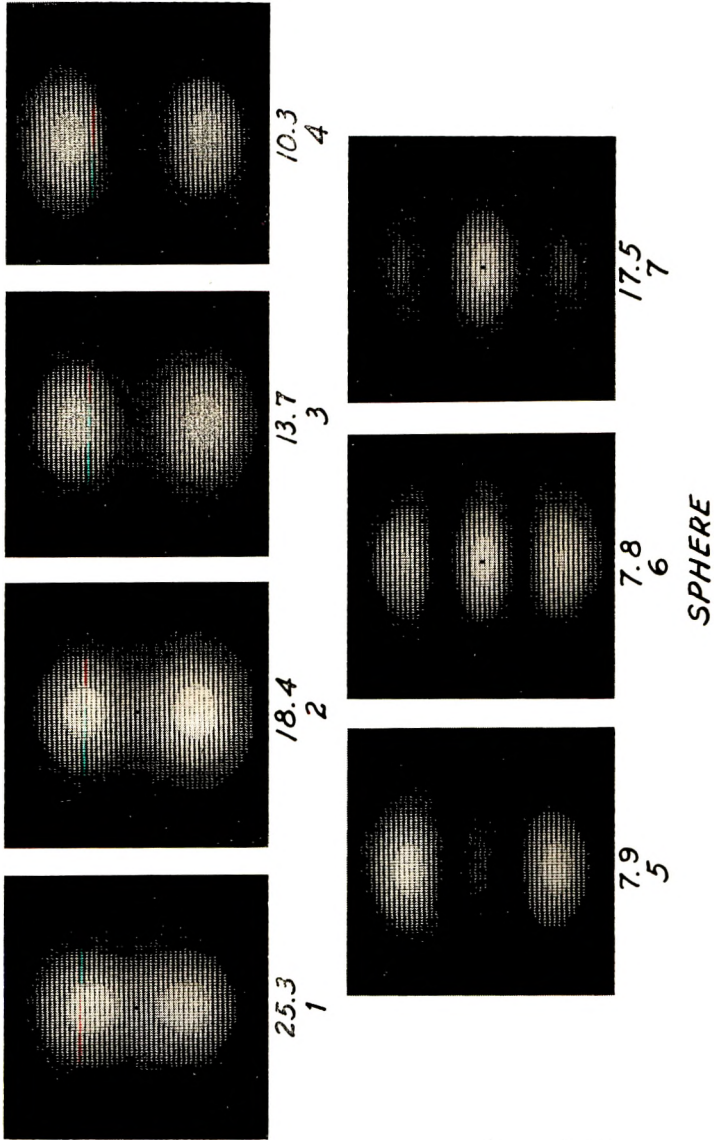
Fig. 44. Transformation of theoretical V_v SALS sphere pattern D to pattern A.
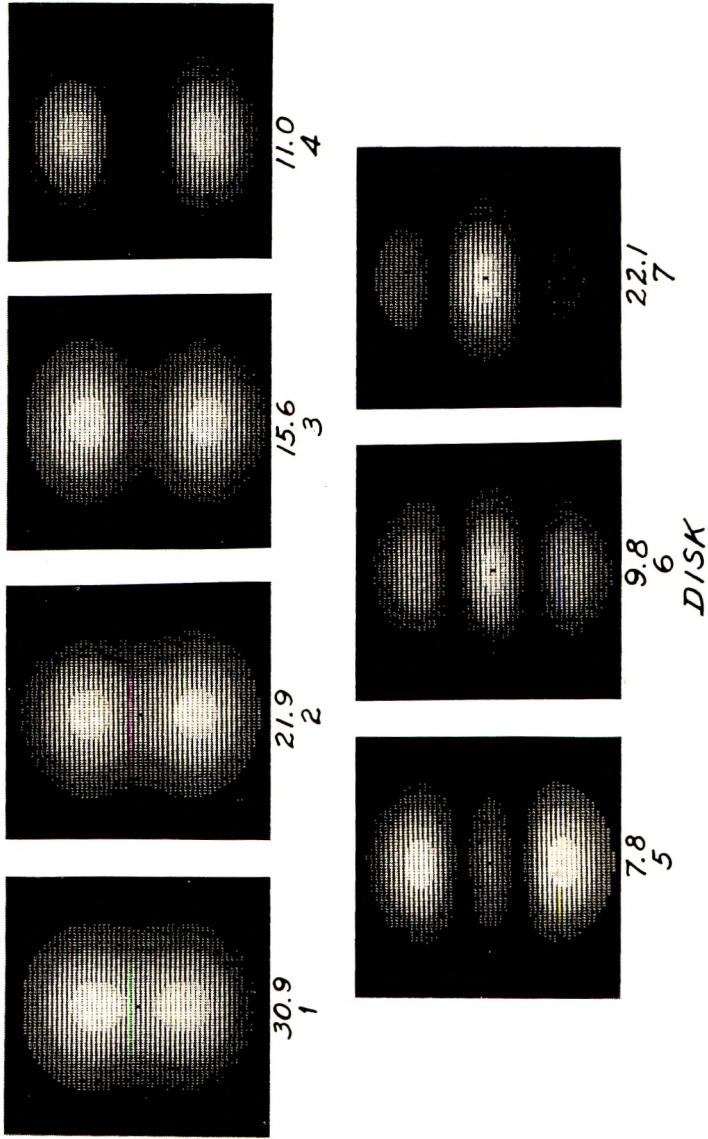
Fig. 45. Transformation of theoretical V_v SALS disk pattern D to pattern A.
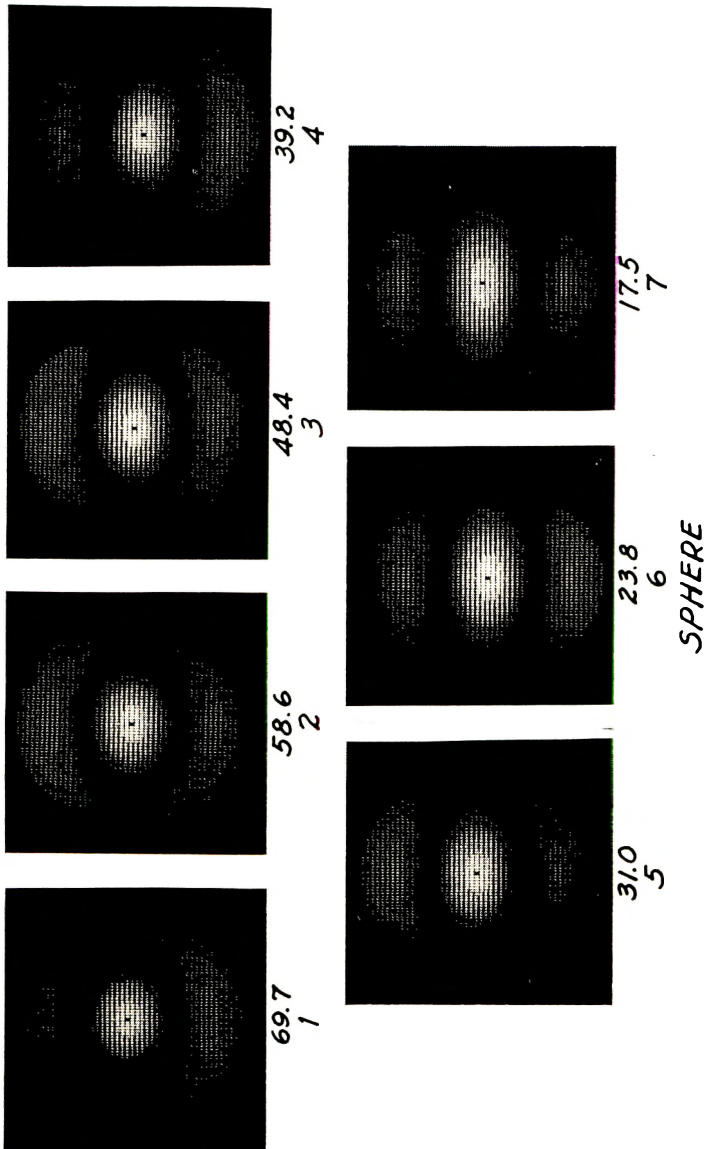
Fig. 46. Transformation of theoretical V_v SALS sphere pattern C to pattern A.
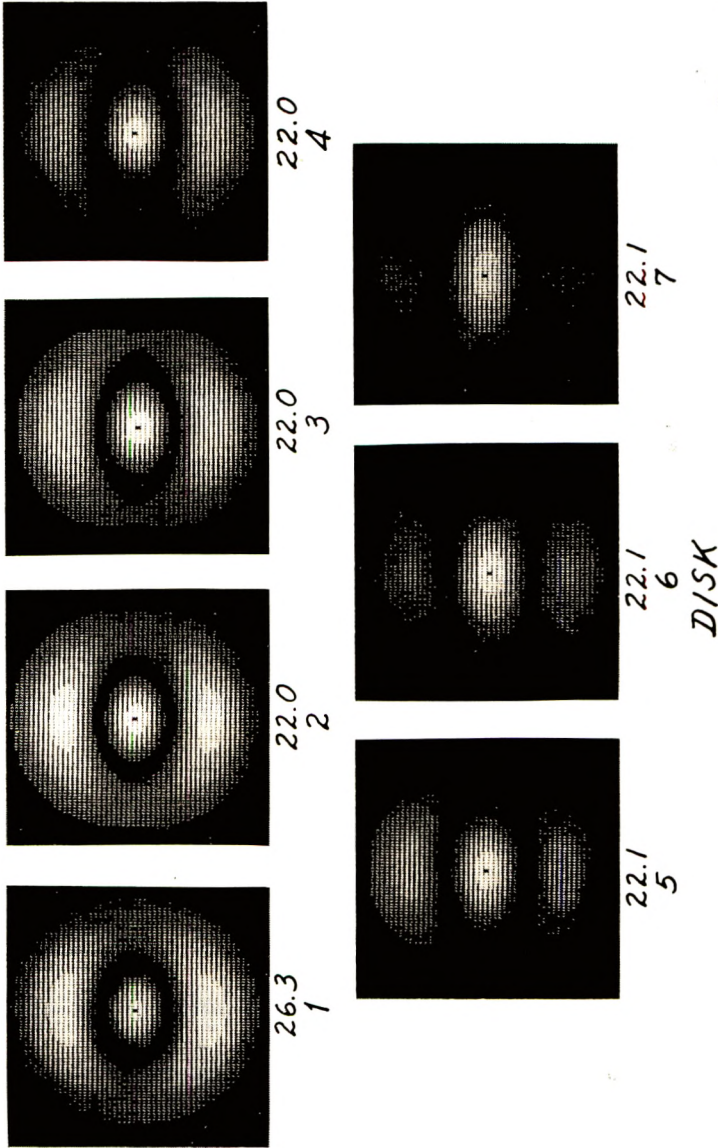
Fig. 47. Transformation of theoretical V_v SALS disk pattern C to pattern A.
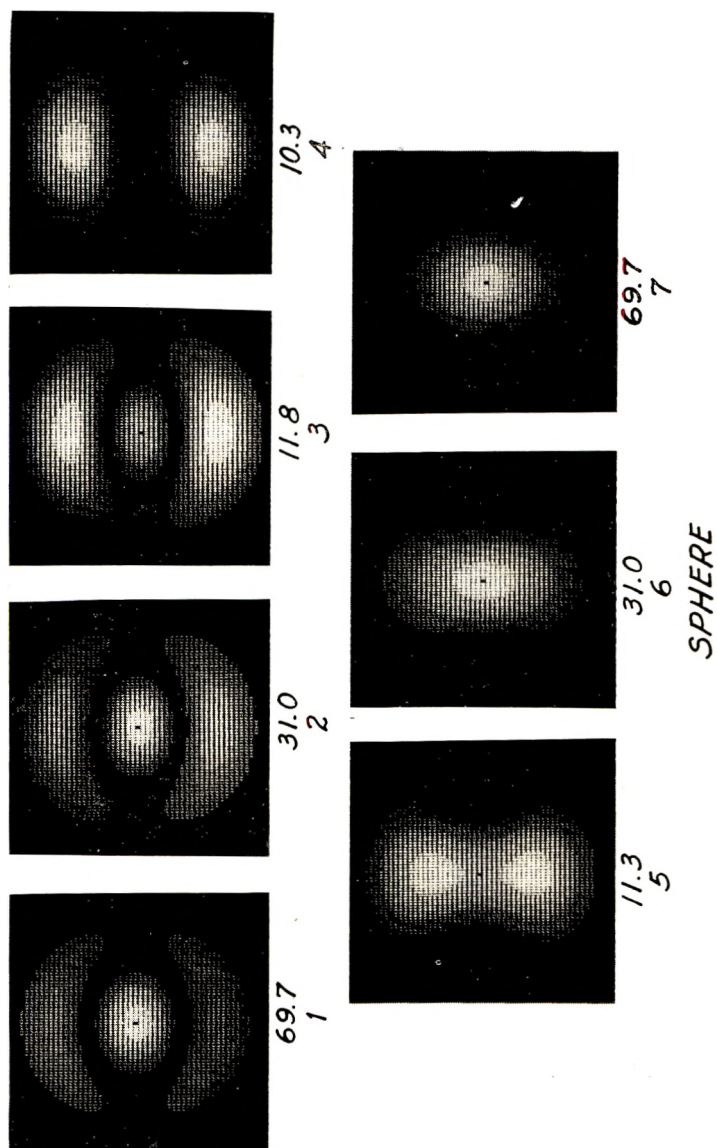
Fig. 48. Transformation of theoretical V_v SALS sphere pattern C to pattern B.
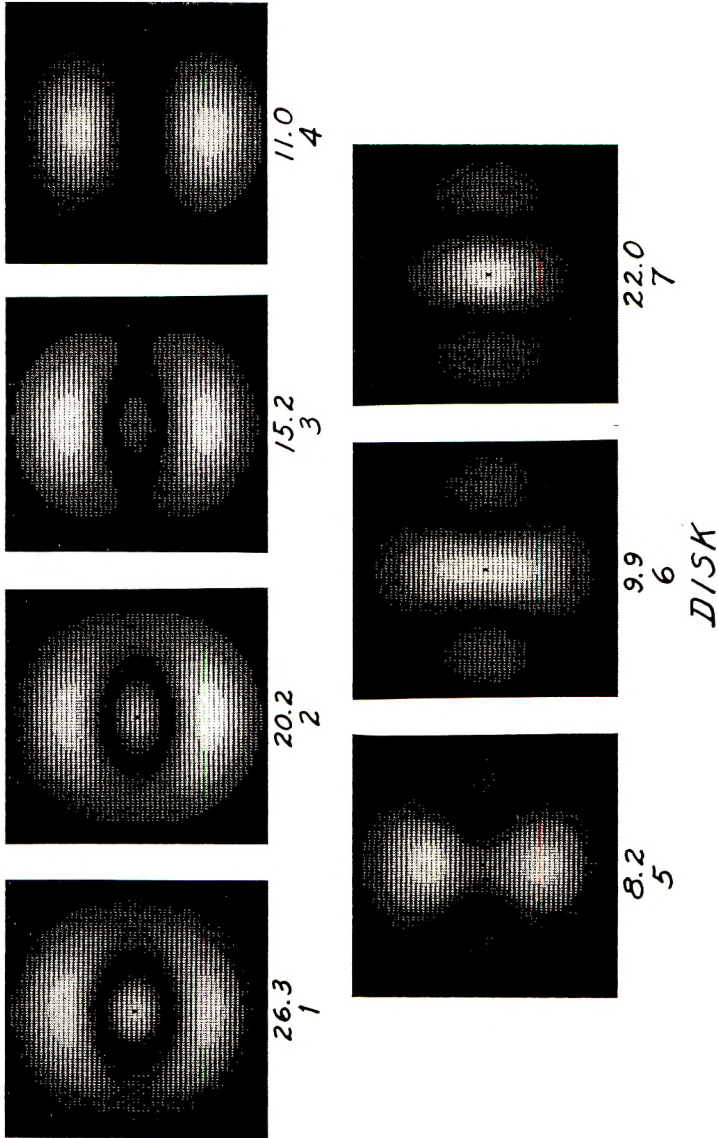
Fig. 49. Transformation of theoretical V_v SALS disk pattern C to pattern B.

disks has its highest intensity along the equator of the pattern ($\mu_D = 90°$), and its is concentrated in the side lobes ($\theta_D = 26°$). In patterns 4 and 5 for disks the maximum intensity remains in the side lobes along the equator and moves progressively toward the center of the pattern until it reaches $\theta_D = 0°$ at pattern 6 and remains there through pattern 7. In contrast, the maximum intensity in patterns 4 and 5 for spheres moves progressively away from the center with increasing pattern number and does this along the meridian ($\mu_s = 0°$) of the pattern (μ for spheres in this region is 90° out of phase with that of disks). By sphere pattern number 6 the maximum intensity region has moved farthest away from the center ($\theta_s = 26.7°$) along the meridian of the pattern; however, the intensity in the center of this pattern is progressively increasing. In sphere pattern 7 the increase in intensity in the central region of the pattern has become greater than that in the outer lobes and I_{max} is again at $\theta_s = 0°$, $\mu_s = 0°$, and is indistinguishable from the comparable disk pattern.

This discussion points out some of the features of the catalog of V_V SALS patterns and how it may be evaluated. By careful examination of the patterns other more subtle features of the scattering behavior will appear. By using the catalog in this way an intimate knowledge of the possibilities of the SALS technique will emerge.

References

1. R. S. Stein and M. B. Rhodes, *J. App.. Phys.*, **31**, 1873 (1960).

2. J. J. van Aartsen, *Offlce Naval Res. Tech. Rept.*, No. 83, March 1, 1966.

3. A. Keller, *J. Polym. Sci.*, **17**, 351 (1955).

4. H. D. Keith, F. J. Padden, Jr., N. M. Walter, and H. W. Wyckoff, *J. Appl. Phys.*, **30**, 1485 (1959).

5. R. J. Samuels, in *Supramolecular Structure in Fibers J. Poly. Sci. C*, **20**, P. H. Lindenmeyer, Ed., Interscience, New York, 1967, p. 253.

6. D. R. Kreger, *Biochim. Biophys. Acta*, **6**, 406 (1951).

7. R. J. Samuels and R. Y. Yee, *J. Polym. Sci. A-2*, in press.

8. P. Ingram and A. Peterlin, *J. Polym. Sci. B*, **2**, 739 (1964).

9. V. I. Selikhova, G. S. Markova, and V. A. Kargin, *Vysokomol. Soedin.*, **6**, 1136 (1964).

10. I. L. Hay and A. Keller, *Kolloid Z. Z. Polym.*, **204**, 43 (1965).

11. F. D. Bloss, *An Introduction to the Methods of Optical Crystallography*, Holt, Rinehart, and Winston, New York, 1961, p. 76.

12. K. Mühlethaler, *Stärke*, **17**, 245 (1965).

13. R. J. Samuels, in *Small Angle Scattering from Fibrous and Partially Ordered Systems J. Polym. Sci. C*, **13**, R. H. Marchessault, Ed., Interscience, New York, 1966, p. 37.

14. C. E. Green, private communication.

15. R. J. Samuels, *J. Polymer Sci. A-2*, **6**, 1101 (1968).

16. M. Kerker, *The Scattering of Light*, Academic Press, New York, 1969.

17. J. Borch and R. H. Marchessault, *J. Colloid Interface Sci.*, **27**, 355 (1968).

18. C. Picot, G. Weill, and H. Benoit, in *Macromolecular Chemistry, Prague 1965 J. Polym. Sci. C*, **16**, O. Wichlerle and B. Sedláček, Eds., Interscience, New York, 1968. p. 3973.

19. R. S. Stein, Office Naval Res. Tech. Rept. No. 106, January, 1968.

20. R. S. Stein, S. B. Clough, and C. Picot, *J. Polym. Sci., A-2*, **9**, 1147 (1971).

21. J. R. Partington, *An Advanced Treatis on Physical Chemistry*, Vol. 4, Longmans, Green, London, 1953, p. 72.

22. R. S. Stein and P. R. Wilson, Office Naval Res. Rept., No. 35, August 25, 1961.

23. R. S. Stein, M. B. Rhodes, P. R. Wilson, and S. N. Stidham, *Pure Appl. Chem.*, **4**, 219 (1962).

24. R. S. Stein and S. B. Clough, Office Naval Res. Rept., No. 76, June 30, 1965.

25. R. S. Stein, private communication.

26. R. S. Stein and C. Picot, *J. Polym. Sci. A-2*, **8**, 1955 (1970).

27. G. W. Schael, *J. Appl. Polym. Sci.*, **12**, 903 (1968).

28. A. Guinier, G. Fournet, C. Walker, and K. Yudowich, *Small-Angle Scattering of X-rays*, Wiley, New York, 1955, p. 19.

29. I. D. G. Macleod, *IEEE Trans. Computers*, **C**, **19**, 160 (1970).

30. C. E. Green, and O. W. Marks, private communication.

NOTES

Monomer Sequence Distributions in Copolymers of Vinylidene Chloride and Methacrylonitrile by PMR Spectroscopy

The PMR spectra of the methylene protons in copolymers containing only monomer units that are symmetrically substituted at the α-carbon can be analyzed in terms of singlet resonance peaks that correspond to identifiable tetrad sequences. Such an analysis has been reported for poly(vinylidene chloride-co-isobutylene).[1-3] The penultimate model for copolymerization is more consistent with the results in this study than the terminal model.

The PMR spectra of several addition copolymers containing vinylidene chloride and monomer units that are not symmetrically substituted at the α-carbon have been determined. The simplest methylene proton spectra for this class of copolymers occurs when no α-proton is present to couple with the methylene protons. The loss of symmetry about the α-proton in one of the monomer units produces heterosteric methylene protons in some sequences and complicates their spectra. Spectral assignments are usually incomplete in these cases, but information about the sequence distributions can be obtained.[4,5]

In this paper, the sequence distributions of poly(vinylidene chloride-co-methacrylonitrile), P(VDC–MAN), an example of this second class of copolymers, are determined by analysis of the PMR spectra. The copolymerizations were performed in bulk at three temperatures. Characteristics of the copolymer sequences and the polymerization kinetics are described.

Experimental

Bulk polymerizations were carried out in sealed ampoules with the use of about 0.06 g of benzoyl peroxide in 25 g of mixtures of vinylidene chloride (VDC) and methacrylonitrile (MAN). The ampoules containing the reaction mixtures were shaken in a constant temperature bath regulated to ±0.1°C for periods of time chosen to restrict the reaction yield to less than 5%. Polymerization was studied at 50.0, 71.0, and 90.0°C. The liquid content of each ampoule was transferred to a weighed flask and the solids were dissolved in pyridine and added to the flask. The copolymers were precipitated with carbon tetrachloride, dried and weighed.

The vinylidene chloride (Monomer-Polymer Lab.) and methacrylonitrile (Vistron Corp.) were distilled before use. The pyridine and carbon tetrachloride were Baker Analyzed Reagent Grade. All spectra were obtained at 60 MHz by using a Varian A-60 NMR spectrometer equipped with a variable temperature controller. The spectrum of PVDC was taken at 145°C with tetrachloroethane as solvent. All other spectra were run at 85°C, ±1°C, with the use of 10–15 wt-% solutions of the copolymers in pyridine. All samples included tetramethylsilane as an internal reference, and the chemical shifts were measured with respect to this reference by the sideband method. The spectra were integrated by using a planimeter. Areas used in all calculations were averages of at least three integrations.

Results and Discussion

The PMR spectra of the homopolymers are consistent with those previously reported.[6-8] The spectrum of PVDC polymerized at 50°C consists of a single sharp peak

2247
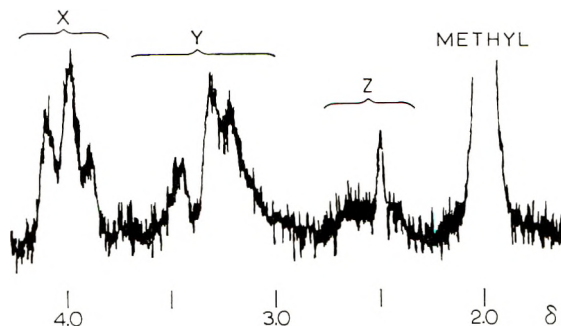
Fig. 1. A 60 MHz spectrum of P(VDC-MAN), polymerized at 50°C from $x = 4.0$.

at 3.85 δ. The spectrum of PMAN polymerized at 50°C matches one reported for an amorphous sample containing *meso* and racemic dyads. The peak at 1.90 δ is assigned to the methyl group. The quartet corresponding to the methylene protons of the *m*-dyads is not completely resolved and appears with the peak corresponding to the *r*-dyads in the region of 2.5-2.0 δ. Ishigure et al.[7] report a geminal coupling constant of 15.5 Hz and a chemical shift difference of 0.49 ppm for the methylene protons.

The PMR spectrum of a copolymer polymerized at 50°C from a monomer ratio x (VDC/MAN) of 4.00 is shown in Figure 1. The single peak at about 1.9 δ, assigned to the methyl protons, is not sensitive to the sequence. The complex spectrum in the region 4.2–2.0 δ is assigned to the methylene protons. The peaks in region X are assigned to the AA-dyads, where A is VDC and B denotes MAN units. The protons in these sequences are homosteric and three peaks at 4.07, 3.97 and 3.87 δ are distinguishable. These peaks are attributed to the AAAA, AAAB(BAAA), and BAAB tetrads, respectively. The Y region is assigned to the AB dyads and BA dyads, and it is complex because the methylene protons are heterosteric. Each of the central methylene protons corresponding to each of the AABA(ABAA), BABA(ABAB), AABB(BBAA) and BABB(BBAB) tetrads may exhibit a different H_aH_b spectrum. A detailed analysis of this region is not reported. The Z region is assigned to the methylene protons in the BB dyads. These protons are homosteric in the *r*-sequence or heterosteric in the *m*-sequence. Assignments corresponding to the ABBA, ABBB(BBBA), and BBBB tetrads are again not reported.

The copolymerization kinetics can be analyzed in terms of the terminal model. By assigning the X, Y and Z regions to the methylene protons in AA, (AB + BA), and BB dyads and using a variation of the method of Fischer et al.[1] the compositions of the copolymers, in mole or number fractions, are calculated by:

$$f_a = (A_x + A_y/2)/A \tag{1}$$

$$f_b = (A_z + A_y/2)/A \tag{2}$$

where f_a and f_b are the mole fractions of A and B in the copolymer, A_x, A_y, and A_z are the areas of the peaks in the X, Y and Z regions, and $A = A_x + A_y + A_z$.

Reactivity ratios, $r_a = k_{aa}/k_{ab}$ and $r_b = k_{bb}/k_{ba}$, were determined using the Ross-Fineman[9] form of the copolymer composition equation:

$$(x/f)(f - 1) = r_a(x^2/f) - r_b \tag{3}$$

where x is the ratio F_A/F_B of the mole fractions of the monomers in the reaction mixture, and $f = f_a/f_b$. A least-squares analysis was performed on each set of data to determine r_a and r_b. The reactivity ratios determined in this manner are listed in Table I. Plots

TABLE I
Reactivity Ratios Based on the Terminal Model

Polymerization temperature, °C	r_a	r_b
50.0	0.350 ± 0.017	2.05 ± 0.24
71.0	0.364 ± 0.041	1.48 ± 0.27
92.0	0.381 ± 0.058	1.73 ± 0.31

TABLE II
Arrhenius Parameters Based on the Terminal Model

Activation energy, kcal/mole	Frequency factor, l./mole-sec
E_{aa} 25[a]	A_{aa} 1.84×10^{19}[a]
E_{ab} 24.5	A_{ab} 2.34×10^{19}
E_{ba} 12.5	A_{ba} 2.34×10^{10}
E_{bb} 11.5[b]	A_{bb} 8.38×10^{9}[b]

[a] Data of Brandrup and Immergut.[10]
[b] Data of Burnett and Melville.[11]

of $\log r_a$ and $\log r_b$ versus $1/RT$ yield straight lines within the error intervals. A least-squares analysis of each of these sets of data produces the equations:

$$\log r_a = -0.105 - 227/RT \tag{4}$$

$$\log r_b = -0.446 + 468/RT \tag{5}$$

The Arrhenius expressions for the rate constants are:

$$\log r_a = \log (A_{aa}/A_{ab}) - [(E_{aa} - E_{ab})/2.30RT] \tag{6}$$

$$\log r_b = \log (A_{bb}/A_{ba}) - [(E_{bb} - E_{ba})/2.30RT] \tag{7}$$

The Arrhenius parameters for the photoinitiated polymerization of the homopolymers have been reported.[10,11] With these values, the remaining values for the copolymerization can be calculated (Table II).

Application of the transition-state theory gives: $\Delta S_{aa}{}^{\ddagger} - \Delta S_{ab}{}^{\ddagger} = 0.5$ eu/mole and $\Delta S_{bb}{}^{\ddagger} - \Delta S_{ba}{}^{\ddagger} = -2.0$ eu/mole.

Burnett and Melville[11] suggest that the unusually high values of E_{aa} and A_{aa} in the bulk homopolymerization of VDC are caused by the observed poor solubility of the polymer in the monomer. The growing radical may become surrounded by polymer requiring that the monomer diffuse through a layer of the polymer to the reaction site where it becomes virtually trapped. Precipitation also occurs in the copolymerization. Hence it is reasonable to use the E_{aa} and A_{aa} values of Burnett and Melville[11] in the comparisons.

By using the method of Kinsinger and Colton,[12] the number fraction of dyad sequences, f_{aa}, $f_{ab} = f_{ba}$ and f_{bb}, were calculated from each set of reactivity ratios corresponding to the several monomer-solution compositions. These values were in good agreement with the experimental values of the dyad concentrations obtained directly from the spectral data by:

$$f_{aa} = A_x/A \tag{8}$$

$$2f_{ab} = 2f_{ba} = A_y/A \tag{9}$$

$$f_{bb} = A_z/A \tag{10}$$
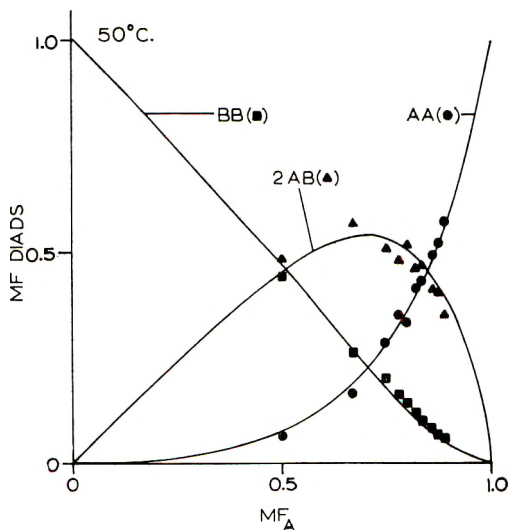
Fig. 2. Mole fraction dyads vs. mole fraction of VDC in reaction solution; polymeriza-
tion at 50.0°C. Solid lines represent $r_a = 0.350$ and $r_b = 2.05$.

TABLE III
Reactivity Ratios Based on Penultimate Theory Analysis

Polymeriza-tion temperature, °C	R_a	R_a'	R_b	R_b'
50.0	0.52 ± 0.05	0.22 ± 0.02	0.65 ± 0.41	4.06 ± 0.56
71.0	0.35 ± 0.07	0.50 ± 0.04	1.07 ± 0.52	2.30 ± 0.33
92.0	0.37 ± 0.04	0.43 ± 0.04	1.28 ± 0.37	2.44 ± 0.29

A comparison is provided in Figure 2. The maximum for f_{ab} occurs in the region of
0.6–$0.75F_A$ at each polymerization temperature.

Ito and Yamashita[13] have proposed a method for analyzing the experimental data in
terms of penultimate kinetics parameters. The method requires knowledge of the
copolymer composition and the concentration of the dyad sequences.

The number-average lengths of sequences of A units, L_a, and of B units, L_b, are
defined by

$$L_a = f_a/f_{ab} = 1 + (P_{baa}/P_{aab}) \tag{11}$$

$$L_b = f_b/f_{ba} = 1 + (P_{abb}/P_{baa}) \tag{12}$$

where the P terms are probability functions, e.g., P_{baa} is the conditional probability
that a growing polymer chain having B as its penultimate unit and A as its end unit
will add an A unit. In terms of the reactivity ratios and x, useful forms of eqs. (11)
and (12) are:

$$(L_a - 2)/x = R_a - (1/R_a')(L_a - 1)/x^2 \tag{13}$$

$$(L_b - 2)x = R_b - (1/R_b')(L_b - 1)x^2 \tag{14}$$

where

$$R_a = k_{aaa}/k_{aab},$$
$$R_a' = k_{baa}/k_{bab},$$
$$R_b' = k_{abb}/k_{aba},$$
$$R_b = k_{bbb}/k_{bba}$$

Experimental values of L_a and L_b were determined directly from the spectral data by

$$L_a = (A_x + A_y/2)/(A_y/2) \tag{15}$$

$$L_b = (A_z + A_y/2)/(A_y/2) \tag{16}$$

The results of these calculations using a least squares analysis of each set of data are listed in Table III.

The lack of a penultimate effect would be indicated by $R_a = R_a'$ and $R_b = R_b'$. Despite the large standard deviation in R_b and R_b', these results indicate a penultimate effect which diminishes as the temperature increases. The increase in the solubility of the growing copolymer chains with high concentrations of VDC as the temperature increases probably contributes to the changes in reactivity ratios.

References

1. T. Fisher, J. B. Kinsinger, and C. W. Wilson, *J. Polym. Sci. B*, **4**, 379 (1966).
2. T. Fisher, J. B. Kinsinger, and C. W. Wilson, *J. Polym. Sci. B*, **5**, 285 (1967).
3. K. H. Hellwege, U. Johnsen, and K. Kolbe, *Kolloid-Z. Z. Polym.*, **214**, 45 (1966).
4. U. Johnsen and K. Kolbe, *Kolloid-Z. Z. Polym.*, **216**, 97 (1967).
5. K. Ito, S. Iwase, and Y. Yamashita, *Makromol. Chem.*, **110**, 233 (1967).
6. R. Chujo, S. Satoh, T. Ozeki, and E. Nagai, *J. Polym. Sci.*, **61**, S12 (1962).
7. K. Ishigure, Y. Tabata, and K. Oshima, *J. Polym. Sci. B*, **4**, 669 (1966).
8. A. L. Segre, F. Ciampelli, and G. Dall'Asta, *J. Polym. Sci. B*, **4**, 633 (1966).
9. S. D. Ross and M. A. Fineman, *J. Polym. Sci.*, **5**, 259 (1950).
10. J. Brandrup and E. H. Immergut, Eds., *Polymer Handbook*, Interscience, New York, 1966, pp. 11–68.
11. J. D. Burnett and H. W. Melville, *Trans. Faraday Soc.*, **46**, 976 (1950).
12. J. B. Kinsinger and D. Colton, *J. Polym. Sci. B*, **3**, 797 (1965).
13. K. Ito and Y. Yamashita, *J. Polym. Sci. A*, **3**, 2165 (1965).

R. E. BLOCK
H. G. SPENCER

Department of Chemistry
Clemson University
Clemson, South Carolina 29631

Dependence of the Intrinsic Viscosity of Polyelectrolytes on the Concentration of Added Salt

When plotted against $c_s^{-1/2}$, with c_s denoting the concentration of added salt, the intrinsic viscosity of polyelectrolytes shows a linear dependence for large values of c_s but some deviation has been observed for smaller concentrations.[1-4] We shall present here a new theoretical formula, based on the recent theory by Yeh and Isihara,[5,6] which accounts for such a nonlinear dependence.

For this purpose, we make use of a formula derived before:[5,6]

$$[\eta] = \frac{Nab^2/6m}{1 + (6a/\pi^{1/2}b)N^{1/2}f(z)} \frac{1 + 3(cz)^{1/2} + 3cz}{1 + 3(cs)^{1/2}} \tag{1}$$

where

$$f(z) = \exp\{3(cz)^{1/2}\}[1 + 3(cz)^{1/2}]^{-1} \int_0^\infty \exp[-y - (9cz/4y)]dy \tag{2}$$

and

$$z = (3/2\pi b^2)^{3/2}\beta N^{1/2} \tag{3}$$

Here, N is the number of segments in a polymer chain, a is the effective radius of a segment considered as a sphere and m is its mass, b is the bond length and β is the effective excluded volume for a pair of segments.

Equation (1) is based on the assumption that the segments are spherically distributed about the center of mass of a polymer chain with a distribution characterized by an excluded volume parameter cz, where c is a constant of the order of unity. The formula is applicable to a flexible chain molecule in the presence of both excluded volume and hydrodynamic interactions. Since the excluded volume effect has been expressed in terms of an arbitrary potential function, we find it possible to apply the formula to polyelectrolytes. However, in the previous treatment we used only the first term of the Taylor expansion of the Boltzmann factor for the parameter β. One can improve on this by using the Debye approximation (or the equivalent considerations based on ring diagrams[6]) because it takes into consideration all orders in interaction although the pattern of interaction is limited to a ring form.

In the Debye approximation, the equation of state of an electron gas is given by:[7]

$$p/kT = n - (n/3)(\partial S/\partial n) \tag{4}$$

where n is the density and where

$$S = \kappa^3/12\pi$$
$$\kappa^2 = (4\pi\epsilon^2/kT)n \tag{5}$$

and where ϵ is the effective charge and n is the number density of charges. The effect of Coulomb interactions on the parameter β is then given by

$$\beta = (1/3n)(\partial S/\partial n)$$
$$= (4\pi\epsilon^2/kT)^{3/2}[24\pi n^{1/2}]^{-1} \tag{6}$$

on the assumption that eq. (4) is applicable. Since $n \propto c_s$, we have

$$z = z_0 c_s^{-1/2} \tag{7}$$
$$z_0 = (3/2\pi b^2)^{3/2}N^{1/2}B \tag{8}$$
$$B = (4\pi\epsilon^2/kT)^{3/2}(24\pi)^{-1}(10^3/2N_a)^{-1/2}$$

where N_a is Avogadro's number and c_s is in mole/l.

The function $f(z)$ is close to unity for $z \to 0$ and varies as $z^{-1/4}$ for large z. Assuming that z is small we obtain from eq. (1) the following approximate formula:

$$[\eta] = [\eta]_\infty \{1 + 3cz_0/c_s^{1/2} - 9c^{3/2}z_0^{3/2}/(c_s^{1/2})^{3/2} + \ldots\} \tag{9}$$

where $[\eta]_\infty$ is the limiting viscosity for $c_s \to \infty$.

Equation (9) shows that $[\eta]$ plotted against $c_s^{-1/2}$ is a straight line in the first approximation, but a gradual bending due to the second term occurs. Such a deviation has been observed by experiments. Equation (9) agrees in form with the empirical relation proposed by Noda et al.[2]

For a polymer of molecular weight $M = 1.5 \times 10^4$, monomer molecular weight $m = 140$ and $a = 1.5$ Å, $b = 9.0$ Å, eq. (9) gives

$$[\eta] = 12.43 + 1.10(cz_0)/c_s^{1/2} - 0.00207(cz_0)^2/c_s + \ldots \tag{10}$$

where the unit of the intrinsic viscosity is in ml/g. The constant cz_0 still has to be determined. If $c = 1.0$ and if the effective charge is equal to 0.76 times the electronic charge, then cz_0 is 5.1. This gives $1.10(cz_0) = 5.61$, in agreement with Noda et al[2].

References

1. A. Takahashi and M. Nagasawa, *J. Amer. Chem. Soc.*, **86**, 543 (1965).

2. I. Noda, T. Tsuge, and M. Nagasawa, *J. Phys. Chem.*, **74**, 710 (1970).

3. S. Rice and M. Nagasawa, *Polyelectrolyte Solutions*, Academic Press, New York, 1961, p. 503.

4. D. T. F. Pals and J. J. Hermans, *Rec. Trav. Chim.*, **71**, 433 (1952).

5. R. Yeh and A. Isihara, *J. Polym. Sci. A-2*, **9**, 373 (1971); *J. Polym. Sci. A-1*, **8**, 861 (1970).

6. A. Isihara, *Adv. Polym. Sci.*, **5**, 531 (1968).

7. H. Friedman, *Ionic Solution Theory*, Wiley, New York, 1962.

H. Chien
A. Isihara

Statistical Physics Laboratory
Department of Physics
State University of New York
Buffalo, New York 14214

Column Fractionation of Polymers. XXI. Gel-Permeation Chromatography: The Effect of Sample Viscosity on Elution Characteristics

A number of studies on gel-permeation chromatography have reported changes in elution volume with the amount of sample injected.[1-8] In general, for samples of narrow distribution the elution volume increases with increasing sample size, and the rate of change increases with increasing molecular weight. Broad distribution samples show changes both in the position of the chromatogram maximum and in its shape.

Previous studies have indicated that viscosity effects may be partially responsible for the observed changes in elution behavior.[3,8,9] However, the changes in viscosity have been coupled with changes in polymer concentration and molecular weight. In this work, changes in viscosity have been made in a similar manner but have also been achieved at constant polymer concentration by varying the viscosity of the solvent in which the polymer is dissolved prior to injection in the chromatograph.

Experimental

The chromatograph used was a Waters Model 200 (Waters Associates, Framingham, Massachusetts) with a differential refractometer detector. The columns were four 4-ft sections packed with crosslinked polystyrene gels with nominal pore sizes of 10^6, 10^5, 10^4, and 10^3 Å, respectively, and arranged in order of decreasing pore size from entrance to exit. The columns were operated at ambient temperatures at a flow rate of 1.0 ml/min. The eluant was tetrahydrofuran (THF) in all cases. The standard multiport injector valve with a 2 cc sample loop was used.

The polystyrene samples were anionically polymerized, samples of narrow molecular weight distribution (Pressure Chemical Company, Pittsburgh, Pennsylvania). The solvents used to dissolve the polystyrenes were tetrahydrofuran, two viscosity grades of chlorinated diphenyls (Monsanto Aroclor), and various mixtures of tetrahydrofuran and the Aroclors.

Relative viscosities were measured in capillary viscometers. The number of plates was calculated in the conventional manner. No attempt was made to separate the various contributions to peak width, except for the changes with the sample injected, all other contributions to peak width remained constant.

Results and Discussions

Table I lists the conditions and results for all measurements. The lowest concentration for each molecular weight was selected to be sufficiently low so that no concentration effects due to overloading were present. Figure 1 plots the change in elution volume with viscosity increase for two polystyrenes with a molecular weight of 411,000 and 1,800,000. The increase in elution volume with increasing polymer concentration is generally consistent with the results observed by others.[3,8] The samples where the viscosity was changed by changing the solvent viscosity also show a slight increase in elution volume but the effect is not as large. In both cases the change in elution volume represents a significant change in calculated molecular weight; for example, from 411,000 to 96,000.

Figure 2 shows the change in column efficiency with change in relative viscosity for molecular weight 1,800,000. Directionally there is a major decrease in efficiency as the relative viscosity goes from 1 to 3 with a lower limiting value being reached at relative viscosities of 3 to 5. After this, the efficiency remains essentially constant at relative viscosities as large as 37. There appears to be a somewhat smaller loss in efficiency if the viscosity change is due to changing solvent, but this difference is small and may be within the experimental error $\pm 10\%$. Similar behavior is observed for molecular weights of 860,000 and 411,000.

TABLE I
Viscosity Effects on Elution Characteristics

Polymer MW × 10⁻³	Polymer concentration, wt-%	Solvent by volume	Relative kinematic viscosity[a]	Elution volume, ml/5	Plates per foot
1800	0.25	THF	1.0	24.8	25.5
	1.0	THF	1.3	25.5	7.4
	2.0	THF	2.1	25.7	5.8
	2.0	THF	3.0	25.8	6.6
	2.0	THF	7.0	25.9	5.5
	8.0	THF	14	26.4	6.1
	0.25	10 Aroclor 1248:1 THF	4.5	25.4	9.4
	0.25	30 Aroclor 1248:1 THF	11	25.4	9.0
	0.25	Aroclor 1248	37	25.4	9.6
860	0.25	THF	1.0	25.6	41.1
	1.0	THF	1.2	26.1	17.2
	2.0	THF	1.5	26.2	10.2
	0.25	5 Aroclor 1248:1 THF	2.2	26.1	13.9
	0.25	10 Aroclor 1248:1 THF	4.5	26.1	14.3
	0.25	30 Aroclor 1248:1 THF	11	26.4	16.0
	0.25	Aroclor 1248	37	26.4	13.8
411	0.25	THF	1	26.5	43.2
	1.0	THF	1.1	26.6	26.2
	2.0	THF	1.2	27.0	17.3
	2.0	THF	3.3	28.2	11.8
	2.0	THF	6	28.4	12.2
	13.0	THF	14	28.5	9.4
	0.25	5 Aroclor 1248:1 THF	2.2	27.3	17.6
	0.25	10 Aroclor 1248:1 THF	4.5	27.0	16.7
	0.25	30 Aroclor 1248:1 THR	11	27.0	16.7
	0.25	Aroclor 1248	37	27.2	15.6
19.8	0.25	THF	1	30.6	61.6
	0.25	10 Aroclor 1248:1 THF	4.5	31.3	—
	0.25	30 Aroclor 1248:1 THF	11	31.4	—
	0.25	Aroclor 1248	37	31.5	—

[a] THF viscosity 0.53 cP at ambient test temperature.

Flodin[9] studied the separation of relatively large samples of haemoglobin and sodium chloride on dextran gels. By adding a dextran fraction with a molecular weight of 1,800,-000 the relative viscosity of the sample was varied from 1 to 11.8. As the relative viscosity increased, the peak shapes changed from almost perfectly symmetrical and completely separated to extremely distorted. Flodin cited compression of the gel bed as a partial explanation of the observed results. It does not seem probable that gel compression is responsible for any significant portion of the effects observed in this study because only minor effects were noted as the relative viscosity was changed from 49 to 195 (see data in Table I for $M = 19,800$).

Considerable qualitative discussion has taken place in recent years concerning the so-called "viscous fingering" effect in gel-permeation chromatography.[10] This idea has its foundation in concepts developed for the flow of viscous fluids through packed beds and the behavior of a high-viscosity "slug" being pushed through a matrix by a low viscosity fluid. From this effect both a change in efficiency and elution volume may be expected, and in the direction reported in this study.
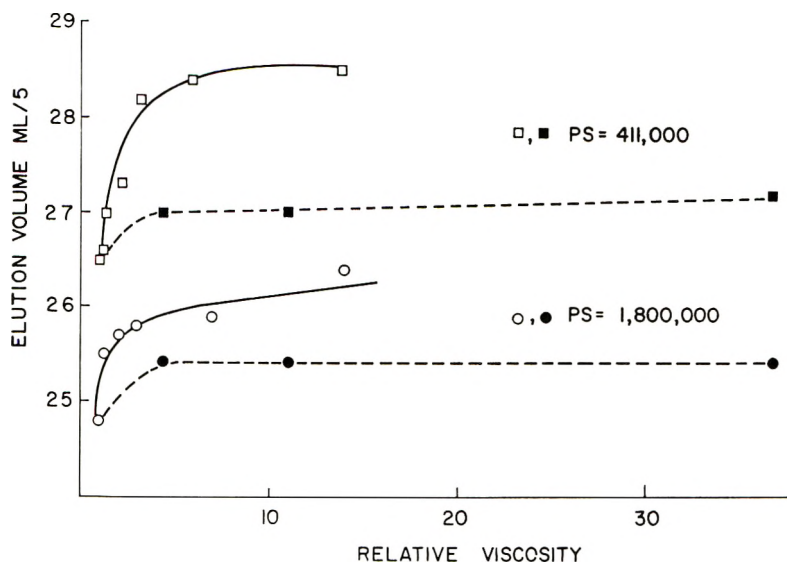
Fig. 1. Elution volume vs. relative viscosity: (O,□) viscosity increase from added polymer; (●,■) viscosity increase from changing solvent.
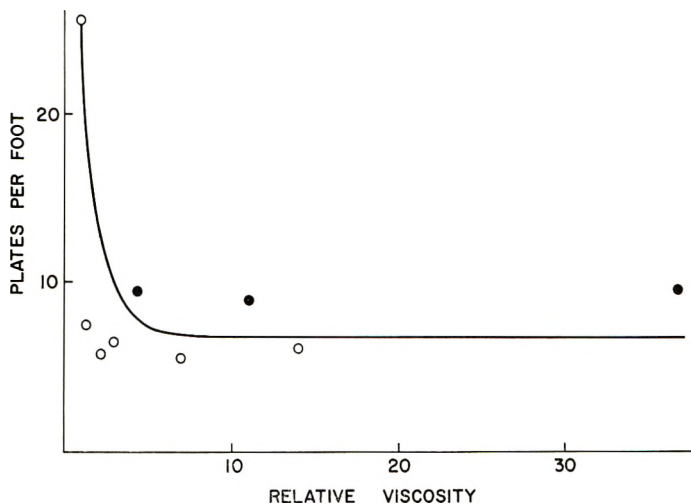
Fig. 2. Efficiency vs. relative viscosity for polystyrene, $M = 1.8 \times 10^6$: (O) viscosity increase from added polymer; (●) viscosity increase from changing solvent.

The viscous fingering effect in essence leads to an injection over a broader volume than that of the injection loop. Movement of the lower-viscosity THF elution solvent across the undissolved injection solution thus provides a band spreading mechanism. The greater the viscosity difference, the greater the band spreading might be expected. In this regard it should be noted that the high and greatly different viscosity media used for polymer injection give effectively the same reduction in column efficiency. Thus the dominant mechanism may not be due to the differential and parallel flow of fluids of different viscosity. Elution volumes are increased rather than shortened by increasing

concentration and viscosity. This feature could be explained by the viscous fingering in that the high-viscosity injection, once it has been "broken through" by the trailing low-viscosity eluent, will travel at a slower rate on the average leading to not only a broader elution peak but one which appears at a later time. Both of these effects are consistent with the observations made here and in other studies. However, the differences in the elution volumes produced by the two methods of changing viscosity indicate that viscosity alone cannot be wholly responsible for the change in elution volume.

References

1. M. J. R. Cantow, R. S. Porter, and J. F. Johnson, *J. Polym. Sci. B*, **4**, 707 (1966).

2. D. J. Harmon, Preprints Second Int. Symp. Gel Permeation Chromatography, Boston, September 1955.

3. J. E. Hazell, L. A. Prince, and H. E. Stapelfeldt, in *Analytical Gel Permeation Chromatography (J. Polym. Sci. C*, **21**,) R. S. Porter and J. F. Johnson, Eds., Interscience, New York, 1968, p. 43.

4. N. Nakajima, in *Analytical Gel Permeation Chromatography (J. Polym. Sci. C*, **21**), R. S. Porter and J. F. Johnson, Eds., Interscience, New York, 1968, p. 153.

5. F. Rodriquez, R. A. Kulakowski, and O. K. Clark, *Ind. Eng. Chem., Prod. Res. Develop.*, **5**, 121 (1966).

6. R. M. Screaton and R. W. Seeman, in *Analytical Gel Permeation Chromatography (J. Polym. Sci. C*, **21**), R. S. Porter and J. F. Johnson, Eds., Interscience, New York, 1968, p. 297.

7. J. L. Waters, paper presented at American Chemical Society Meeting, 1965; *Polym. Preprints*, **6**, 1061 (1965).

8. K. A. Boni, F. A. Sliemers, and P. B. Stickney, *J. Polym. Sci. A-2*, **6**, 1567 (1968).

9. P. Flodin, *J. Chromatog.*, **5**, 103 (1961).

10. K. H. Altgelt and J. C. Moore, in *Polymer Fractionation*, M. J. R. Cantow, Ed., Academic Press, New York, 1967, pp. 164–165.

K. Peter Goetze
Roger S. Porter

Julian F. Johnson

Polymer Science and Engineering
University of Massachusetts 01002

Department of Chemistry and
Institute of Materials Science
University of Connecticut
Storrs, Connecticut 06268

AUTHOR INDEX, VOLUME 9

SUBJECT INDEX, VOLUME 9

16 и.н. 2515